An Underwater Explosion-Induced Ship Whipping Analysis Method for use in Early-Stage Ship Design

Benjamin C. Brainard

Thesis submitted to the Faculty of the
Virginia Polytechnic Institute and State University
in partial fulfillment of the requirements for the degree of

MASTER OF SCIENCE

in

Ocean Engineering

Alan J. Brown, Chair
Ming Ma
Kevin Wang

December 9, 2015
Blacksburg, VA

Keywords: Underwater Explosion, Surface Ship, Whipping, MAESTRO

An Underwater Explosion-Induced Ship Whipping Analysis Method for use in Early-Stage Ship Design

Benjamin C. Brainard

Abstract

This thesis presents an analysis method for determining the whipping response of a hull girder to underwater explosion (UNDEX) bubble pulse loading. A potential flow-based UNDEX bubble model capable of calculating the behavior of a migrating bubble for up to three pulses is developed. An approximate vertical plane ship vibration model is derived using fundamental beam theory by representing the ship as a free-free beam with varying cross-sectional properties along its length. The fluid-structure interaction is approximated using strip theory and the distant flow assumption. The most severe predicted whipping load conditions are applied to a MAESTRO finite element model of the ship as a quasi-static load case to determine the response of the structure to the whipping loads. The calculated hull girder bending moments are compared to the ultimate bending strength of the hull girder to determine if the girder will collapse. The analysis method is found to be a useful method for determining preliminary UNDEX-induced whipping design load cases for early-stage ship design. However, more detailed and accurate data is needed to validate and verify the predicted whipping responses.

It is found that the most severe whipping loads occur as the result of an UNDEX event that occurs under the keel near midship and produces a bubble with a pulsation frequency similar to the natural vibration frequency of the ship in its third mode. Significant damage to the ship structure and hull girder collapse is possible as a result of these loads.

Dedication

To the memory of Dr. Owen Hughes, who was originally a member of this thesis committee. His passion for teaching and immense contributions to the field of ocean structures will not soon be forgotten.

Acknowledgements

I would like to thank Dr. Alan J. Brown for his guidance, support, and expertise throughout this project. Your patience and understanding is greatly appreciated.

I would also like to thank the members of my committee, Dr. Ming Ma and Dr. Kevin Wang, for their assistance and support.

Most importantly, I would like to thank my family for their love, motivation, and patience throughout my studies and life. Without it, none of this would have been possible and I would not be the person I am today.

Table of Contents

List of Figures

List of Tables

Chapter 1 Introduction

1.1 Motivation and Background

The underwater explosion (UNDEX) and subsequent ship interaction problem has many unique characteristics, all of which are governed by complex physics [1]. The complexity of this problem necessitates the use of significant time and computer resources to obtain solutions which accurately represent the physics involved. For this reason, the response of a ship to an UNDEX event is typically not included in early-stage ship design when multiple hull forms and structural characteristics are being considered. A fast and simple method of determining the response of ships to potential UNDEX threats with reasonable accuracy, coupled with an effective early-stage structural design tool, would enable the consideration of such threats in early-stage ship design and should result in ships that are better prepared to survive UNDEX events.

1.1.1 Ship Survivability

The United States Navy defines survivability as: "the capacity of the total ship system to avoid and withstand damage and maintain and/or recover mission integrity [2]." Ship survivability can be quantified as:

$$S = 1 - P_h P_{k/h}\left(1 - P_{r/k}\right) \tag{1}$$

where S is the probability of survival for a naval ship, P_h is the probability of the ship being hit by a threat weapon, $P_{k/h}$ is the probability of a kill or loss of mission capability given the ship is hit, and $P_{r/k}$ is the probability of the ship recovering given a specific kill or loss. These probability terms are called susceptibility, vulnerability, and recoverability.

Susceptibility considers the ability of a threat to hit the ship and the ability of the ship to avoid the threat, which includes both active and passive methods [2]. Active avoidance methods include maneuvering, striking the attacker, intercepting potential threats after they are launched, but before they reach the ship, and electronic warfare, such as threat detection and radar jamming techniques. Passive methods primarily involve limiting ship signatures, such as radar cross-section and acoustic, magnetic, and thermal signatures. Vulnerability is the probability of the ship sustaining some level of damage or capability loss after being hit. This considers the full range of possible threat weapons and scenarios in addition to the passive ability of the ship systems and structure to withstand and minimize damage from a successful enemy weapon strike.

Recoverability measures the ability of the ship to control, stop, and recover from damage caused by a successful enemy weapon strike, and minimize loss of life and mission capabilities as a result of the strike.

Mission capabilities are typically grouped into primary mission capabilities and secondary mission capabilities. Primary capabilities are required to be operational for the ship to complete its missions. Primary capabilities include: ship control and propulsion; command and control; navigation; communications; surface, air, and underwater surveillance; countermeasures; launch, recover, fuel, and rearm aircraft and small craft; essential maintenance of aircraft and ordnance; weapons stowage, control, launch, and guidance; replenish at sea; mine-hunting and sweeping; combat payload transport; casualty and damage control; collective protection system [3]. The loss of any of these capabilities is considered a kill by the definition of vulnerability.

This thesis focuses on the vulnerability of a ship structure to an under-keel UNDEX event. An under-keel UNDEX event has the potential to severely damage or even sink a ship, causing a loss of all capabilities.

1.1.2 Threats

A naval ship may be subjected to many types of weapons that threaten the ability of the ship to perform its mission. Numerous threat scenarios are possible. For naval ships, the primary explosive threats are underwater explosions (UNDEX) and air explosions (AIREX). These events are categorized as internal or external based upon where the event occurs. External explosion events are also categorized by their proximity to the vessel.

The severity of an UNDEX event is closely related to its location relative to the ship, as the types of possible damage from the event vary based upon the location of the explosion. UNDEX threats can occur in both far and close proximity to the ship, with a contact explosion also being a possibility. Figure 1 shows the result of an under keel torpedo explosion, illustrating that it is one of the most severe UNDEX threats. Torpedoes and mines are the primary weapons that present UNDEX threats to ships. Some past and present torpedoes, their nation of origin, and their warhead sizes are listed in Table 1. The same information for underwater mines is listed in Table 2. These types of threats are the focus of this thesis.

Figure 1 – Under Keel UNDEX Example [4]

Table 1 – Torpedo Charge Sizes

Name/ Model	Nation	Charge Size (kg)	Charge Size, TNT Equivalent (kg)	Charge Type	Reference
MK-48	USA	295	544	PBXN-103	[5, 6]
MK-37	USA	150		HBX-3	[6]
MK-54	USA	44	108	PBXN-103	[5, 6]
DM2A4	Germany	255	460	PBX	[5, 6]
Spearfish	UK	300		PBX	[5, 6]
G-RX2	Japan	267			[6]
Type 65	Russia	450/557			[6]
Type 53	Russia	265-400	265-400	TNT	[6]
Shkval	Russia		210		[5]
APR-3	Russia	74	74		[6]

Table 2 – Mine Charge Sizes

Name/Model	Nation	Charge Size (kg)	Charge Size, TNT Equivalent (kg)	Charge Type	Reference
MK-67	USA	230			[6]
MK-62/63/64	USA	227/454/907		H-6 or PBXN-103	[6]
MK-56	USA	163		HBX-3	[6, 7]
Stonefish	UK/ Australia	100-600		PBX	[6, 8]
EM-52	China	140			[9, 10]
EM-56	China	380			[9, 10]
EM-57	China	300/700			[10]
M-4	China	600			[9, 10]
PMK-1	Russia		350		[10]
PMK-2	Russia		110		[9, 10]

1.2 Underwater Explosion Event

The general UNDEX problem begins with an explosive charge of a certain size and material located at a depth below the free surface in proximity to a ship [11]. A typical arrangement of an UNDEX problem is shown in Figure 2. The water is assumed to behave as a compressible fluid that is incapable of supporting significant tension. The event may be classified as either far-field or near-field depending upon the position of the charge relative to the ship, which is floating on the free surface, and the response of the ship in both the early and late timeframes. These explosion types are defined later in this section.

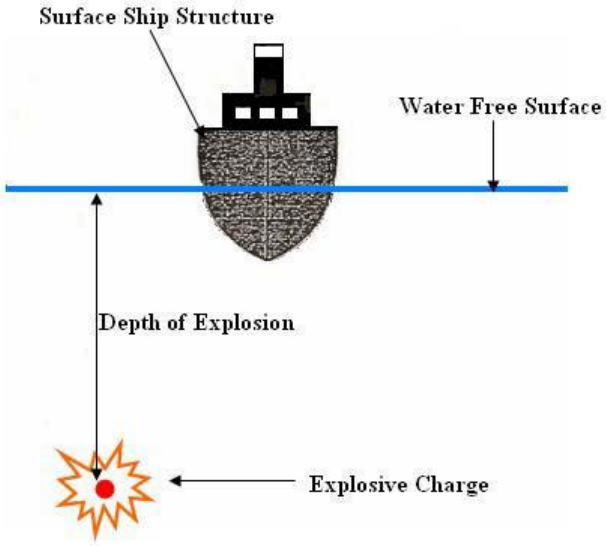

Figure 2 – General Setup of UNDEX Problem (Adapted from [12])

A general UNDEX event begins with the chemical reaction of the explosive material, which is an unstable chemical substance in a gas, solid, or liquid state. This chemical reaction takes place in two parts: the initial chemical reaction and the detonation process. The initial chemical reaction, which is both exothermic and rapid in nature, is started by the transfer of energy to the explosive material [13]. This transfer of energy is done by a mechanism known as a "detonator" or "igniter," which is made from a more sensitive explosive material than the primary explosive material. As the explosive material is ignited, it reacts and releases energy, and transforms into a more stable state. The product of the reaction is a hot gas at an extremely high pressure [14]. This chemical reaction is called an explosion or explosion reaction.

If the pressure created by the initial chemical reaction in the detonator is large enough, a thermo-mechanical shock wave, known as the "detonation wave," is created. The detonation wave then propagates at a supersonic speed through the primary explosive material, which is still in its original state, generating intense heat. Assuming the explosive material is classified as a high explosive, this causes the remaining unreacted explosive material to undergo an explosive reaction as the wave passes through, making the detonation process self-sustaining [13].

The newly formed gaseous products behind the detonation wave have no time to expand before the shock wave passes entirely through the primary explosive due to the high speed of the wave. As a result, the gaseous products are heated and cannot relieve the pressure through

expansion, which produces pressures in the range of two to four million pounds per square inch [13, 14]. This pressure, known as either the "detonation pressure" or "Chapman-Jouget" pressure, is a constant dependent on the type of explosive material used [13]. Given the high speed of the detonation wave, the chemical reactions of the detonation process can be assumed to occur instantaneously for engineering purposes [13].

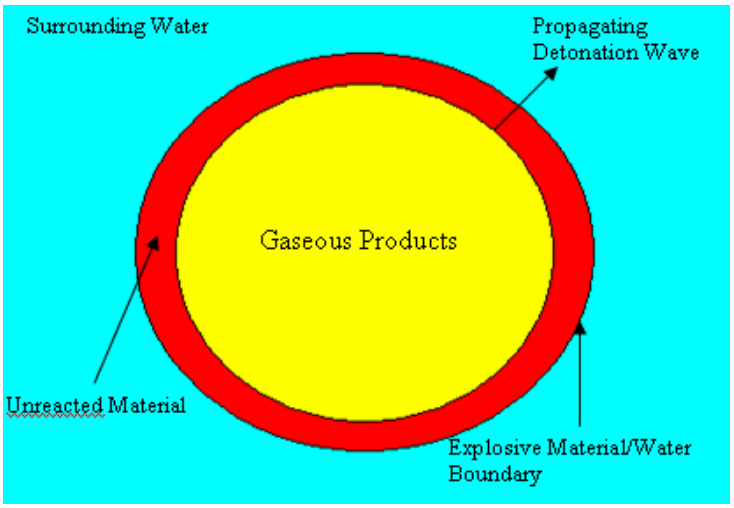

Figure 3 – UNDEX during Detonation Process [15]

All unreacted material has been converted to gaseous products by the time the detonation wave reaches the explosive material/water boundary. The gaseous products are now a very dense, superheated, spherical gas bubble [14]. At this point, the UNDEX detonation process is complete. This thesis will treat the conclusion of the detonation process as the initial condition for an UNDEX event.

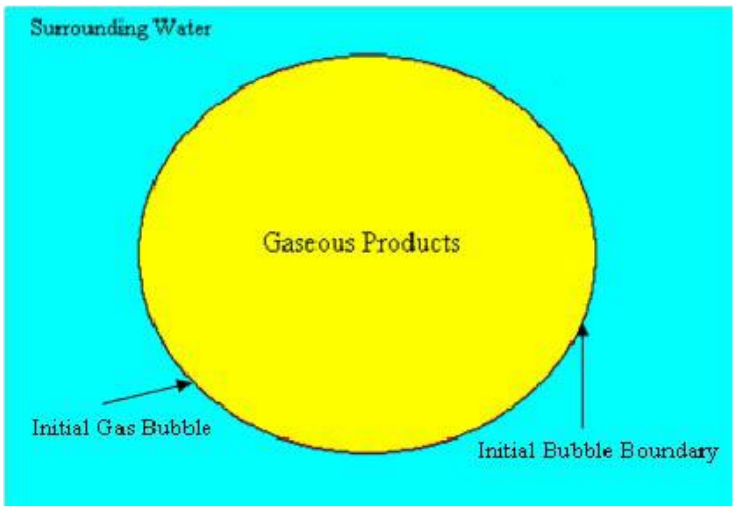

Figure 4 – UNDEX at Instant of Detonation Process Completion [15]

1.2.1 Types

UNDEX events are usually classified as either near-field or far-field, depending on the response of the ship structure to the event. Near-field UNDEX events occur close to the ship and typically result in the plastic deformation or rupture of the ship's hull. Far-field UNDEX events occur further away from the ship, at a distance where the ship response will cause only elastic or elastic-plastic deformation [12]. The distance at which these deformations occur depends on the size and power of the charge and the structural characteristics of the ship. These definitions are outlined in terms of UNDEX phenomena in Figure 5.

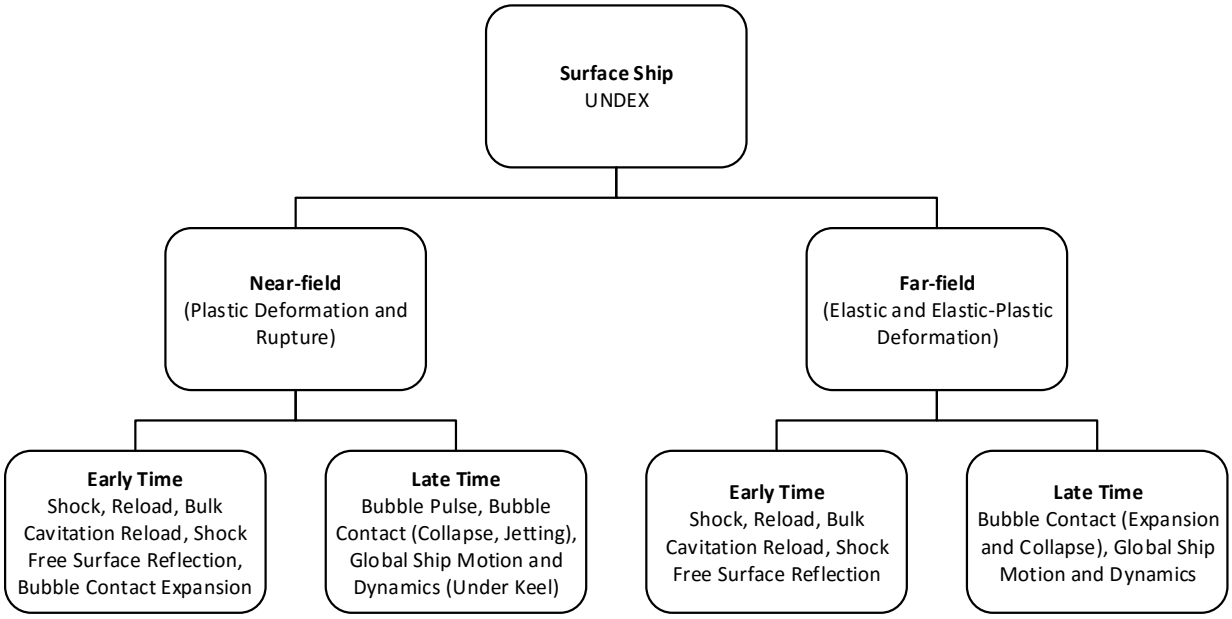

Figure 5 – Classification of UNDEX, Recreated from [16]

1.2.1.1 Far-Field Underwater Explosion

A far-field UNDEX event can cause significant shock damage to systems inside the ship [17]. Early time response is the result of the shock wave contacting the ship, while late time response is limited to lesser global ship motion and dynamics. The potential exists for additional late time response caused by the bubble expanding or collapsing while in proximity to the hull. The effect of an explosion can be divided into response due to the shock wave and response due to the gas bubble [17]. For the purpose of this thesis, a far-field UNDEX event is defined as an UNDEX event that is far enough away from the ship to not cause hull rupture or produce bubble pulses which influence the late time response of the ship.

1.2.1.2 Near-Field Underwater Explosion

Every aspect of the UNDEX event must be considered for a near-field UNDEX analysis [11]. A near-field UNDEX event can excite the structure globally and locally in both the early and late timeframes. Early time response is the result of the shock wave or bubble contacting the ship, while late time response is the result of bubble pulse loading or the bubble collapsing or jetting while in contact with the hull. Ship response to near-field UNDEX events typically results in the plastic deformation or rupture of plating, while deformation or failure of the hull girder is possible under certain conditions. This thesis will focus on the global motion and dynamics of the hull girder caused by multiple bubble pulses from a noncontact, under keel UNDEX event.

1.2.2 Phenomena

The first UNDEX phenomenon to occur after the completion of the detonation process is the shock wave. The shock wave is a compressive high pressure wave emitted from the initial explosion gas bubble as a continuation of the detonation wave. The shock wave shape is characterized by a nearly discontinuous rise in pressure followed by a brief period, on the order of a few milliseconds at most, of exponential decay [14]. The maximum pressure reached by the shock wave is known as the "peak" pressure and plays an important role in calculating the early structural response of a ship to an UNDEX event [14, 12, 11]. The shock wave propagates in the water as a spherical wave, initially faster than the speed of sound. As the shock wave moves further from the origin of the explosion, its propagation speed slows to the speed of sound, its peak pressure gradually reduces, and its shape becomes more elongated [13,14]. Figure 6 illustrates this occurrence.

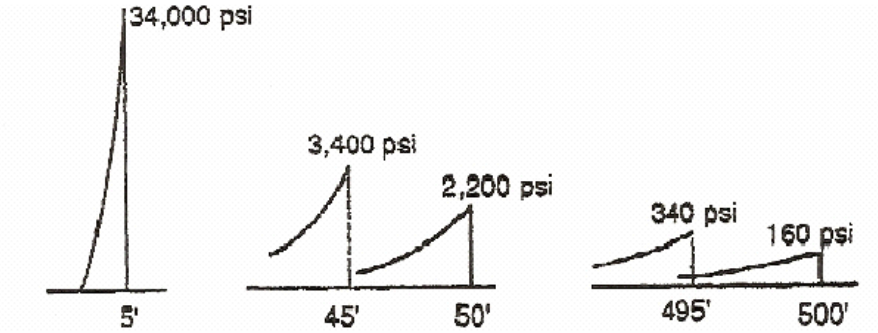

Figure 6 – Shock Wave Profiles at Various Distances from Explosion Origin [14]

When the shock wave contacts the hull of a surface ship, it creates a pressure loading on the hull that is characterized as an instantaneous rise to peak pressure followed by an exponential decay [12]. This loading imparts an upward or inward acceleration onto the structure, which eventually forces the structure to move faster than the surrounding water. This places the water under tension, which the water is not capable of sustaining, and a cavitation region is formed at the interface of the hull and water [12]. This cavitation region, termed the local or hull cavitation region, results in a condition of zero hydrodynamic loading on the ship [18]. The local cavitation region will remain until the ship structure reaches its maximum upward velocity, or kick-off velocity, and begins to slow. The slowing of the structure allows the local cavitation region to close, which causes the structure to be reloaded [12].

The shock wave will also encounter the free surface and seafloor bottom boundary. It will reflect off of these boundaries, producing a tensile wave at the free surface and a compression wave at the bottom boundary. The tensile wave is similar in magnitude to the shock wave, while the compression wave has a much smaller magnitude [14, 12]. However, it is often assumed that the bottom boundary is far enough away so that it will not affect the behavior of other shock wave elements [11]. The low net pressure at locations near the free surface where the incident shock wave and reflected tensile wave meet may result in a large bulk cavitation region, the size of which is dependent on the location and size of the explosion [19]. This region is symmetric about the vertical axis of the explosion origin, with an upper boundary and lower boundary. The locations of these boundaries are influenced by the environmental, incident shock wave, and reflected tensile wave pressures and their decay rates. The general shape and position of this region is shown in Figure 7. After some time, the cavitation region closes in a zipper-like manner, which produces a pressure wave known as the cavitation pulse. The cavitation pulse can potentially load the ship with pressure loads more damaging than the initial shock wave impact, depending on the proximity of the ship to the pulse location [19]. This is the last event of the shock wave early time response of the ship to the UNDEX event. These events, which have a duration on the order of a few milliseconds, can cause significant damage to internal components of the ship, but have little effect on the ship's global motion.

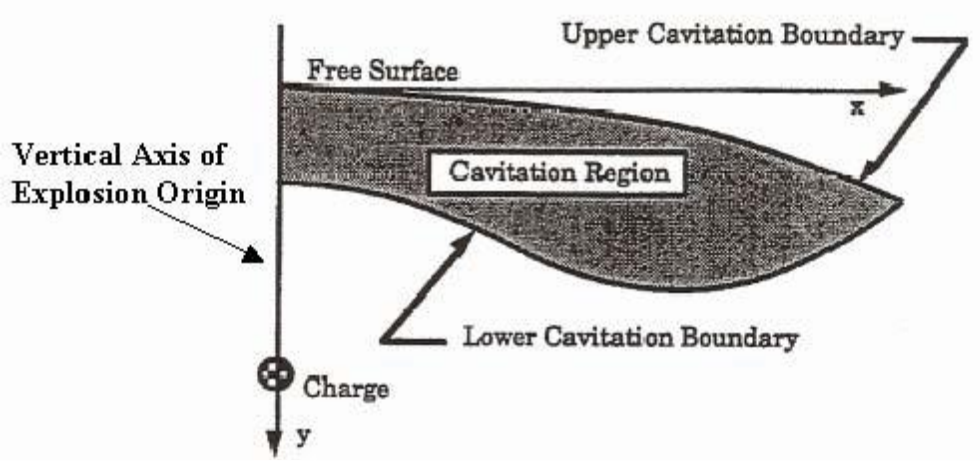

Figure 7 – Bulk Cavitation Region [19]

Recall that after the shock wave was emitted by the explosion at the conclusion of the detonation process, what remains is the dense, superheated, spherical gas bubble. The pressure inside of the bubble, though somewhat lower after the release of the shock wave, still exceeds the hydrostatic pressure of the surrounding water, which causes the bubble to rapidly expand in an attempt to reach hydrostatic equilibrium [14]. The expansion of the bubble reduces the internal pressure and creates a flow of water moving away from the bubble. As the internal bubble pressure reaches the hydrostatic pressure, the gases continue to expand due to the inertia of the outward flowing water, causing the bubble pressure to drop below the hydrostatic pressure [14]. Once the momentum of the water is depleted by the pressure difference, the bubble is at its maximum radius and its minimum internal pressure. The greater hydrostatic pressure then begins to force the bubble to contract, increasing the internal bubble pressure. The bubble will continue to contract until the internal pressure stops the contraction [14]. At this instant, the bubble is at its minimum radius and the internal bubble pressure is again greater than the hydrostatic pressure. The expansion and contraction process repeats until the bubble collapses or runs out of energy. Energy is dissipated with each cycle, meaning each successive oscillation will have a shorter duration, smaller maximum radius, and larger minimum radius [14]. The expansion and contraction oscillation of the bubble is illustrated in Figure 8.

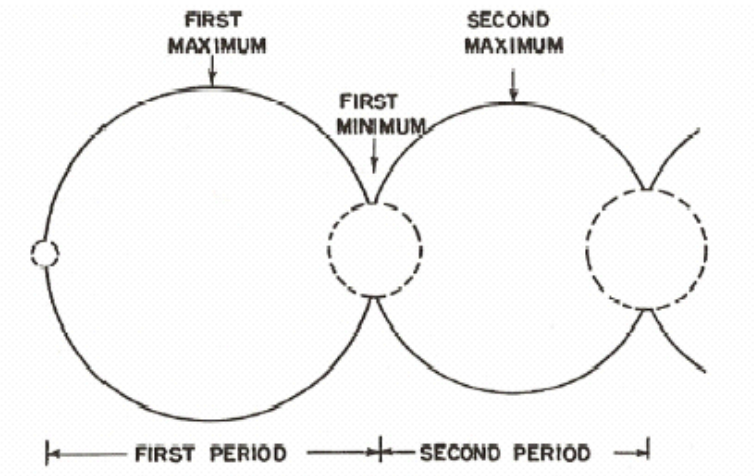

Figure 8 – Gas Bubble Oscillation [14]

At the point where the internal bubble pressure is at a maximum (and the radius is at its minimum) in the oscillation cycle, secondary pressure waves, known as bubble pulses, are radiated outward from the bubble [14, 12]. Bubble pulses are a result of the high pressure gases inside of the bubble accelerating the surrounding water while attempting to reach hydrostatic equilibrium. They propagate at the speed of sound in water, but do not display the discontinuous rise in pressure followed by exponential decay characteristic of the shock wave [14, 18]. Bubble pressure pulses feature a gradual rise to a peak pressure, followed by a similar gradual decay to hydrostatic pressure. The rise and decay of the bubble pressure pulses are concave in form, as shown in Figure 9, and occur on the order of milliseconds to one tenth of one second, depending on the location of the bubble and amount of energy still in the system. The peak pressure from the first bubble pulse is approximately ten to twenty percent as large as the peak shock wave pressure and decreases in magnitude with each cycle [14].

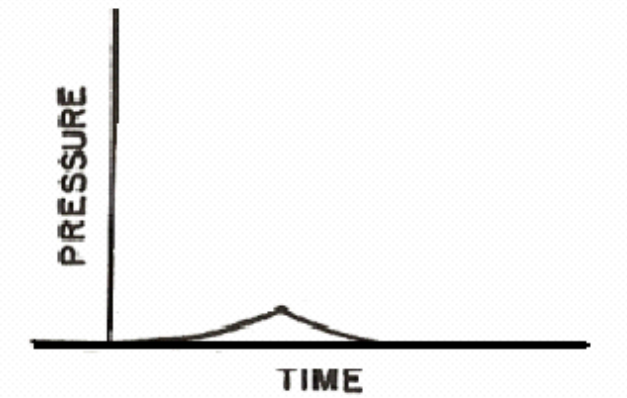

Figure 9 – Typical Bubble Pulse Shape [14]

As the bubble is oscillating, it is also migrating towards the surface due to the buoyancy of the gas products. The speed of migration is affected by the size of the bubble and the motion of the surrounding fluid. During the early expansion, very little migration occurs because the bubble and the hydrostatic force acting on it, which is equivalent to the displacement of the bubble, are small [20]. When the bubble is large, both the buoyancy force and inertia of the fluid surrounding it, commonly referred to as added mass, are large, resulting in minimal displacement. However, the bubble is accelerating upward and the water surrounding the bubble is acquiring significant momentum. As the bubble contracts, the displacement and added mass of the bubble both decrease significantly, but the momentum produced while the bubble was large is still present. This results in the bubble migrating upward quickly when near its minimum [20]. While the bubble is migrating quickly, the bottom surface of the bubble inverts and forms a jet which penetrates through the bubble, producing a toroidal shape [20]. The bubble will regain an approximately spherical shape while it expands at the beginning of the second cycle [20]. The bubble migration and pulse behavior is shown in Figure 10.

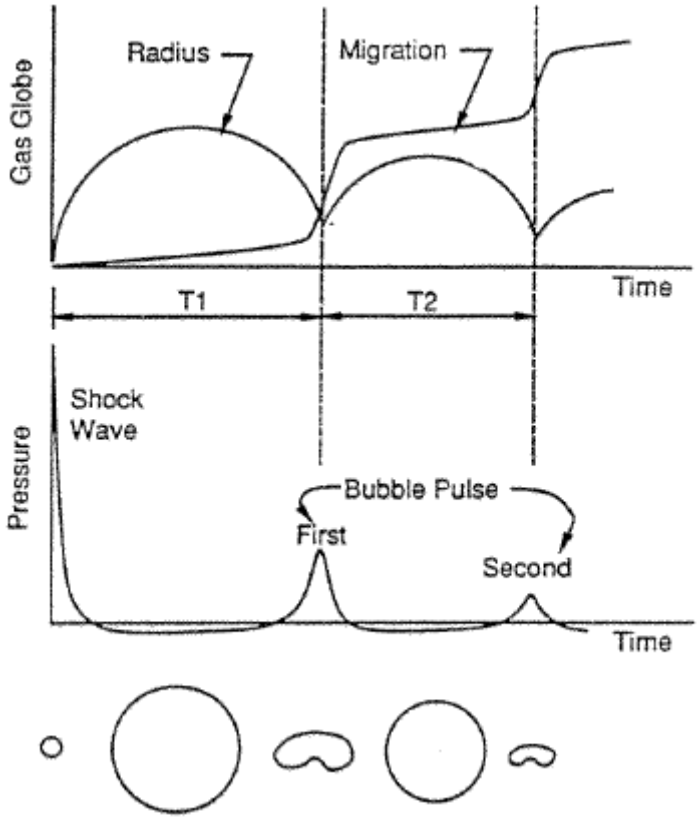

Figure 10 – Bubble Migration and Pulse Behavior [12]

Bubble migration has two significant effects on the bubble pulse. First, it brings the location of the pulse source significantly closer to the ship [20]. The second effect is the reduction of the peak pressure and an increase in the duration of the bubble pulse. This combination results in the impulse, or area under the pressure-time curve, of pulses from both migrating and non-migrating bubble being approximately equal [20]. Therefore, bubble migration does not affect the impulse of the bubble pulse, which is important when considering the motion of a ship above the bubble [20]. A comparison of the bubble pulse shapes are shown in Figure 11.

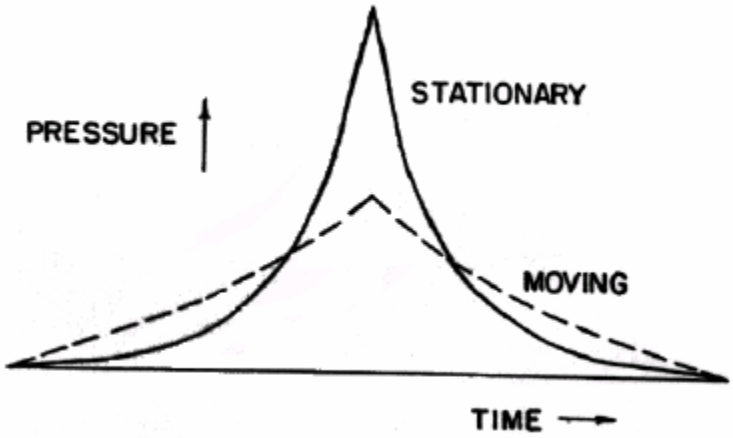

Figure 11 – Bubble Pulse Shape with and without Migration [14]

The primary reason for the bubble radius, period, and pulse magnitude decreasing with each successive pulse is loss of energy. It has been experimentally determined that approximately 47% of the total explosion energy remains in the initial gas bubble after the shock wave has passed. The first bubble expansion and contraction period results in 13% of the total explosion energy dissipated from the bubble. The emission of the first bubble pulse consumes 17% of the total explosion energy, leaving 17% for the remaining pulses [12, 18]. This results in a reduction of available energy of approximately 64% during the first bubble pulse. It has been determined in other studies that between sixty and seventy percent of the original bubble energy is lost during the first cycle, with an additional fifty to sixty percent loss of remaining energy during the second and later pulses [14, 21, 22].

Strongly migrating and non-migrating or slightly migrating bubbles have different energy dissipation mechanisms. Non-migrating bubbles primarily lose energy through the instability of the gas-bubble interface late in the collapse phase through a spraying of the less dense and cooler fluid, the water, into the denser and hotter fluid, the gas. This is known as the Taylor surface

instability [20]. This mixing of fluids decreases the temperature of the gas inside of the bubble, and, therefore, its pressure and energy. For strongly migrating bubbles, this instability does not occur in a significant manner. However, when the bubble is migrating at high speeds, it transfers momentum and energy to the water following the bubble. This results in the wake forcing the lower surface of the bubble to approach the upper surface of the bubble as the upper surface begins to slow as the bubble expands, producing the toroidal shape discussed earlier. This wake is powerful enough to possibly penetrate the bubble, causing the formation of a vertical water jet. This phenomenon is known as the wake theory [20]. Despite these drastically different dissipation mechanisms, migrating bubbles dissipate approximately the same amount of energy as non-migrating bubbles [20].

If the explosion occurs on the seafloor, the bubble will initially expand into a hemispherical form due to the presence of the rigid boundary. The bubble will sit on the seafloor early in its oscillation, but can eventually break away from the bottom due to its buoyancy. If the bubble breaks away from the seafloor, it will migrate and oscillate similar to bubbles formed in open water [18].

The bubble pulses are the second UNDEX-related phenomenon to reach the hull of the ship. The bubble pulses are unlikely to cause significant local damage to ship plating unless they are emitted close to the hull, as they are significantly weaker than the shock wave [18]. The first bubble pulse may contribute to shock wave damage depending on its phase when it strikes the hull [12]. Cavitation regions do not develop as a result of bubble pulse loading.

Bubble pulses are typically ignored for charges far away from the ship, as they are assumed to dampen and become insignificant before reaching the ship [11]. However, bubble pulses from UNDEX at intermediate standoff distances, specifically those positioned directly under the ship, can result in whipping. Whipping is the flexing or bending motion of the hull girder, usually in the vertical plane, in its low frequency modes. For close, but noncontact UNDEX events, these motions can be severe enough to cause the hull girder to buckle, break, or lose all stiffness at the point of failure [23]. The probability of this type of damage occurring increases if the frequency of the bubble pulses is close to the natural vertical vibration frequency of a ship's hull girder [12]. The period of bubble motion from large explosions typically is similar to the fundamental two-node whipping frequency of smaller ships, with both taking between three-tenths and one second

to complete an oscillation [23]. Examples of the damage caused by severe whipping are shown in Figure 12 and Figure 13.

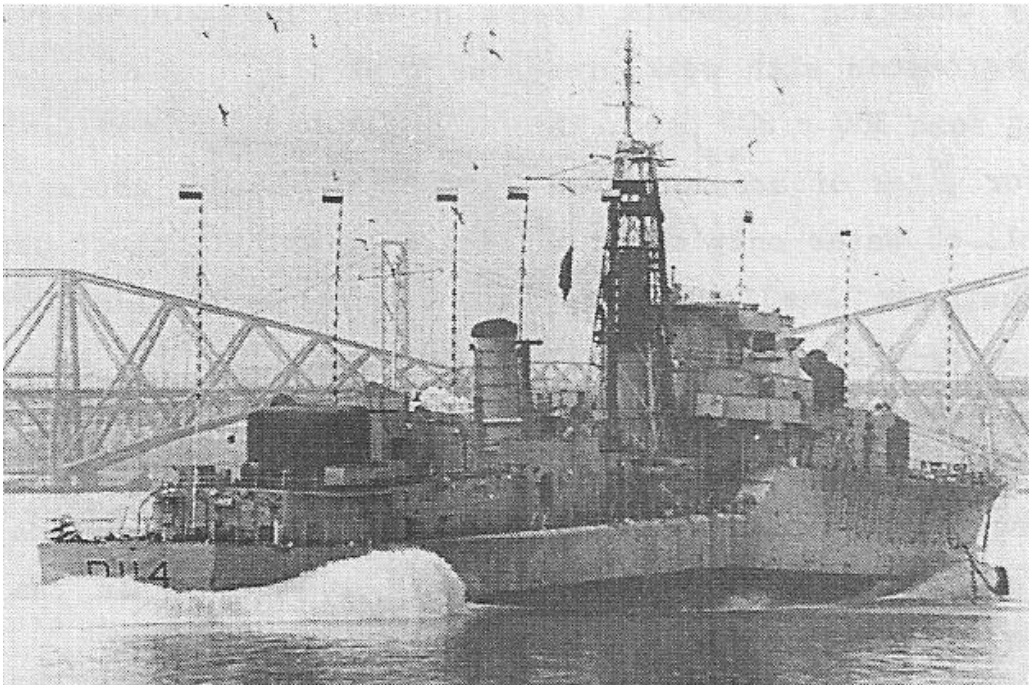

Figure 12 – Damage from Severe Whipping [23]

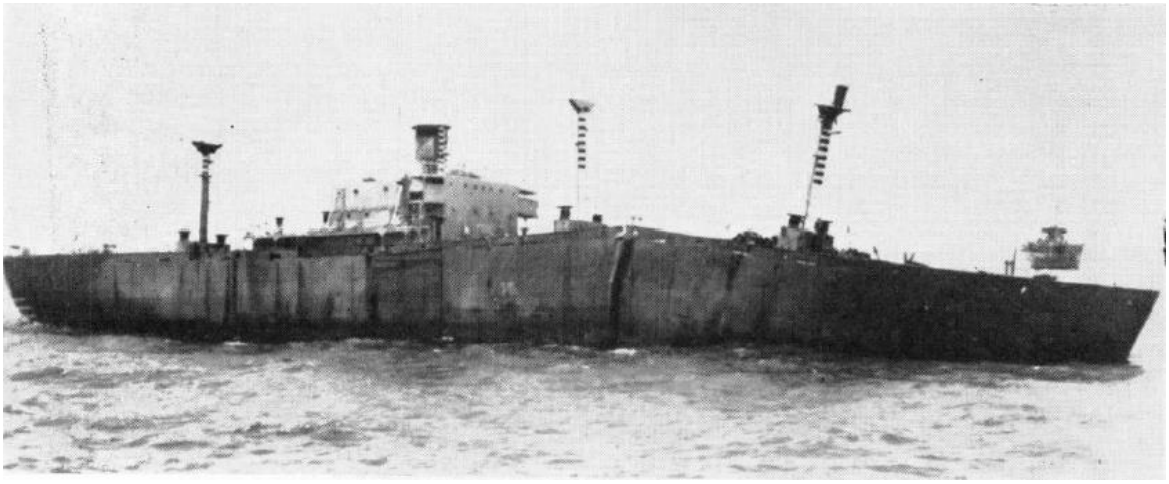

Figure 13 – Failure of Liberty Ship Hull Girder due to Noncontact, Under Keel UNDEX [18]

Bubble pulse loading is the primary driver of UNDEX-induced ship whipping, as ship whipping from shock wave effects is not a serious problem. This is primarily due to the high velocity imparted on the hull plating by the shock wave not being efficiently transferred to the total structure. This inefficient transfer of momentum is a result of the hull plating mass being small relative to the ship total mass and added mass in the vertical direction. This momentum

transfer, characterized by a high velocity on a small mass being transferred to a low velocity on a large mass, generally results in only about one percent of the shock wave energy resulting in global whipping motion [23].

The last UNDEX-related phenomenon to reach the hull is the gas bubble itself [11]. A migrating bubble is attracted to a rigid surface and repelled by a free surface [14, 18]. Therefore, if the bubble is migrating near the surface close to the ship, the bubble is likely to migrate towards the ship and eventually come into contact with it. Bubble contact presents two potential types of loading.

The first type of gas bubble loading is produced by the outward flowing water around the bubble during expansion impacting the hull. This loading imparts high pressure onto the hull over a much longer duration than the shock wave. The impulse from this event is capable of creating significant damage to localized areas of the hull, which can be more severe than the damage caused by the shock wave in extreme cases [11].

The second type of gas bubble loading occurs when the bubble collapses onto the hull of the ship. As the bubble contracts in close proximity to the hull, the water column under the bubble caused by the vertical migration of the bubble pushes upward through the bubble with significant speed [20]. This phenomenon, known as a bubble jet, results in a local pressure loading capable of puncturing the hull [12].

The arrival of UNDEX phenomena at the water surface is evident by certain visual cues, all of which are illustrated in Figure 14. The occurrence of the spray dome and the slick on at the water surface indicate that the shock wave has reached the surface. The spray dome is the vertical upheaval of white water on the surface produced by the vertical velocity given to the water surface when the incident shock wave is reflected. It typically occurs directly above the charge [14]. The slick is a ring of darkened water on the surface, the edge of which indicates the furthest points the shock wave has reached on the surface [14]. The darkness of the slick is a result of the differing water conditions produced by the reflection of the shock wave and the cavitation region [14]. The arrival of the bubble at the surface is marked by the plume. The plume is a column of white water and explosive gas products that is thrown vertically into the air [14]. The size and duration of each of these visual cues are related to the depth, location, and size of the explosive charge, with only the slick being visible for deep UNDEX events [14].

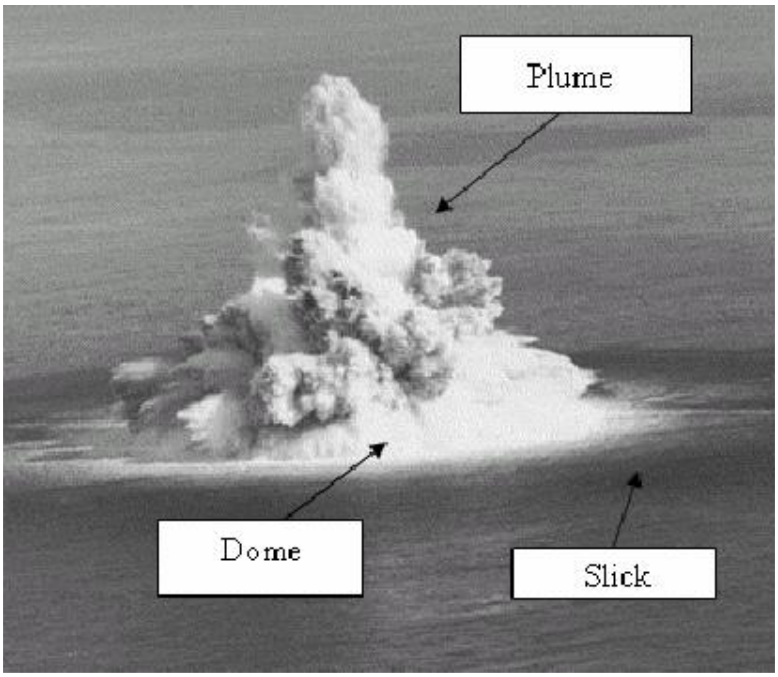

Figure 14 – Plume, Spray Dome, and Slick [11]

1.2.3 Similitude Equations

Analytical equations representing the physics of UNDEX are very complex [11]. The method of similitude offers a simplified way to calculate the characteristics of an UNDEX event. Similitude relations yield information on the various properties of the shock wave, gas bubble, and secondary pressure pulses, such as pressure, impulse, energy, and basic time histories [14]. This basic approach is applied in this thesis, so a thorough understanding of the similitude equations is important.

The similitude equations use a limited number of variables coupled with experimentally determined constants to approximate the characteristics of UNDEX events. The primary variables used are the charge weight, explosion depth, and a point of interest in the explosive field. The method, referred to by Cole as the "principle of similarity," assumes that if the variables of two separate explosions are different by some ratio, the characteristics of the explosions are the same at two corresponding points of interest scaled by the same ratio [14].

Similitude equations do not accurately reflect the physics that occur during an UNDEX event, but they provide a good understanding of the behavior of UNDEX events. In some cases, similitude equations only apply to a limited range of combinations of their input variables. The similitude equation for bubble pulse maximum pressure is generally limited in its applicability to

depths of 142-1209 meters, while the equation for bubble pulse duration is limited to depths greater than 182 meters with an unknown upper depth limit. The equations for gas bubble periods and maximum radii are usually assumed to be valid regardless of the UNDEX conditions [24].

A number of assumptions are required to derive and use the similitude equations. These assumptions and the impact they have on the derivation and applicability of the theory are outlined in Table 3. The most significant assumptions include assuming no effects from boundary surfaces, termed a freewater explosion, and that the gas bubble does not migrate [24, 25].

Table 3 – Assumptions Required for Similitude Equations (Adapted from [11])

Assumption	Impact
No boundary surface effects	No reflection of shock wave or bubble pulses. No cavitation or free surface effects. All similitude equations based on explosions that took place significantly far away from boundary surfaces.
Freewater (infinite fluid) explosion	Bubble reaches its maximum before it reaches the surface.
No gas bubble migration	Shape of bubble pulse unaffected by moving bubble. All similitude equations and constants based on explosions that resulted in minimal bubble migration.
Spherical gas bubble	Allows bubble radius to be found using similitude. Effects volume of bubble used in energy equations
Incompressible fluid/no energy losses in bubble oscillation	Creates error in hydrodynamic bubble energy calculations.
Irrotational fluid	Allows potential flow to be used to develop energy equations.
Radius-time curve symmetrical about bubble maximum time	Ignores any energy lost between bubble minimums.

1.2.3.1 Gas Bubble

The radius-time history of the gas bubble can be estimated through coupling similitude equations with hydrodynamic methods [14]. The similitude equations for the period, T_n, and the maximum bubble radius, $A_{max,n}$, of the n^{th} bubble pulse are:

$$T_n = K_n \frac{W^{1/3}}{Z_{0,n}^{5/6}} \tag{2}$$

$$A_{max,n} = J_n \frac{W^{1/3}}{Z_{0,n}^{1/3}} \tag{3}$$

where W is the charge weight in kilograms (kg), $Z_{0,n}$ is the hydrostatic pressure head at the bubble center at the beginning of the nth pulse in meters, K_n is the period constant for the nth pulse, and J_n is the radius constant for the nth pulse [26, 27]. The hydrostatic pressure head is calculated as:

$$Z_{0,n} = d_n + 10 \tag{4}$$

where d_n is the depth of the bubble center at the beginning of the nth pulse in meters. The additional ten meters included represent atmospheric pressure above the water surface. The decision to utilize the depth at the beginning of each oscillation rather than the initial explosion depth, as done during the original derivation, better compensates for the effect of migration. This leads to more accurate approximation of characteristics for migrating bubbles [22].

Values for the period and radius constants for the first three pulses for TNT explosions are shown in Table 4. These values were determined by Swift and Decius [26, 27] to have strong agreement with experimental data. The experiments consisted of numerous small charges detonated in deep water at large depths to limit bubble migration and minimize surface effects [26]. The radius constant for the first pulse is reflective of the bubble behavior resulting from large charge explosions because the simulations done in this thesis will focus on large charge explosions. This value is approximately four percent larger than the value for the small charge explosions. Radius constants for the second and third pulse were not given for large charge explosions, so the small charge explosion values were increased by four percent, consistent with the behavior from the first pulse.

Table 4 – Similitude Bubble Time-History Constants (*=adjusted)

Pulse Number	**Period Constant (K_n)** $\left(s \cdot m^{5/6} \cdot kg^{-1/3}\right)$	**Radius Constant (J_n)** $\left(m^{4/3} \cdot kg^{-1/3}\right)$
1	2.11	3.5
2	1.57	2.36*
3	1.33	1.83*

Though the effects of boundaries and surfaces were ignored in the derivation of equation (2), a simple correction factor exists to adjust the bubble periods to account for the effect of the free surface [22]. The free surface corrected bubble period, $T_{FS,n}$ can be calculated as:

$$T_{FS,n} = T_n \cdot \left(1 - \alpha \frac{A_{max,n}}{d_n}\right) \tag{5}$$

where α is the free surface correction coefficient [22]. The value of this coefficient is not a constant, as it is dependent on the ratio of maximum radius to depth. However, analysis by Snay determined that a value for α of 0.1 is appropriate for most explosion scenarios, specifically those not too close to the surface [22]. The determination is appropriate for the work of this thesis and is applied to similitude results when necessary. The presence of a free surface does not have an effect on the maximum or minimum bubble radii, so no adjustment is necessary to these values [22].

As it is assumed that the radius-time curve is symmetric about the time of the bubble maximum, the time of the bubble maximums can be estimated from the bubble periods [25]. Given this assumption, the approximate time at which the bubble reaches its n^{th} maximum and minimum radii can be estimated from the period predictions:

$$T_{max,n} = \sum_{i=1}^{n-1} T_i + \frac{T_n}{2} \tag{6}$$

$$T_{min,n} = \sum_{i=1}^{n} T_i \tag{7}$$

The bubble minimum radius can be approximated as:

$$A_{min1} = f W^{1/3} \tag{8}$$

where f is the bubble minimum radius similitude constant, which is equal to 0.113 m/kg$^{1/3}$ for TNT explosions [25]. Similitude equations for subsequent bubble minimum radii were not given in any of the referenced works.

Total vertical bubble migration distance at the first minimum can also be approximated for TNT explosions as:

$$m = 12.2 \frac{W^{1/2}}{Z_0} \tag{9}$$

where all variables are in metric units [12]. The bubble migrates approximately half of this distance between the first and second minimums [12].

1.2.3.2 Bubble Pulse

The important characteristics of the bubble pulse are the time of arrival at a point of interest, the peak pressure, the impulse, and the duration. Similitude equations can be used to estimate most of these characteristics, but no direct method exists for the time of arrival of the bubble pulse [11]. The bubble pulse begins to propagate at the bubble minimum [14]. The arrival time, t_{BP}, is calculated as:

$$t_{BP} = \frac{R}{u} \tag{10}$$

where R is the distance from the bubble center at the time the bubble pulse is emitted to the point of interest in the fluid and u is the estimated pulse velocity calculated as:

$$u = \pi/2 \left(\frac{A_{max1} - \left(\frac{W}{\rho_{TNT} \cdot g}\right)^{1/3}}{t_{max1}} \right) \tag{11}$$

where ρ_{TNT} is the density of TNT, g is the acceleration due to gravity [11]. The maximum pressure of the bubble pulse, P_{BP}, in kilopascals at a distance R from the bubble center is calculated as:

$$P_{BP} = K_{BP} Z_0^{1/6} \left(\frac{W^{1/3}}{R} \right) \tag{12}$$

where K_{BP} is the bubble pulse maximum pressure similitude constant equal to 2917 $m^{5/6}/kg^{1/3}$ [24]. The impulse of the bubble pulse, I_{BP}, in kilopascal-seconds at a distance R from the bubble center is calculated as:

$$I_{BP} = K_{IBP} Z_0^{-0.4} \frac{W^{2/3}}{R} \tag{13}$$

where K_{IBP} is the bubble pulse impulse similitude constant equal to 85.2 $m^{1.4}/kg^{2/3}$ [24]. The duration of the bubble pulse, τ_{BP}, is estimated from the maximum pressure and impulse as [11]:

$$\tau_{BP} = \frac{I_{BP}}{P_{BP}} \tag{14}$$

1.3 Literature Survey

The ability to predict the damage to ships from UNDEX events is an important aspect of naval ship design. The development of a method capable of accurately predicting the global response of the hull girder to bubble pulse loading with limited resource requirements could help

incorporate an often overlooked phenomenon of surface ship UNDEX effects into the early-stage ship design process. This thesis combines and improved on earlier methods to accomplish this objective.

1.3.1 UNDEX Bubble Models

The first requirement necessary to develop an UNDEX-induced ship whipping method is the selection of an appropriate UNDEX bubble model. There are many bubble models in existence, a few of which are discussed in the following sections.

1.3.1.1 Rayleigh-Plesset Equation

The Rayleigh-Plesset (RP) equation is an analytical method used to approximate the behavior of underwater bubbles that is commonly applied to UNDEX bubbles [28, 29]. It is derived by applying conservation of mass and conservation of momentum to the motion of the bubble surface and utilizing boundary conditions at the bubble surface [28, 30]. Some of the significant assumptions made during the derivation of the RP equation for UNDEX include: spherical bubble, bubble begins as a sphere of high pressure explosion products (ignore explosion process), no bubble migration, no loss of energy during bubble oscillation, zero mass transport across the gas/water interface, inviscid fluid, incompressible liquid, and no surface effects [29, 28].

Several equations have been developed based on the RP equation that eliminate some of the assumptions, most notably the inclusion of compressibility effects, bubble migration, and energy dissipation mechanisms [27, 28, 31]. These RP-based equations require a numerical ordinary differential equation (ODE) solver, such as a fourth order Runge-Kutta method, to integrate the equation and solve for the bubble time history [27, 29]. Initial conditions can be calculated from the similitude relations at the end of the shock wave phase of the UNDEX event [31, 29]. This method produces bubble characteristic time histories that can be tuned to accurately represent experimental data and can be solved quickly with limited computer resources. Fluid motions are imposed on a structure in a separate domain using strip theory or a similar method.

The RP equation presents many advantages for the application of this thesis. It is a simple method capable of accurately calculating bubble behavior for multiple pulses. Variations of the equation exist that include many important effects that are ignored in similar models. Also, the

equations do not require significant resources to calculate the bubble response. However, equation derivations and fluid acceleration equations are not as readily available as other methods. Also, a whipping model that utilizes this bubble model is limited by the separate domain assumption.

1.3.1.2 Potential Flow

The potential flow method is another analytical method of defining an UNDEX bubble. This type of model utilizes a point source of time-dependent strength, which is related to the energy of the explosive charge, to represent the pulsating bubble [32, 20, 21, 33]. Equations for both non-migrating and migrating bubbles exist. The effects of surfaces may also be included or ignored. In addition to the assumptions required when using a potential flow model, such as irrotational, inviscid, incompressible fluid, potential flow UNDEX bubble models typically include the following assumptions: spherical bubble throughout, ignore shock wave effects, bubble gases obey the ideal gas law, and the bubble begins as a sphere of high pressure explosion products, ignoring the explosion process [20, 21]. This method relies on empirical corrections and factors to accurately represent the explosion bubble behavior, specifically for energy dissipation during migration and at the bubble minimums [20]. The equations of motion can be reduced to a system of ODEs that can be solved with a numerical ODE solver [20, 21]. This method produces bubble characteristic time histories that can be tuned to accurately represent experimental data and can be solved quickly with limited computer resources [20]. The fluid motions are typically imposed on a structure that is assumed to be in a separate domain using strip theory or a similar method, which are simply calculated and implemented using potential flow theory [20, 33].

The potential flow method presents many advantages for the application of this thesis. It is a simple method capable of accurately calculating bubble behavior for multiple pulses for migrating and non-migrating bubbles. The equations derived using this method do not require significant resources to calculate the bubble response. Also, many UNDEX-induced whipping models use this method for bubble calculations. However, some of the assumptions made in the derivation of the potential flow bubble model can be included in the more complex variations of the RP equations. Also, a whipping model that utilizes this bubble model is limited by the separate domain assumption. All fluid-structure interaction (FSI) calculations are approximated as a one-way coupled method that utilizes fluid accelerations calculated at the free surface. The direct interaction between the bubble and hull is not included in these calculations.

1.3.1.3 Computational Fluid Dynamics

Computational Fluid Dynamics (CFD) is method of solving fluid mechanics problems through the utilization of numerical methods and specialized algorithms. There are many models and codes utilizing various levels of detail, including finite volume analysis methods, boundary element methods (BEM), Eulerian or Arbitrary Lagrangian/Eulerian (ALE) methods, multiphase flow methods, and numerous others [34, 35]. Within each of these methods, variations may exist in the choice of equation of state for the gas bubble and/or liquid, meshing techniques, compressibility effects, and free surface effects, among other model properties [34]. CFD methods produce fluid responses that can be used as input for structural codes and are not capable of calculating structural response on their own [35]. CFD methods are capable of accurately calculating bubble time histories and many do not require the assumption of a spherical bubble throughout bubble oscillation. They also are capable of calculating the influence of the bubble motion to stationary, rigid surfaces [34]. These methods require significant computer resources and time to obtain solutions and time histories.

The primary advantages of utilizing a CFD method for the application of this thesis include the potential for high accuracy results and the ability to model the physics of bubble-ship interactions, though a specific FSI routine is also required to do so. However, the substantial resource and time requirements needed to perform an analysis is a significant disadvantage.

1.3.1.4 Hydrocodes

Hydrocodes are computational mechanics tools for the simulation of multi-material, compressible, transient continuum mechanics that are capable of simulating the response of both solids and fluids to dynamic stimuli [36]. Hydrocodes generally make fewer assumptions and are more diverse than CFD methods. They solve the more fundamental time-dependent equations of continuum mechanics that CFD methods do not. There are various types of hydrocode meshing techniques which vary the behavior, motion, and location of the mesh within the analysis domain based upon the problem being solved [17, 35, 36]. Hydrocodes require significant computer resources and time to obtain solutions. However, they are capable of performing fluid and structure response calculations simultaneously [36].

The primary advantages of utilizing a hydrocode for the application of this thesis include the potential for high accuracy results and the ability to model the physics of bubble-ship

interactions. The ability to model the problem using a single program or code is also desirable. However, the substantial resource and time requirements needed to perform an analysis is a significant disadvantage.

1.3.2 Ship Structural or Vibration Models

The second requirement in the development of the desired model is the selection of an appropriate structural vibration model for the ship. There are many available methods and tools for analyzing a ship structure, some of which are discussed in the following sections.

1.3.2.1 Beam Theory

Considering the hull girder of a ship to be a free-free beam with varying cross-section is a common assumption among naval architects, as it produces results that are fairly accurate when calculating the first few low frequency modes [20]. The accuracy of this simplification is dependent on the inclusion of added mass, which is usually calculated by strip theory. To better approximate the changes in the ship's properties along its length, the ship is typically assumed to be a series of lumped masses connected by weightless beams of equal length, each representing the properties of the hull cross-section at its midpoint [20, 37].

Beam theory is a simplification of linear elastic theory that relates the deflection of a beam to its internal forces, such as shear and bending moment [37]. The properties of the ship are then used to create a stiffness matrix, which is used in the vibration equation of motion (EOM). The general EOM of the vibrating ship is assumed to be similar to a spring-mass-damper system, with the ship mass and added mass acting as the mass term, the hydrodynamic damping acting as the damper term, and the stiffness matrix acting as the spring term. Only vertical plane motion is traditionally considered for vibration and whipping analysis, though two and three-dimensional beam representations may be used at the cost of greater complexity and increased resource requirements. From the vibration EOM, natural vibration frequencies and mode shapes can be calculated, which serve as the primary methods of representing the elastic motions of the hull girder. Forcing from the fluid is then applied to each mode shape individually to determine how significantly the ship is excited in each mode. The motions from each mode shape are then superimposed on each other to determine the overall motion of the hull girder [20, 37].

The predicted hull girder deflections are used to determine stresses or damage that may occur to the hull girder. Plastic deformations can be included or ignored, which will influence the behavior of the structure. Some methods do account for the effects of plastic deformation, but this adds additional complexity to the model [20, 33]. The beam theory method of representing the structural characteristics and motion of a hull girder has been proven to be a simple method that gives reasonable results, couples easily with fluid forcing, and does not require significant computer resources or time to obtain solutions. However, its accuracy is limited by the approximate ship model and the various assumptions made while developing the method.

1.3.2.2 Finite Element Models

There are numerous versions and types of Finite Element Analysis (FEA) software and codes available, a few of which are specifically developed for ship structural analysis. FEA models are capable of being very accurate on both the local and global scale, and can be made more or less accurate based on the size of the elements. In general, the level of detail and accuracy is inversely proportional to the size of the elements, with greater accuracy being associated with smaller elements. However, the increased detail comes at the cost of increased time and computer resources necessary to complete the analysis. Both static and dynamic FEA programs exist. Many dynamic FEA models do not readily accept a time history of fluid forcing, instead requiring a separate FSI script to communicate between the structure and fluid codes. These methods require significant amounts of time to create full ship models, while analysis times vary significantly based on the type of analysis. The amount of time required for the analysis of single, static load cases is relatively small, while dynamic analysis of the structure in the time domain requires a significant amount of computer resources and time [38, 39, 40].

1.3.2.2.1 MAESTRO Structural Design Software

MAESTRO (Modeling, Analysis, Evaluation, and STRuctural Optimization) is a design, analysis, and evaluation tool specifically tailored for floating structures. MAESTRO is capable of performing structural modeling, static FEA, failure (or limit state) analysis, and optimization for large and complex thin-walled structures at the global and local levels [41, 39]. A ship model can be placed under various predefined or user-defined ship-based static loading conditions and

evaluated for compliance with several structural design standards and methods. The specified static load cases can defined using hydrodynamic conditions, such as a random seaway, hydrostatic balance, or a design wave, or by imposing forces, pressure loads, restraints, or deflections at any point along the vessel. MAESTRO is capable of performing static and quasi-static analyses [41]. After a model has been completed, the majority of MAESTRO analyses do not require significant computation time or resources to complete. MAESTRO also has post-processing capabilities for visualization of results, all of which are in the context of ship structural design.

1.3.2.2.2 Nastran

Nastran is a general purpose FEA solver capable of performing numerous types of analyses on objects and systems of any size, shape, or purpose. It is used extensively in the marine industry to perform both structural and FSI analyses. Nastran requires input and produces output in a specific format through text files, which necessitates the use of preprocessing and post-processing tools to visualize and interpret the problem and its results. Nastran is capable of performing both static and dynamic analyses for linear and nonlinear structural analysis problems. Implicit and explicit solution methods are available depending on the type of analysis chosen. [42, 43].

1.3.3 Conclusion

A potential flow bubble model one-way coupled to the lumped mass beam theory structural model similar to the one described by Hicks [20, 23] was selected for the purpose of this thesis. Similitude relationships and bubble empirical data are used to calibrate and verify the bubble model when required. To determine the extent of the potential damage caused by the whipping motions predicted by the beam theory model, the dynamic response of the structure is applied to a finite element model in MAESTRO as a quasi-static case to assess structural adequacy. The ability of these models and methods to produce meaningful results while requiring limited computer resources and time to set up and solve problems were the primary factors in the selection. In addition, MAESTRO was chosen as the FEA tool because of its specialization in ship structures and its many analysis tools and options. Also, the potential flow bubble model was chosen over the Rayleigh-Plesset based models due to its relative simplicity of including bubble migration in the equations of motion and the availability of fluid acceleration equations and derivations.

1.4 Thesis Objectives

The overall goal of this thesis is to develop a method capable of simply predicting the global response of the hull girder to UNDEX bubble pulse loading with limited resource requirements for use in early-stage ship design. In order to accomplish this goal, the objectives of this thesis are:

- Develop an UNDEX bubble model capable of calculating the bubble behavior for multiple pulses.
- Develop a simple model capable of calculating the whipping response of a ship to an UNDEX event that can be utilized early in the design process and requires minimal computer or manpower resources.
- Incorporate finite element structural analysis into the analysis process without greatly increasing the required computer or manpower resources.
- Determine the most significant and influential variables of the UNDEX-induced whipping problem.
- Determine the UNDEX scenario most likely to cause significant damage or catastrophic hull failure due to UNDEX-induced whipping.
- Make design suggestions to improve ship survivability against the threat of UNDEX-induced whipping.

1.5 Thesis Outline

This thesis describes the development of a simplified underwater explosion-induced ship whipping model and the analysis of the whipping problem using the model and MAESTRO structural design software. Chapter 1 provides background information and motivation for the need to accurately model and simulate UNDEX events and evaluate the vulnerability of a ship to an UNDEX event. A description of the sequence and phenomena of UNDEX events and a discussion of some current methods of modelling these phenomena are presented. Chapter 2 describes the UNDEX-induced ship whipping model developed through this research and discusses its validity. Chapter 3 explains how to extract the necessary data from a MAESTRO model of a sample ship and run a whipping analysis on the same ship using the model described in Chapter 2. The maximum hull girder deflections resulting from an under keel UNDEX event is applied to the ship in MAESTRO as a quasi-static structural analysis case to determine the ability of the ship structure

to withstand the whipping loads. Chapter 4 presents a parametric and sensitivity analysis study of the whipping problem for the sample ship. This analysis is used to determine the dependence of the ship response to charge characteristics and the elements of a worst case scenario. Chapter 5 discusses the conclusions of this thesis and possible future work.

Chapter 2 Underwater Explosion-Induced Ship Whipping Model

2.1 Overview

This chapter describes a simplified mathematical model developed to quickly calculate the UNDEX-induced whipping motions of a ship. This model is based on the model developed by A.N. Hicks [20, 23] with adjustments and modifications to fill in knowledge gaps and improve overall accuracy. In the following sections, the Hicks model, the adjustments made to the Hicks model, and a model assessment are presented.

2.2 Hicks Model

The UNDEX-induced ship whipping model developed by Hicks was derived as a simplified model capable of calculating reasonable results with limited computing capability. The theory, derivations, and equations presented in this section are directly from his referenced works [20, 23, 44]. Hicks makes numerous assumptions and utilizes matrix relationships to simplify the model and keep computation time to a minimum. The model consists of four main components: the UNDEX pulsating bubble model, ship structural model, ship vibration equations of motion, and ship total motion equations. The theory and equations behind each of these sub-models are explained in the following sections.

2.2.1 Underwater Explosion Bubble Model

The following assumptions are made to simplify the physics and calculation of the pulsating bubble model:

- Compressible phase of bubble expansion and its effects are neglected
- Shock wave effects are ignored
- Presence of ship does not affect the motion of the bubble
- No bottom effects (infinite depth of water below bubble)
- Inviscid and irrotational fluid
- Bubble geometry remains spherical throughout
- Adiabatic system (no heat transferred from the bubble gases to the water)
- Explosion gases obey the ideal gas law
- Bubble starts as a sphere of high pressure explosion products

The irrotational, inviscid, and incompressible fluid assumptions allow the use of potential flow theory as the foundation for the bubble model. Assuming that the geometry of the bubble remains spherical throughout each oscillation allows for the use of bubble radius as a defining factor of the bubble dynamics, but ignores the change in shape that occurs near minimums. By ignoring any effects the ship may have on the bubble motion, the ship and bubble are essentially assumed to be in separate fluid domains. This limits the accuracy of the model to scenarios where the bubble is far enough away from the ship to avoid contact with the ship and any rigid surface effects the presence of the ship may cause. Assuming the bubble starts as a sphere of high pressure explosion products and that the shock wave has already left the bubble allows for the use of a simplified initial condition based only on the explosive energy and depth of the charge. Ignoring shock wave effects also assumes the shock wave has a negligible effect on global ship motions. The adiabatic system and ideal gas law assumptions allow the use of the adiabatic equation of state to represent the potential energy of the bubble and assumes the energy in the bubble remains constant during an oscillation.

Given these assumptions, the pulsating bubble is modeled as a vertically migrating potential flow source with time-dependent strength. The geometry for this scenario is shown in Figure 15, with the free surface defined as a contour of zero potential. This is achieved by placing a single negative image bubble above the surface, making the surface a plane of anti-symmetry. The use of a single image bubble is an approximation ignoring higher order terms, as an infinite number of images is required to balance the higher order terms of the velocity potential [21].

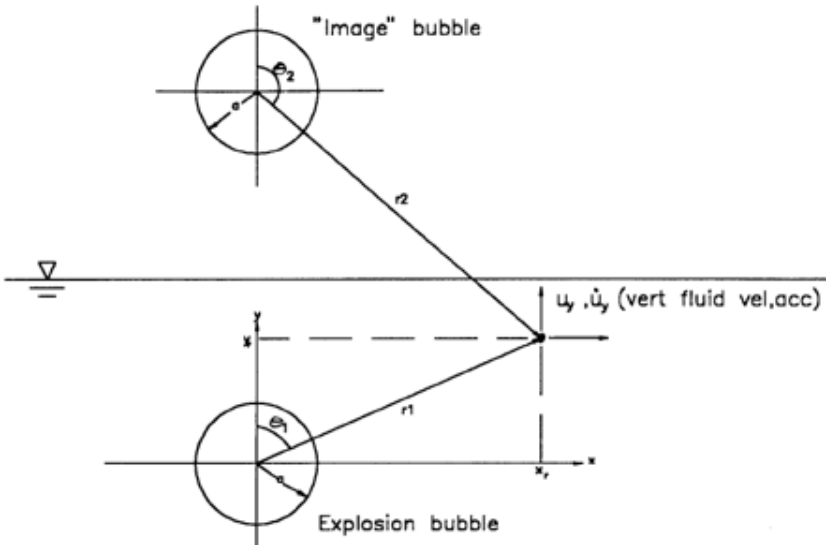

Figure 15 – Geometry for migrating bubble near a free surface [45]

The velocity potential of the migrating bubble for the geometry in Figure 15 is:

$$\phi = \frac{e_1}{r_1} + \frac{e_2}{r_1^2}\cos\theta_1 - \frac{e_1}{r_2} + \frac{e_2}{r_2^2}\cos\theta_2 \tag{15}$$

where e_1 is the strength of the source representing the explosion bubble, e_2 is the strength of the source representing the image bubble, and all other terms are as defined in Figure 15. The source strengths can be represented as:

$$e_1 = a^2\dot{a} \tag{16}$$

$$e_2 = \frac{a^3}{2}\left(v - \frac{a^2\dot{a}}{4d^2}\right) \tag{17}$$

where a is the bubble radius, $\dot{a}$ is the velocity of the bubble surface, v is the vertical velocity of the migrating bubble, and d is the depth of the bubble center.

The vertical velocity of the fluid due to the pulsating bubble, u_y, is defined as the negative gradient of the velocity potential:

$$u_y = -\nabla\phi = -\frac{\partial\phi}{\partial y} \tag{18}$$

By substituting the potential from equation (15) into equation (18), u_y can be calculated at any point in the fluid as:

$$u_y = \frac{e_1 y_r}{r_1^3} - \frac{e_2}{r_1^3}\left[1 - \frac{3{y_r}^2}{r_1^2}\right] \tag{19}$$

where all distance terms are as defined in Figure 15. Assuming this form, substituting equations (16) and (17) for the source strengths, and ignoring terms of order higher than $(a/d)^2$, the kinetic energy of the bubble is:

$$KE = 2\pi\rho a^3\dot{a}^2\left(1 - \frac{a}{2d}\right) + \frac{\pi}{3}\rho a^3 v^2 - \frac{\pi}{2}\rho a^3\dot{a}v\left(\frac{a^2}{d^2}\right) \tag{20}$$

where ρ is the density of water. The potential energy of the bubble is a combination of the potential energy of the hole in the water occupied by the bubble and the internal energy of the explosion gas products, and is represented by:

$$PE = \frac{4}{3}\frac{\pi a^3 p}{\gamma - 1} + \frac{4}{3}\pi a^3 p_\infty \tag{21}$$

where p_∞ is the hydrostatic pressure at the bubble center and p is the explosion gas pressure, which can be calculated using the adiabatic equation of state:

$$p = k_1 p_g^{\gamma} = \frac{k_1 W^{\gamma}}{\left(\frac{4}{3}\pi a^3\right)^{\gamma}} \tag{22}$$

where k_1 is an adiabatic constant, W is the explosive charge weight, and γ is the adiabatic index (ratio of specific heats) of the explosive charge gases [14, 20].

Next, the equations of motion are derived. Conservation of energy is applied to equations (20) and (21), including drag effects, to derive the pulsating bubble EOM:

$$E_0 = PE + KE \approx \epsilon W \tag{23}$$

where ϵ is the explosive energy per unit mass of the charge. The bubble migration equation is given by equating the buoyancy force to the rate of change of momentum. This relationship can be derived from the Lagrangian form of the EOM:

$$\frac{d}{dt}\left[\frac{\partial}{\partial \dot{Z}}(KE - PE)\right] = \frac{\partial}{\partial Z}(KE - PE) \tag{24}$$

where Z is the hydrostatic pressure head at the bubble center, as defined in equation (4) and $\dot{Z}$ is the rate of change of the hydrostatic pressure head, which is equivalent to the bubble vertical migration velocity, v.

The equations of motion are then made non-dimensional and suitable for numerical integration by writing them in terms of the following non-dimensional variables:

Non-dimensional Bubble Radius	$x = {}^{a}/_{L}$
Non-dimensional Time	$\tau = {}^{t}/_{T}$
Non-dimensional Bubble Depth	$\delta = {}^{d}/_{L}$
Non-dimensional Pressure Head	$\zeta = {}^{Z}/_{L}$

(25)

where t is the current time, L is the length scale, and T is the time scale. The length and time scales are defined as:

$$L = \left(\frac{3E_0}{4\pi\rho g Z_0}\right)^{\frac{1}{3}} \tag{26}$$

$$T = \left(\frac{3}{2gZ_0}\right)^{\frac{1}{2}} L \tag{27}$$

where g is the acceleration due to gravity and Z_0 is the hydrostatic pressure head at the initial charge location. The length and time scales are characteristic values derived from dimensional analysis and similar in form to the similitude equations for maximum bubble radius and bubble

period in section 1.2.3.1. They are derived to ensure that the effect of gravity (hydrostatic pressure) is the same in both the length and time domains, which requires the assumption that the only force acting on the water is gravity and the only resistance to flow is caused by the inertia of the water. To make this assumption, it is must also be assumed that the initial energy of the gas inside of the bubble is small, which is true when the bubble is not near its minimum size [14].

From equations (20) through (25), the non-dimensional equations of motion for the migrating bubble near a free surface are:

$$\frac{d}{d\tau}\left[x^3\dot{x}^2\left(1-\frac{x}{2\delta}\right)+\frac{1}{6}x^3\dot{\zeta}^2+\frac{1}{4}x^3\dot{x}\dot{\zeta}\left(\frac{x^2}{\delta^2}\right)+\frac{x^3\zeta}{\zeta_0}+\frac{k}{x^{3(\gamma-1)}}\right]=0 \tag{28}$$

$$\frac{d}{d\tau}\left[\frac{1}{3}x^3\dot{\zeta}\right]=-\left[\frac{3}{4}\frac{x^4\dot{x}^2}{\delta^2}+\frac{x^5\ddot{x}}{4\delta^2}+\frac{x^3}{\zeta_0}\right] \tag{29}$$

where *k* is an adiabatic pressure-volume relationship constant, which can be calculated as [20]:

$$k=\frac{(\rho g Z_0)^{\gamma-1}}{\gamma-1}k_1\left(\frac{W}{E_0}\right)^{\gamma} \tag{30}$$

However, the bubble migrations calculated by this theory are larger than experimental values. To solve this problem, a pseudo drag coefficient, C_D, is developed to slow the migration of the bubble to better match experimental results. It is derived assuming the form of a turbulent wake drag force, F_D:

$$F_D=C_D\left(\frac{1}{2}\rho v^2 A\right) \tag{31}$$

where *A* is the cross-sectional area of the bubble perpendicular to the direction of the migration. The amount of energy removed from the system due to this drag force is:

$$-\frac{dE}{dt}=Fv=\frac{\pi}{2}\rho C_D a^2 v^3 \tag{32}$$

The amount of momentum being lost due to the wake at a specific time is equal to the force required to overcome the wake drag at that same time. Although this assumed force does not accurately represent the physics of the problem, it does provide a simple adjustment to the model which allows for a more accurate representation of experimental results from the theory. Hicks determined the nominal value of C_D to best match the migration patterns observed in experiments to be 2.25 [20]. The non-dimensional equations of motion that include C_D, given by Hicks [20], as derived by G.I. Taylor, are:

$$\frac{d}{d\tau}\left[x^3\dot{x}^2\left(1-\frac{x}{2\delta}\right)+\frac{1}{6}x^3\dot{\zeta}^2+\frac{1}{4}x^3\dot{x}\dot{\zeta}\left(\frac{x^2}{\delta^2}\right)+\frac{x^3\zeta}{\zeta_0}+\frac{k}{x^{3(\gamma-1)}}\right]=\frac{C_D}{4}x^2\dot{\zeta}^3 \tag{33}$$

$$\frac{d}{d\tau}\left[\frac{1}{3}x^3\dot{\zeta}\right]=-\left[\frac{3}{4}\frac{x^4\dot{x}^2}{\delta^2}+\frac{x^5\ddot{x}}{4\delta^2}+\frac{x^3}{\zeta_0}\right]+\frac{C_D}{4}x^2\dot{\zeta}^2 \tag{34}$$

The non-dimensional pulsating bubble equation, (33), and the migration equation, (34), can be reduced to a system of first order differential equations suitable for numerical integration:

$$\begin{gathered}\sigma=\dot{x}\\ \lambda=\dot{\zeta}\\ \dot{\sigma}=-\frac{3}{2\left(1-\frac{\beta x}{2\delta}\right)}\left[\frac{\sigma^2}{x}\left(1-\frac{2\beta x}{3\delta}\right)-\frac{\lambda^2}{6x}+\frac{\zeta}{x\zeta_0}-\frac{(\gamma-1)k}{x^{3\gamma}+1}+\frac{\beta x}{4\delta^2}\left(\frac{C_D\lambda^2}{4}+\frac{\sigma\lambda}{3}-\frac{x}{\zeta_0}\right)\right]\\ \dot{\lambda}=-3\alpha\left(\frac{1}{\zeta_0}+\frac{\sigma\lambda}{x}-\frac{C_D}{4}\frac{\lambda^2}{x}+\frac{\beta x}{4\delta^2}(3\sigma^2+x\dot{\sigma})\right)\end{gathered} \tag{35}$$

where α and β are control variables which are used to include or exclude bubble migration or the free surface effect, respectively, in the analysis. Appropriate values for α and β, and the type of motion each scenario represents, are shown in Table 5. It is important to remember that d is dependent on the vertical position of the bubble relative to the free surface, meaning both d and δ will vary as the bubble migrates. The system in equation (35) can now be integrated with a time-stepping integration procedure using the initial conditions:

$$\begin{gathered}x_0=k^{\frac{1}{3(\gamma-1)}}\left(1+\frac{k^{\frac{1}{\gamma-1}}}{3(\gamma-1)}\right)\\ \dot{x}_0=\sigma_0=0\\ \zeta_0={}^{Z_0}/_{L}\\ \dot{\zeta}_0=\lambda_0=0\end{gathered} \tag{36}$$

A built-in ordinary differential equation (ODE) solver in Matlab, ode45, is used to perform the integration. It is a one-step solver that utilizes a Runge-Kutta (4, 5) formula with a variable time step [46]. Using a variable time step is recommended because the rapid changes in bubble radius that occur near the minimum require a small time step to accurately represent the bubble dynamics,

while a larger time step is appropriate near the maximum when the radius is changing more slowly [20, 45].

Table 5 – Appropriate Values of Control Variables (Recreated from [20])

α	β	Type of Motion
0	0	Non-migrating
1	0	Migrating
1	1	Migrating near a free surface

The vertical fluid acceleration at any point in the fluid, $\dot{u}_y$, can be found by differentiating the vertical fluid velocity, equation (19), using chain rule:

$$\dot{u}_y = \frac{\partial u_y}{\partial t} - v\frac{\partial u_y}{\partial y} \tag{37}$$

which, after differentiation and substitution of u_y gives:

$$\dot{u}_y = \frac{\dot{e}_1 y_r}{r_1^3} - \frac{\dot{e}_2}{r_1^3}\left[1 - \frac{3y_r^2}{r_1^2}\right] - v\left\{\frac{e_1}{r_1^3}\left[1 - \frac{3y_r^2}{r_1^2}\right] + \frac{3e_2 y_r}{r_1^5}\left[3 - \frac{5y_r^2}{r_1^2}\right]\right\} \tag{38}$$

where $\dot{e}_1$ and $\dot{e}_2$ are the time derivatives of the source strengths from equations (16) and (17):

$$\dot{e}_1 = a^2\ddot{a} + 2a\dot{a}^2 \tag{39}$$

$$\dot{e}_2 = \frac{3a^2\dot{a}v + a\dot{v}}{2} - \frac{5a^4\dot{a}^2 + a^5\ddot{a}}{8d^2} + \frac{a^5\dot{a}v}{4d^3} \tag{40}$$

where $\dot{v}$ is the vertical acceleration of the bubble, $\ddot{a}$ is the outward acceleration of the bubble surface, and all other terms are as defined in Figure 15. Each of the fluid acceleration terms in equation (38) represents the contribution of a specific aspect of the bubble motion. The first term measures the contribution of the pulsating bubble. The second group of terms calculates the fluid acceleration due to the buoyancy force acting on the bubble. The third group of terms represents the contribution of the rapidly collapsing and expanding bubble near its minimum and the fluid acceleration due to the vertical momentum of the bubble [20].

The source strengths and their derivatives can also be expressed in terms of the non-dimensional variables and length and time scales:

$$e_1 = \frac{L^3}{T} x^2 \dot{x} \tag{41}$$

$$e_2 = \frac{L^4}{2T} x^3 \left(\dot{\zeta} - \frac{x^2 \dot{x}}{4\delta^2} \right) \tag{42}$$

$$\dot{e}_1 = \frac{L^3}{T^2} (2x\dot{x}^2 + x^2 \ddot{x}) \tag{43}$$

$$\dot{e}_2 = \frac{L^4}{T^2} \left(\frac{3x^2 \dot{x} \dot{\zeta} + x^3 \ddot{\zeta}}{2} - \frac{5x^4 \dot{x}^2 + x^5 \ddot{x}}{8\delta^2} + \frac{x^5 \dot{x} \dot{\zeta}}{4\delta^3} \right) \tag{44}$$

All UNDEX events considered in this analysis use TNT as the explosive. Constants for TNT were determined through extensive testing by Arons [25, 14]. The following constant values, in metric units when required, are used [25, 20]:

$$k \approx 0.0743 \cdot Z_0^{\gamma - 1}$$

$$\gamma = 1.25$$

$$\epsilon \approx 2.051 \cdot 10^6 \left(\frac{J}{kg} \right) \tag{45}$$

$$k_1 = 1.440 \cdot 10^5$$

2.2.2 Ship Structural Model

For the dynamic calculations, the ship's hull girder is modeled as a two dimensional series of 'n' lumped masses connected by 'n-1' weightless beams of equal length capable of moving in the vertical plane. The ship is assumed to have zero forward speed. Each beam is assumed uniform and given the characteristics, such as moment of inertia and shear area, of the cross-section of the ship at the midpoint of the beam. A representation of this model is shown in Figure 16.

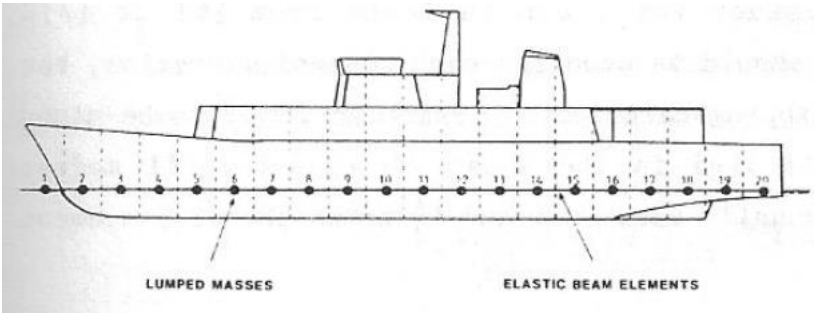

Figure 16 – Lumped Mass/Beam Model Representation [20]

Using this representation, beam theory can be used to determine the vibration characteristics of the hull girder. Beam theory is capable of accurately calculating the frequencies of the first few lowest modes, but only if shear deflections and the added mass of the water near the ship are included. However, it is not reliable for mode shapes with more than five nodes [20]. This is due to the importance of the distortion of plane sections, which is ignored in beam theory, in the calculation of the higher frequency modes. Also, the use of strip theory to calculate added mass becomes increasingly inaccurate at higher vibration frequencies. In addition, combined transverse-vertical modes may begin to appear at higher frequencies. Furthermore, many of the high frequency mode shapes are a product of the lumped mass representation, which requires twenty or more masses to ensure an accurate representation of the ship structure, and have no physical meaning. Since only the first few low frequency modes significantly contribute to UNDEX-induced whipping, a beam theory ship vibration representation is appropriate [20].

The deflections and rotations at the ends of any beam section can be used to determine the forces and moments acting at the beam ends. Using the sign convention in Figure 17, beam theory can be used to derive these relationships:

$$\frac{dF}{dx} = 0$$
$$\frac{dBM}{dx} = -F \tag{46}$$
$$BM = EI\frac{d^2y}{dx^2}$$

where F is shear force, BM is bending moment, E is Young's Modulus of Elasticity for the beam material, I is section moment of inertia of the cross-section, y is the deflection of the lumped mass in the vertical direction, positive upward, and x is the direction parallel to the longitudinal direction of the ship, positive aft. The slope of the deflection curve, dy/dx, is calculated as:

$$\frac{dy}{dx} = \gamma + \frac{F}{A_s G} \tag{47}$$

where γ is the angle of rotation of the deflected beam at the lumped mass, A_s is the area of the cross-section effective in shear (shear area), and G is the shear modulus of the cross-section.

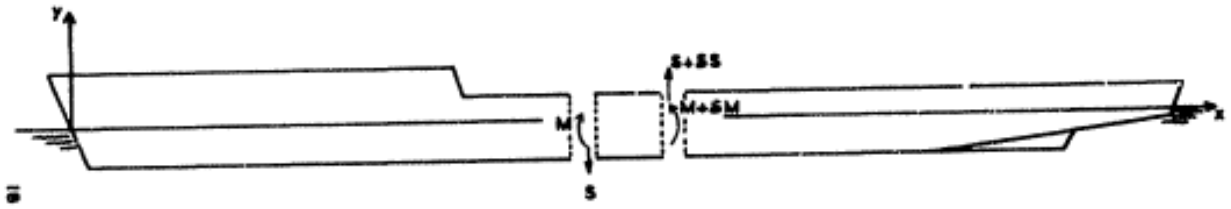

Figure 17 – Sign Conventions for Beam Equations [20]

The beam equations can be obtained by integrating equations (46) and (47), and can be expressed in matrix form as:

$$\begin{bmatrix} y \\ \gamma \\ BM \\ -F \end{bmatrix} = \begin{bmatrix} 1 & x & \frac{x^2}{2EI} & \frac{x^3}{6EI} - \frac{x}{A_s G} \\ 0 & 1 & \frac{x}{EI} & \frac{x^2}{2EI} \\ 0 & 0 & 1 & x \\ 0 & 0 & 0 & 1 \end{bmatrix} \begin{bmatrix} y_L \\ \gamma_L \\ BM_L \\ -F_L \end{bmatrix} \tag{48}$$

where a subscript *L* reflects the condition at the left hand (forward) end of the beam. The moments and shear forces at this end of the beam required to maintain the deflected condition of the beam are given by:

$$\begin{bmatrix} BM_L \\ F_L \end{bmatrix} = \begin{bmatrix} 3\alpha\ell & -\alpha\ell^2(1-\epsilon) \\ 6\alpha & -3\alpha\ell \end{bmatrix} \begin{bmatrix} y_R \\ \gamma_R \end{bmatrix} - \begin{bmatrix} 3\alpha\ell & \alpha\ell^2(2+\epsilon) \\ 6\alpha & 3\alpha\ell \end{bmatrix} \begin{bmatrix} y_L \\ \gamma_L \end{bmatrix} \tag{49}$$

where ℓ is the length of a weightless beam connecting two lumped masses, a subscript *R* reflects the condition at the right hand (aft) end of the beam, and α and ϵ are short-hand variables that represent the structural characteristics of the beam cross-section. For the ith cross-section, α_i and ϵ_i are calculated as:

$$\epsilon_i = \frac{12 \cdot (1+\nu) \cdot I_i}{A_{s,i}\ell^2}; \ \ (i = 1, \dots, n-1) \tag{50}$$

$$\epsilon_0 = \epsilon_n = 0$$

$$\alpha_i = \frac{2EI_i}{\ell^3 \cdot (1+2\epsilon_i)}; \ \ (i = 1, \dots, n-1) \tag{51}$$

$$\alpha_0 = \alpha_n = 0$$

where ν is Poisson's ratio for the hull material, I_i is the moment of inertia of the ith cross-section, $A_{s,i}$ is the shear area of the ith cross-section. The terms inside of the (2 x 2) matrices in equation (49) represent the stiffness of an individual beam section against movement in heave and pitch [47, 48].

For the entire ship, the shear forces, $\vec{F}$, and bending moments, $\overrightarrow{BM}$, needed to maintain a given set of deflections, $\vec{y}$, and bending rotations, $\vec{\gamma}$, are given by:

$$\begin{Bmatrix} \vec{F} \\ \overrightarrow{BM} \end{Bmatrix} = \begin{bmatrix} [A]+[K] & [B] \\ [B]^T & [C] \end{bmatrix} \begin{Bmatrix} \vec{y} \\ \vec{\gamma} \end{Bmatrix} \tag{52}$$

where *[A]*, *[B]*, and *[C]* are tri-diagonal (n x n) matrices which represent the elastic beam characteristics of the hull girder and *[K]* is a diagonal (n x n) matrix containing the buoyancy force per unit immersion at each mass. If the moments in individual beam sections are assumed to be zero, as they have a minimal effect on results [20], equation (52) becomes:

$$\vec{F} = [([A]+[K]) - [B][C]^{-1}[B]^T]\vec{y} = [S]\vec{y} \tag{53}$$

$$\vec{\gamma} = [C]^{-1}[B]^T\vec{y} \tag{54}$$

where *[S]* is symmetric and represents the stiffness matrix for the hull girder.

The elements of matrices *[A]*, *[B]*, and *[C]* are calculated as:

$$\begin{gathered} a_{i,i} = 6 \cdot (\alpha_i + \alpha_{i-1});\ \ (i = 1, \dots, n) \\ a_{i,i+1} = a_{i+1,i} = -6\alpha_i;\ \ (i = 1, \dots, n-1) \\ a_{i,j} = 0;\ \ (otherwise) \end{gathered} \tag{55}$$

$$\begin{gathered} b_{i,i} = 3 \cdot (\alpha_i - \alpha_{i-1}) \cdot \ell;\ \ (i = 1, \dots, n) \\ b_{i,i+1} = -b_{i+1,i} = 3\alpha_i\ell;\ \ (i = 1, \dots, n-1) \\ b_{i,j} = 0;\ \ (otherwise) \end{gathered} \tag{56}$$

$$\begin{gathered} c_{i,i} = \alpha_i\ell^2 \cdot (2+\epsilon_i) + \alpha_{i-1}\ell^2 \cdot (2+\epsilon_{i-1});\ \ (i = 1, \dots, n) \\ c_{i,i+1} = c_{i+1,i} = \alpha_i\ell^2(1-\epsilon_i);\ \ (i = 1, \dots, n-1) \\ c_{i,j} = 0;\ \ (otherwise) \end{gathered} \tag{57}$$

The position of the elements of matrices *[A]*, *[B]*, and *[C]* is shown in Figure 18. Using the nomenclature defined in Figure 18, the stiffness of beam ‘i’ is represented by the diagonal terms of the matrices. The stiffness of beams ‘i-1’ and ‘i+1’ are represented by the terms to the left and right of the diagonal, respectively. Each of the matrices represent the stiffness of the beam to movement in a specific degree of freedom. The elements of matrix *[A]* represent the stiffness of the set of beams in heave due to a heave force, while the elements of matrix *[C]* represent the stiffness of the set of beams in pitch due to a pitch moment. The elements of matrix *[B]* represent the stiffness of the set of beams in heave due to a pitch moment, which is equivalent to the stiffness

in pitch due to a heave force. More details about the derivation of stiffness properties for a finite element lumped mass beam model can be found in Barltrop and Adams [49] and Bathe [40].

Figure 18 – Position of Beam Elements in Matrices [A], [B], and [C]

2.2.3 Hydrodynamic Forces Acting on the Ship

Strip theory is used to calculate the added mass of the water surrounding the ship. Strip theory allows for the calculation of the three-dimensional (3-D) added mass and damping coefficients of a hull form from two-dimensional (2-D) section coefficients by assuming that the hydrodynamic flow close to the ship is largely confined to planes perpendicular to the ship axis. For this approximation to be accurate, the vessel must be a slender body (beam and draft significantly smaller than length), changes in cross-section must occur gradually, the vessel must have no forward speed, and there can be no flow interaction between the 2-D sections. Given these assumptions, the solution of the flow around the 2-D sections can be related to the potential flow solution of the flow surrounding a 2-D circular cylinder of similar size to the ship section. The cylinder solution is transformed to the solution around the hull section utilizing conformal mapping, which is a method of translating the solution of one geometry to a new geometry and solution through a change of variables. The most common method of applying conformal mapping for ship hulls was developed by Lewis [50] using the transformation:

$$Z = z + \frac{a}{z} + \frac{b}{z^3} \tag{58}$$

where a and b are coefficients, Z is the ship coordinate, and z is the cylinder coordinate in the form:

$$z = x + iy \tag{59}$$

where x is the real component, y is the imaginary component, and i is the imaginary unit ($\sqrt{-1}$). After applying the transformation, it is determined that the added mass per unit length of the ship section, μ, is related to the added mass of a circular cylinder with a diameter equal to the ship section beam by:

$$\mu = C\left[\frac{1}{2}\pi\rho\left(\frac{B}{2}\right)^2\right] \tag{60}$$

where B is the ship beam, ρ is the density of the water, C is a hydrodynamic coefficient defined by the underwater shape of the cross-section.

The approximation of flow only contacting the ship in planes perpendicular to the ship axis is not valid at the ends of the vessel. To account for these 3-D flow effects, it was determined that the added mass distribution of the ship should be reduced by a 3-D correction factor, J, so that equation (60) becomes:

$$\mu = CJ\left[\frac{1}{2}\pi\rho\left(\frac{B}{2}\right)^2\right] \tag{61}$$

The magnitude of the correction factor was derived by analyzing the flow around a prolate spheroid vibrating in a mode shape similar to a ship vibration mode calculated by both strip theory and an exact solution. The factor J is the ratio of the kinetic energies of the exact solution to the strip theory approximate solution. The value of J selected for a ship comes from the analysis of a spheroid with a similar beam to length ratio. This method provides good results for the lower frequency vibration modes, but it has two primary disadvantages: that the calculation of J is dependent on the shape of the mode being calculated, so that a different equation has to be solved for each mode, and the reduction factor may vary along the length of the ship [20]. Several improvements have been made to strip theory to increase its accuracy for the stated disadvantages. However, the simplified version discussed above is sufficient for this analysis.

The hydrodynamic force acting on the ship-shaped cylinder can be calculated from the pressure exerted on the ship surface by the fluid. This pressure can be obtained using Bernoulli's equation:

$$p = p_0 + \rho\frac{\partial\Phi}{\partial t} - \frac{1}{2}\rho u^2 \tag{62}$$

where p_0 is the hydrostatic pressure, u is the local fluid velocity, and Φ is the velocity potential. For the problem of a ship floating on the surface subjected to hydrodynamic loading from a fluid with a velocity at infinity, U, the velocity potential can be written in the following form:

$$\Phi = \phi_U + \phi_D + \phi_R \tag{63}$$

where φ_U is the incident potential produced by the fluid velocity, φ_D is the diffraction potential induced by the hull girder free of any deformations, and φ_R is the radiation potential produced purely by the deflection of the hull girder [51]. Neglecting the ρu^2 term from equation (62), as it is small when compared to the $\rho\frac{\partial\phi}{\partial t}$ term, gives:

$$p = p_0 + \rho \frac{\partial \Phi}{\partial t} = p_0 + \rho \cdot \left(\frac{\partial \phi_U}{\partial t} + \frac{\partial \phi_D}{\partial t} + \frac{\partial \phi_R}{\partial t} \right) \tag{64}$$

Now, the hydrodynamic force per unit length acting on the hull surface, *f*, can be obtained by integrating equation (64):

$$f(x,t) = \oint_\Gamma pn_y dl = -\rho \oint_\Gamma \left(\frac{\partial \phi_U}{\partial t} + \frac{\partial \phi_D}{\partial t} + \frac{\partial \phi_R}{\partial t} \right) n_y dl \tag{65}$$

where $\oint_\Gamma ()\, n_y dl$ is the contour integral at the section defined by the curve *Γ*, and n_y is the vertical component of the unit normal of the body surface, as defined in Figure 19.

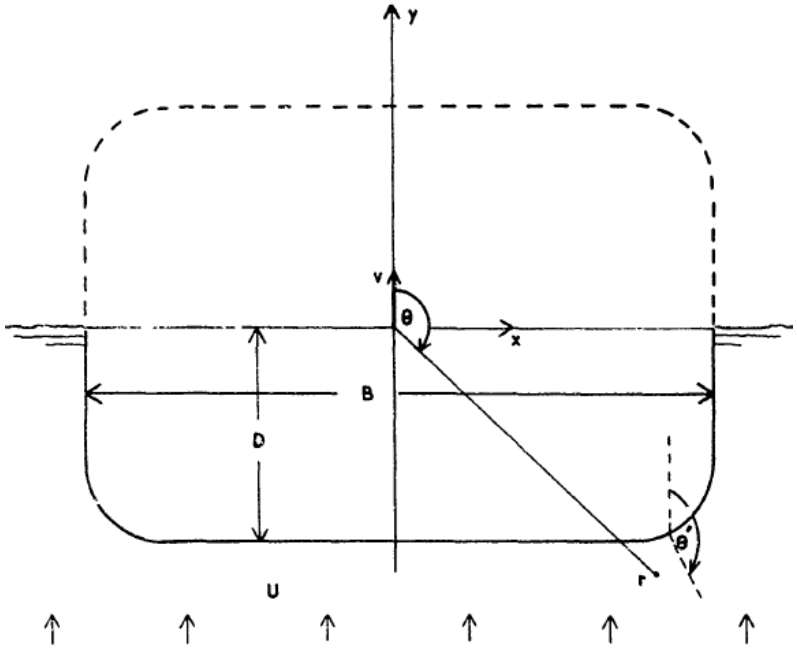

Figure 19 – Geometry for Accelerating Flow past a 2-D Ship Section [20]

For the first term of equation (63), the contour integral gives:

$$\oint_\Gamma \left(\rho \frac{\partial \phi_b}{\partial t} \right) n_y dl = \rho \dot{U} \oint_\Gamma ydz = \rho A \dot{U} \tag{66}$$

where *z* is an integration variable, *A* is the underwater area of the section, and $\dot{U}$ is the fluid acceleration at the section. For the diffraction potential satisfying:

$$\nabla^2 \phi_D = 0 \tag{67}$$

$$|\nabla \phi_D| \to 0 \; at \; infinity \tag{68}$$

$$\frac{\partial \phi_D}{\partial n} = -U \cdot \cos\theta \;\; on \; \Gamma \tag{69}$$

the second term of equation (63) can be written as:

$$\oint_{\Gamma} \left(-\rho \frac{\partial \phi_D}{\partial t}\right) n_y dl = \rho \dot{U} \oint_{\Gamma} \left(\phi_D \frac{\partial \phi_D}{\partial n}\right) dl = \mu \dot{U} \tag{70}$$

where μ is the added mass per unit length of the section defined by equation (61). Equation (67) indicates that the potential must satisfy Laplace's equation, meaning that the flow must be incompressible. Equation (68) requires that the divergence of the potential approach zero at infinity. Equation (69) is the no penetration boundary condition, meaning that the flow cannot pass through the surface of the ship.

Lastly, for the radiation potential satisfying the necessary conditions:

$$\nabla^2 \phi_R = 0 \tag{71}$$

$$|\nabla \phi_R| \to 0 \; at \; infinity \tag{72}$$

$$\frac{\partial \phi_R}{\partial n} = v \cdot \cos\theta \;\; on \; \Gamma \tag{73}$$

where v is the upward velocity of the section, the third term of equation (63) can be written as:

$$\oint_{\Gamma} \left(-\rho \frac{\partial \phi_R}{\partial t}\right) n_y dl = \rho \dot{v} \oint_{\Gamma} \left(\phi_R \frac{\partial \phi_R}{\partial n}\right) dl = \mu \dot{v} \tag{74}$$

where $\dot{v}$ is the upward acceleration of the section.

Substituting the results from equations (66), (70), and (74) into equation (65) gives the hydrodynamic force per unit length acting on each section [51, 20], $f_{hd,cs}$:

$$f_{hd,cs} = \rho A \dot{U} - \mu \ddot{y} + \mu \dot{U} = \rho A \dot{U} + \mu\left(\dot{U} - \dot{v}\right) \tag{75}$$

This equation gives the expected result that the ship will see two distinct flows, one from its motion and one from the motion of the surrounding fluid. The first term is the buoyancy force due to the pressure gradient required in the water to give it the acceleration $\dot{U}$, while the second term is the inertial force due to the relative acceleration of the ship-shaped cylinder and the fluid. Under static gravity, meaning $\dot{U}$ is the acceleration due to gravity, the first term becomes the weight of the water displaced by the section, which is equivalent to the buoyancy per unit length of the section. The variable $\bar{\mu}$ is used to represent ρA in subsequent equations to simplify the notation of the terms.

This result can be applied in a method consistent with that of strip theory. The vertical motion of the water due to the motion of the UNDEX bubble can be calculated as though the ship is not present at each point along the ship axis, which is defined as the intersection of its centerline with the waterline plane. The hydrodynamic force acting on the section due to the bubble motion

can be determined from equation (75) by setting $\dot{U}$ equal to the fluid acceleration produced by the bubble motion, equation (38), at these locations. It can also be assumed that the charge is far enough away from the ship so that this velocity distribution will only vary slowly along the length of the ship. By making this assumption, the disturbance potential necessary to correct the local flow for the presence of the ship is approximately equal to the sum of the diffraction and radiation potentials, so that the force on the ship can be given by equation (75).

2.2.4 Ship Vibration Equation of Motion

It is assumed that the only external forces acting on the ship are from the fluid accelerations produced by the bubble pulses, which act in addition to the inertial forces due to the ship's mass in affecting the ship motions. Each of these forces form a continuous distribution of force along the ship, but are assumed to be applied as a series of summed forces at the lumped mass locations. It is also assumed that any moments produced by these forces are negligible, so that rotation terms can be ignored. If the variation in cross-sectional shape is small between lumped masses, the lumped force in the vertical direction at the ith lumped mass, F_i, is:

$$F_i = F_{hd,i} + F_{hs,i} + F_{I,i} \tag{76}$$

where $F_{hd,i}$, $F_{hs,i}$, and $F_{I,i}$ are the lumped hydrodynamic, hydrostatic, and inertial forces at the ith lumped mass in the vertical direction, respectively. The lumped hydrodynamic force, defined by equation (75), is calculated as:

$$F_{hd,i} = [\mu_i(\dot{u}_i - \ddot{y}_i) + \bar{\mu}_i \dot{u}_i]\ell \tag{77}$$

where μ_i is the added mass per unit length at the ith lumped mass, $\dot{u}_i$ is the vertical fluid acceleration evaluated at the free surface at the longitudinal position of the ith lumped mass, $\ddot{y}_i$ is the vertical deflection acceleration of the ith lumped mass, $\bar{\mu}_i$ is the mass of displaced water per unit length at the ith lumped mass, and ℓ is the length of a weightless beam connecting two lumped masses. The hydrostatic force, which is equal to the loss of buoyancy due to upward deflection, is calculated as:

$$F_{hs,i} = -B_i \ell y_i \tag{78}$$

where B_i is the buoyancy force per unit submergence per unit length along the ship at the ith lumped mass and y_i is the vertical deflection of the ith lumped mass. The normal inertial force is calculated as:

$$F_{I,i} = -m_i \ddot{y}_i \tag{79}$$

where m_i is the mass of the ith lumped mass. Substituting equations (77) through (79) into equation (76) and simplifying terms multiplied by ℓ gives:

$$F_i = -\left(m_i + m_{w,i}\right)\ddot{y}_i - k_i y_i + (m_{wi} + \bar{m}_{w,i})\dot{u}_i \tag{80}$$

where $m_{w,i}$, k_i, and $\bar{m}_{w,i}$ are the lumped added mass, buoyancy per unit submergence, and lumped mass of water displaced at the ith lumped mass, respectively. The lumped added mass and mass of water displaced terms are defined as:

$$m_{w,i} = \mu_i \ell \tag{81}$$

$$\bar{m}_{w,i} = \bar{\mu}_i \ell \tag{82}$$

The lumped mass of water displaced is equivalent to the buoyancy of the ith lumped mass.

In matrix form, equation (80) becomes:

$$\vec{F} = -([M] + [M_w])\ddot{\vec{y}} - [K]\vec{y} + ([M_w] + [\bar{M}_w])\dot{\vec{u}} \tag{83}$$

where all matrices are diagonal (n x n) matrices with elements consistent with:

$$M_{i,i} = m_i \tag{84}$$

and all vectors are of length 'n' with elements defined by their associated ith lumped mass terms. The forces, $\vec{F}$, in equation (83) are the forces necessary to maintain the deflected shape, $\vec{y}$, from equation (53). Therefore, the equation of forced motion of the ship in the vertical plane is:

$$\left[[A] - [B][C]^{-1}[B]^T\right]\vec{y} = -([M] + [M_w])\ddot{\vec{y}} - [K]\vec{y} + ([M_w] + [\bar{M}_w])\dot{\vec{u}} \tag{85}$$

which, when simplified and solved for the fluid acceleration term gives:

$$[M_1]\ddot{\vec{y}} + [S]\vec{y} = [M_2]\dot{\vec{u}} \tag{86}$$

where *[S]* is the stiffness matrix of the hull defined in equation (53) and $[M_1]$ and $[M_2]$ are diagonal (n x n) mass matrices defined as:

$$[M_1] = [M] + [M_w] \tag{87}$$

$$[M_2] = [M_w] + [\bar{M}_w] \tag{88}$$

The mass matrices in equation (86) are assumed to remain constant throughout the analysis, regardless of any change in draft or trim. It is also assumed that these masses are the same for all vibration modes, as the negative effects on accuracy are minimal [20]. Equation (86) fully defines the dynamic response of the hull girder as an elastic system acted on by forces due to the pulsating bubble model [23].

2.2.5 Ship Normal Mode Equations

To simplify the integration of the ship vertical vibration EOM, equation (86), it is decomposed into its normal modes. This separating of the EOM allows for the deletion of higher frequency modes, which do not significantly contribute to the solution, to avoid any unnecessary calculations and to streamline results [20]. To perform this separation, the ship deflection vector, $\vec{y}$, is first transformed using the mass plus added mass matrix, *[M₁]* defined by equation (87):

$$\vec{z} = [M_1]^{1/2}\vec{y} \tag{89}$$

where $\vec{z}$ is the transformed deflection vector and $[M_1]^{1/2}$ is a diagonal matrix with elements equal to the square root of the elements of *[M₁]*. Solving equation (89) for $\vec{y}$ gives:

$$\vec{y} = [M_1]^{-1/2}\vec{z} \tag{90}$$

Substituting equation (90) into equation (86) gives:

$$[M_1]^{1/2}\ddot{\vec{z}} + [S][M_1]^{-1/2}\vec{z} = [M_2]\vec{\ddot{u}} \tag{91}$$

where *[S]* is the stiffness matrix defined by equation (53), *[M₂]* is the hydrodynamic mass matrix defined by (88), and $\vec{\ddot{u}}$ is the vector containing the distribution of vertical fluid accelerations due to the pulsating bubble along the ship, calculated using equation (38) at the lumped mass locations. Simplifying equation (91) by multiplying it by $[M_1]^{-1/2}$ gives the EOM in terms of the transformed deflection vector:

$$\ddot{\vec{z}} + [E]\vec{z} = [M_1]^{-1/2}[M_2]\vec{\ddot{u}} \tag{92}$$

where *[E]* is the transformed stiffness matrix equivalent to:

$$[E] = [M_1]^{-1/2}[S][M_1]^{-1/2} \tag{93}$$

The transformed stiffness matrix is symmetric and positive definite, just as the original stiffness matrix is, meaning it has real and positive eigenvalues that are equal to the squares of the natural frequencies of the system, ω_i^2. Due to these characteristics, the normalized eigenvectors of *[E]* will form an orthogonal set, meaning the following properties are true:

$$\vec{z}_i^T\vec{z}_j = \delta_{ij};\ \ (i \neq j) \tag{94}$$

$$[E]\vec{z}_i = \omega_i^2\vec{z}_i \tag{95}$$

where $\vec{z}_i$ is the eigenvector associated with the i[th] normal mode shape, $\vec{z}_j$ is an arbitrary vector of length 'n,' and δ_{ij} is a positive non-zero scalar. The eigenvectors also form a complete set, so that the vector $\vec{z}$ and the right hand side of equation (92) can be expressed in the form:

$$\vec{z} = \sum_{i=1}^{n} \alpha_i(t)\vec{z}_i \tag{96}$$

$$[M_1]^{-1/2}[M_2]\vec{\ddot{u}} = \sum_{i=1}^{n} \beta_i(t)\vec{z}_i \tag{97}$$

where $\alpha_i(t)$ is the modal coefficient and $\beta_i(t)$ is the forcing function for the i[th] normal mode shape. Substituting equations (95) through (97) into equation (92), and taking advantage of the orthogonality of the eigenvectors, gives:

$$\ddot{\alpha}_i(t)\vec{z}_i + \omega_i^2\alpha_i(t)\vec{z}_i = \beta_i(t)\vec{z}_i \tag{98}$$

Eliminating $\vec{z}_i$ from equation (98) gives the decoupled form of equation (86):

$$\ddot{\alpha}_i(t) + \omega_i^2\alpha_i(t) = \beta_i(t) \tag{99}$$

Equation (99) is a set of 'n' independent equations, each representing a different normal mode shape.

The i[th] ship deflection mode shape, $\vec{y}_i$, is determined from the i[th] normal mode shape using the relationship in equation (90):

$$\vec{y}_i = [M_1]^{-1/2}\vec{z}_i \tag{100}$$

The orthogonality relationship, equation (94), in terms of the i[th] deflection mode shape is:

$$\vec{y}_i^T[M_1]\vec{y}_j = \delta_{ij} \tag{101}$$

where $\vec{y}_j$ is a vector transformed from $\vec{z}_j$ consistent with the relationship in equation (90). Utilizing matrix relationships, equation (101) can be simplified to the form:

$$\sum_{k=1}^{N} m_{1,k}y_{ki}y_{kj} = \delta_{ij} \tag{102}$$

where $m_{1,k}$ is the k[th] diagonal element in $[M_1]$ and y_{ki} and y_{kj} are the k[th] elements of $\vec{y}_i$ and $\vec{y}_j$, respectively.

Multiplying the i[th] independent equation of equation (97) by $\vec{z}_j^T$ gives:

$$\vec{z}_j^T\beta_i(t)\vec{z}_i = \vec{z}_j^T[M_1]^{-1/2}[M_2]\vec{\ddot{u}} \tag{103}$$

Simplifying by using the orthogonality relationship, equation (94), and substituting equation (90) into equation (103) gives:

$$\delta_{ij}\beta_j(t) = y_j^T[M_2]\vec{\ddot{u}} \tag{104}$$

Due to the orthogonality of the mode shapes, setting $\vec{y}_j$ equal to $\vec{y}_i$ causes δ_{ij} to be equal to one. Now, after simplifying the matrix relationships similar to equation (102) and setting $\vec{y}_j$ equal to $\vec{y}_i$, the forcing function in equation (104) can be represented as:

$$\beta_i(t) = y_i^T[M_2]\vec{\ddot{u}} = \sum_{k=1}^{n} m_{2,k} y_{ki} \dot{u}_k(t) \tag{105}$$

where $m_{2,k}$ is the hydrodynamic mass associated with the k[th] lumped mass and $\dot{u}_k(t)$ is the time-dependent vector of fluid acceleration values at the k[th] lumped mass. Substituting equation (105) into equation (99) gives the equation for the i[th] modal coefficient:

$$\ddot{\alpha}_i(t) + \omega_i^2 \alpha_i(t) = \sum_{k=1}^{n} m_{2,k} y_{ki} \dot{u}_k(t) \tag{106}$$

where ω_i is the natural vertical vibration frequency for the i[th] deflection mode shape of the hull girder calculated from the eigenvalues of *[E]*. Equation (106) can then be integrated separately for each mode shape to solve for the modal coefficients in each vibration mode shape with the initial conditions:

$$\begin{aligned} \alpha_i(0) &= 0 \\ \dot{\alpha}_i(0) &= 0 \end{aligned} \tag{107}$$

As discussed previously, it is only necessary to integrate equation (106) for the first few low frequency modes because the higher frequency modes do not contribute much to the motion of the hull girder for this type of problem. This is primarily due to the frequencies of the higher mode shapes being significantly higher than the frequency of pulsating UNDEX bubbles that are produced by large charges near the ship, severely limiting the potential for resonant vibration in these modes. Also, the ship is capable of greater deflections in its lower frequency mode shapes due to the greater distance between the zero deflection nodes of the low frequency modes compared to the higher frequency modes. It is also necessary to limit the analysis to the low frequency modes due to the limitations of beam theory [20].

The vibration frequency for the i[th] mode shape, f_i, can be obtained by:

$$f_i = \omega_i / 2\pi \tag{108}$$

The rotational mode shapes of the hull girder, $\vec{\gamma}$, can be calculated from the normal mode shapes from the relationship in equation (54).

2.2.6 Ship Total Motion Equations

The deflection, deflection velocity, bending moment, deck stress, and shear force can be obtained at any time and location along the ship by combining the modal coefficients with the

positional mode coefficients for each mode shape and superimposing all of the significant mode shapes onto the hull girder.

Deflection $$y(x,t) = \sum_{i=1}^{N} \alpha_i(t) y_i(x) \tag{109}$$

Deflection Velocity $$\dot{y}(x,t) = \sum_{i=1}^{N} \dot{\alpha}_i(t) y_i(x) \tag{110}$$

Bending Moment $$BM(x,t) = \sum_{i=1}^{N} \alpha_i(t) BM_i(x) \tag{111}$$

Deck Stress $$\sigma(x,t) = \frac{\bar{y}(x)}{I(x)} BM(x,t) \tag{112}$$

Shear Force $$V(x,t) = \sum_{i=1}^{N} \alpha_i(t) V_i(x) \tag{113}$$

In equations (109) through (113), $\bar{y}(x)$ is the distance of the deck above the neutral axis and *I(x)* is the moment of inertia of the cross-section at a location *x* along the ship. *N* is the total number of mode shapes included in the integration, including heave and pitch. The default value for *N* is six, but a different number can be chosen by the user. Six is chosen as the default for *N* because only the first five or six mode shapes need to be included to represent experimental results accurately and the higher frequency modes do not contribute much to the solution [23]. The positional mode coefficients, $y_i(x)$, $BM_i(x)$, and, $F_i(x)$, are the unit amplitude deflection, bending moment, and shear force at the position *x* when the ship is in the ith mode. Their equations are derived from the beam equations, equation (48), and are:

$$\begin{bmatrix} y_i(x) \\ BM_i(x) \\ F_i(x) \end{bmatrix} = \begin{bmatrix} 1 & \bar{x} & \frac{\bar{x}^2}{2EI_k} & -\frac{\bar{x}^3(1-\epsilon_k)}{6EI_k} \\ 0 & 0 & 1 & -\bar{x} \\ 0 & 0 & 0 & 1 \end{bmatrix} \begin{bmatrix} y_{ki} \\ \gamma_{ki} \\ BM_L \\ F_L \end{bmatrix} \tag{114}$$

where $\bar{x}$ is the distance from the left hand end of the current beam section to the location of interest along the beam, BM_L is the moment applied to the left end of the beam section, F_L is the shear force applied to the left end of beam section, a subscript *i* indicates that the value for the ith mode should be used, and a subscript *k* indicates that the value at the kth lumped mass should be used. The value of $\bar{x}$ cannot be less than zero or greater than ℓ and the default value is half of ℓ. BM_L and F_L are calculated by equation (49).

2.3 Modifications to Hicks Model

The model described in the previous section calculates the whipping response of a ship to a single bubble pulse. The methods presented in this section were developed to expand the capability of the model to include the effects of multiple bubble pulses and to improve the overall accuracy of the model without making it significantly more complex.

2.3.1 Removal of Energy at Bubble Minimums

As discussed in section 1.2.2, the energy contained within an UNDEX bubble decreases with each oscillation. This results in smaller maximum radii and weaker bubble pulses for the second and later oscillations compared to the first oscillation. The bubble model described in section 2.2.1 does not account for this loss of energy, which results in the characteristics of the second and later oscillations being nearly identical to those of the first oscillation. Sample radius-time and fluid acceleration-time history plots with no energy removal between minimums are shown in Figure 20 and Figure 21, respectively. These inaccuracies can be eliminated by incorporating an energy loss mechanism into the bubble model. The methodology presented in this section applies an empirical loss of energy to the bubble system at the minimums designed to tune the model to closely match the results for second and later pulses given by the similitude equations in section 1.2.3.1.

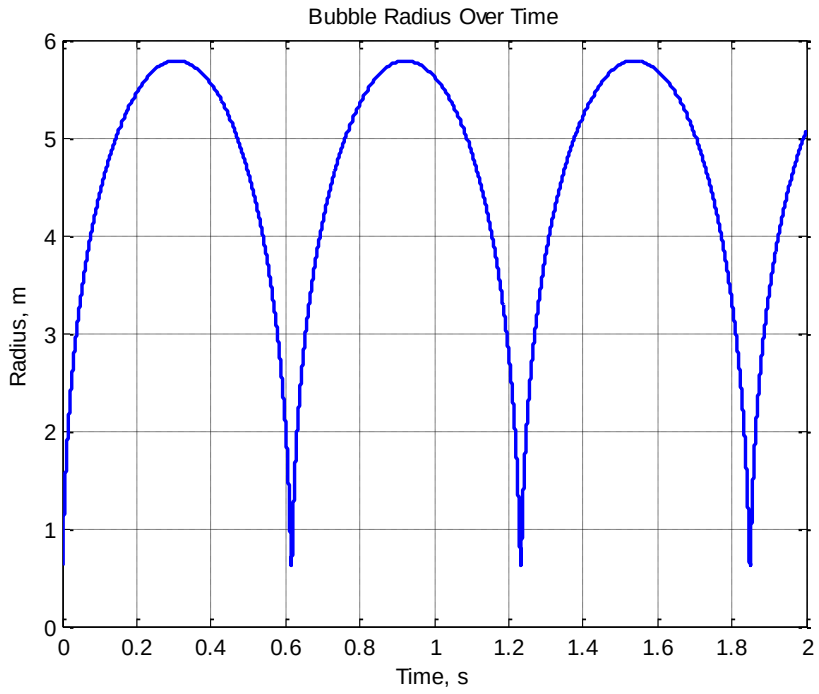

Figure 20 – Sample Bubble Radius-Time History, No Energy Removal

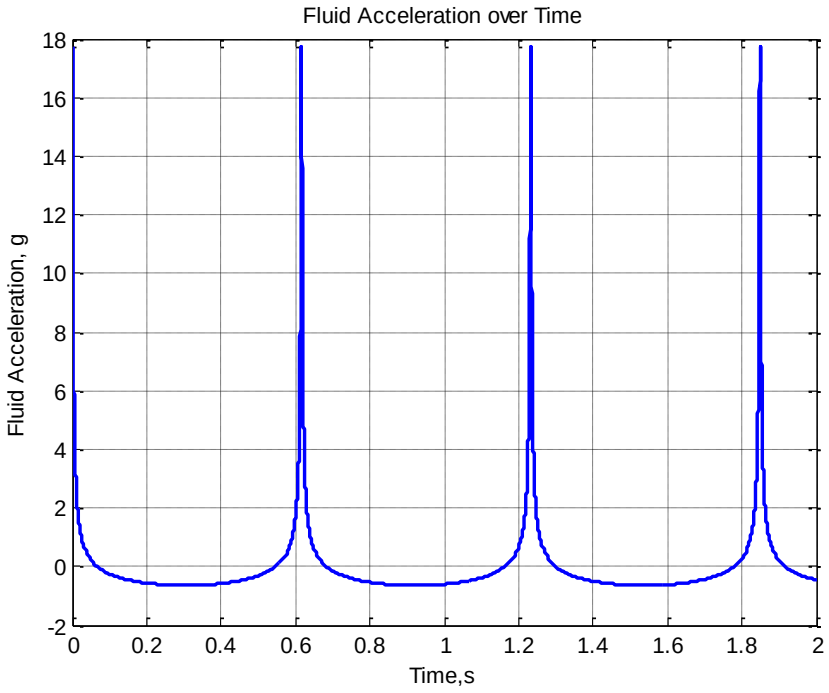

Figure 21 – Sample Bubble Fluid Acceleration-Time History at Free Surface, No Energy Removal

Energy is lost from the bubble system throughout its oscillation, with the majority of energy lost due to phenomena that occur at the minimums, as discussed in section 1.2.2. These mechanisms are not captured in the simplified bubble model, so an empirical loss of energy correction is applied at each minimum to simulate the effects of energy dissipation on the dynamics of the bubble. In saying this, it is assumed that all of the energy loss occurs at the minimums. This is a common assumption made in the derivation of the similitude equations and similar bubble models [14, 21]. However, there is not a universally agreed-upon simple method of calculating and applying energy dissipation in this manner.

The method developed and used to apply energy dissipation at the bubble minimum is outlined by the flowchart in Figure 22. This method treats the secondary bubble pulses as lower energy versions of the original explosion that occur immediately after the bubble radius reaches its minimum value, with initial conditions identical to those present at the same minimum. All step numbers referenced correspond to those given in Figure 22.

After carrying out the initial, full energy integration of the bubble EOMs, the first step of the energy dissipation process is to locate the bubble minimum radius in the bubble radius output and record the time. To ensure the first minimum is selected, the bubble radius vector is only searched in locations that correspond to the predicted time of first bubble minimum calculated by similitude, equation (2). If the inputted total simulation time does not allow for a bubble minimum to occur, characteristics for later pulses are not calculated because none will occur (step 2). The hydrostatic pressure head, bubble radius, and migration speed, are recorded at the minimum (step 3) and re-dimensionalized using the length and time scales (step 4), equations (26) and (27):

$$\begin{aligned} a_{min1} &= x_{min1}L \\ Z_{min1} &= Z_{0,2} = \zeta_{min1}L \\ v_{min1} &= \dot{\zeta}_{min1}L/T \end{aligned} \tag{115}$$

where subscript *min1* indicates a value at the first minimum and subscript *0,2* indicates an initial value for the second pulse. These two designations are interchangeable for dimensional terms, but not for non-dimensional terms. This is due to the variation of the length and time scales between pulses, which is caused by the change in bubble energy and initial conditions between the first and second pulse.

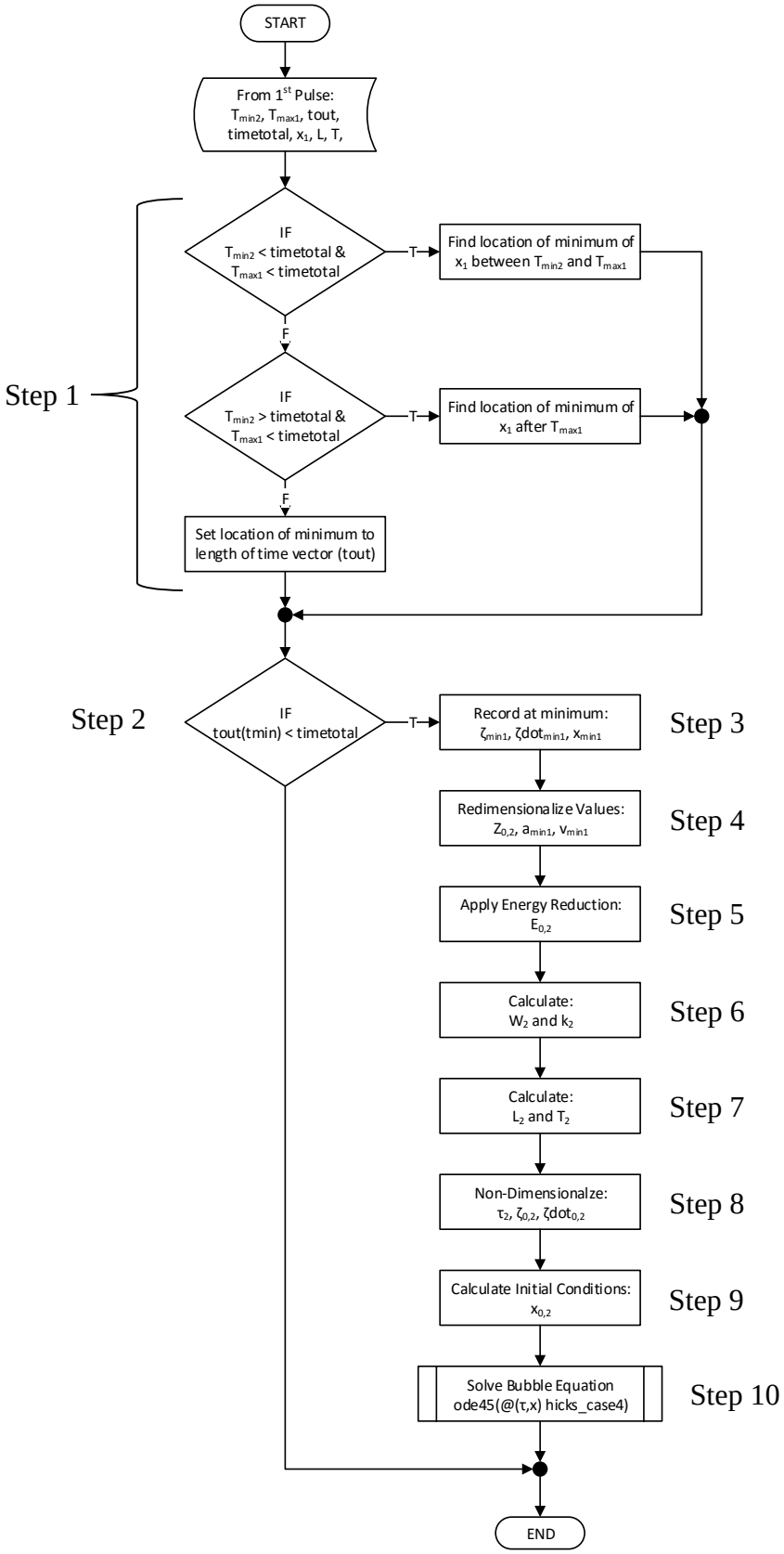

Figure 22 – Bubble Energy Dissipation Flow Chart

Next, the initial energy for the explosion, as calculated in equation (23), is multiplied by a factor representing the percentage of energy to be retained for the next pulse, E_{ret1} (step 5). This factor is used to calculate the energy remaining in the bubble at the start of the second pulse, $E_{0,2}$:

$$E_{0,2} = E_0 E_{ret1} \tag{116}$$

Using this value and the characteristics defined in equation (115), a reduced-effective value for charge weight, W_2, is calculated (step 6). This is done by rearranging the conservation of energy equation used to derive the bubble EOM, equation (23), to solve for charge weight:

$$W_2 = \left[\frac{(\gamma-1)a_{min1}^{3(\gamma-1)}}{k_1}\left(\frac{4\pi}{3}\right)^{\gamma-1}\left(E_{0,2} - \pi\rho a_{min1}^3\left(\frac{4}{3}gZ_{0,2} + \frac{v_{min1}^2}{3}\right)\right)\right]^{\frac{1}{\gamma}} \tag{117}$$

where all terms are as they are previously defined. All terms containing $\dot{a}$ are assumed to be zero and not included in the equation due to the calculation occurring at a minimum of the bubble radius, a. This is consistent with the calculus definition that a derivative of a function will equal zero when the function is at a local minimum or maximum value. The value for W_2 is then entered into equation (30), along with $E_{0,2}$ and $Z_{0,2}$, to calculate the value for k_2 (step 6), the adiabatic pressure-volume relationship constant for the second pulse.

Next, the length and time scales for the second pulse, L_2 and T_2, are calculated using equations (26) and (27) and all necessary values at the bubble minimum defined in this section (step 7). To convert the initial conditions and time vector to a form consistent with the non-dimensional EOMs, they are non-dimensionalized using the updated scale factors (step 8):

$$\tau_2 = {}^{t}/_{T_2} \tag{118}$$

where the time vector, t, begins at the time of the bubble minimum. Lastly, the system in equation (35) is integrated using the following initial conditions (steps 8-10):

$$\begin{gathered} x_{0,2} = k_2^{\frac{1}{3(\gamma-1)}}\left(1 + \frac{k_2^{\frac{1}{\gamma-1}}}{3(\gamma-1)}\right) \\ \dot{x}_{0,2} = \sigma_{0,2} = 0 \\ \zeta_{0,2} = {}^{Z_{0,2}}/_{L_2} \\ \dot{\zeta}_{0,2} = \lambda_{0,2} = v_{min1}\,{}^{T_2}/_{L_2} \end{gathered} \tag{119}$$

This method is also applied at the end of the second pulse to produce results for a third pulse. The model is stopped after the third pulse due to the instability of the equations in later pulses, relative insignificance of later pressure pulses, and many of the assumptions no longer being valid.

2.3.1.1 Bubble Tuning

As discussed in section 1.2.2, there is some consensus among researchers regarding the percentage of energy lost between the minimums of an UNDEX bubble cycle. In general, sixty to seventy percent is lost during the first oscillation, and fifty to sixty percent of the remaining energy is lost during the second and later oscillations [12, 18, 20, 21, 22]. These values are used as a guideline in selecting the empirical amount of energy loss applied to the model at each bubble minimum.

To determine the values of energy loss that produce a bubble radius-time history that best represents the behavior of an UNDEX bubble, a case study was completed. This study tuned the values of E_{ret1} and E_{ret2} so that the bubble radius-time histories produced by the bubble model most closely matched those calculated by the similitude equations in section 1.2.3. The case study was performed for a series of charge weight and depth combinations that covered many possible UNDEX threats. For each combination of charge weight and depth, bubble radius time histories were adjusted using two criteria: match periods and match maximum radii. The goal of using the two criteria was to determine the values of E_{ret1} and E_{ret2} that minimized the percent error between the relevant values calculated by the model and those calculated by the related similitude equations. The overall goal of the study is to determine the values of E_{ret1} and E_{ret2} that minimized the sum of the radius and period percent errors over a range of charge weight and depth combinations. The percent errors were calculated as:

$$\%\ Error\ A_{max} = \frac{A_{max,M} - A_{max,S}}{A_{max,S}} \cdot 100\% \tag{120}$$

$$\%\ Error\ T = \frac{T_M - T_S}{T_S} \cdot 100\% \tag{121}$$

where A_{max} is the maximum bubble radius for a given pulse, T is the period of the pulse, a subscript M represents a value calculated by the model, and a subscript S represents a value calculated by a similitude equation. The combinations of charge weights and depths used for the study are listed

in Table 6. The values of E_{ret1} and E_{ret2} were varied by increments of 0.01 to identify the value that produced the lowest percent error for each criteria throughout the study.

Table 6 – List of Bubble Tuning Study Charge Weight and Depth Combinations

	Charge Weight (kg)				
	50 kg	100 kg	250 kg	500 kg	1000 kg
Charge Depths (m)	20 m	20 m	20 m	30 m	30 m
	30 m	30 m	30 m	40 m	40 m
	40 m	40 m	40 m	50 m	50 m
	50 m	50 m	50 m	60 m	60 m
			60 m		

The study was completed for two bubble motion cases: non-migrating and migrating near a free surface with the pseudo drag coefficient. The non-migrating case was done first because the similitude equations were derived using data from deep, non-migrating bubbles. The results for this case are summarized in Table 7 through Table 9. The results for both pulses were very consistent, with the largest standard deviation (std dev) being equivalent to less than a one percent difference in the amount of energy retained. The consistency of the data shows that a single value of E_{ret1} and E_{ret2} can be chosen to provide accurate bubble behaviors regardless of charge weight or depth. Also, the average values of E_{ret1} and E_{ret2} for each scenario fall either within or slightly outside of the ranges of the experimentally observed percentage of energy lost at the bubble minimums, which helps to confirm the validity of the method of energy dissipation.

Table 7 – Non-migrating Case, Results

	Period E_{ret1}	**Period E_{ret2}**	**Radius E_{ret1}**	**Radius E_{ret2}**
Average	0.4005	0.6090	0.3752	0.5048
Std Dev	0.0021	0.0029	0.0091	0.0050
% Error A_{max}	2.87%	10.46%	0.44%	0.45%
% Error T	-0.45%	-0.13%	-2.56%	8.04%

Table 8 – Non-migrating Case, Results by Charge Weight

Charge Weight (kg)	E_{ret1} Average	E_{ret1} Std Dev	E_{ret2} Average	E_{ret2} Std Dev
50	0.3850	0.0169	0.5575	0.0563
100	0.3850	0.0169	0.5575	0.0563
250	0.3880	0.0148	0.5570	0.0560
500	0.3900	0.0120	0.5563	0.0550
1000	0.3913	0.0136	0.5563	0.0550

Table 9 – Non-migrating Case, Results by Depth

Charge Depth (m)	E_{ret1} Average	E_{ret1} Std Dev	E_{ret2} Average	E_{ret2} Std Dev
20	0.3800	0.0219	0.5550	0.0602
30	0.3850	0.0158	0.5550	0.0580
40	0.3880	0.0132	0.5570	0.0560
50	0.3900	0.0105	0.5600	0.0527
60	0.3967	0.0082	0.5567	0.0513

The results for the migrating bubble case are summarized in Table 10 through Table 12. The similitude equations used as the comparison accounted for both the vertical displacement of the bubble and the presence of the free surface, as shown in equation (5). The results for both pulses were very consistent, with the second maximum radius having a standard deviation greater than one percent. These results are very similar to those of the non-migrating case, with the largest differences being the need for slightly more energy to be retained in the migrating case for the radii matching scenario. Also, less energy is required for the period matching scenario for the migrating case.

Table 10 – Bubble Model Tuning Migrating Case, Results

	Period E_{ret1}	**Period E_{ret2}**	**Radius E_{ret1}**	**Radius E_{ret2}**
Average	0.3824	0.6067	0.3819	0.5290
Std Dev	0.0097	0.0139	0.0073	0.0092
% Error A_{max}	0.23%	5.60%	0.19%	0.21%
% Error T	-0.18%	-0.12%	-0.22%	-4.33%

Table 11 – Bubble Model Tuning Migrating Case, Results by Charge Weight

Charge Weight (kg)	**E_{ret1} Average**	**E_{ret1} Std Dev**	**E_{ret2} Average**	**E_{ret2} Std Dev**
50	0.3825	0.0089	0.5625	0.0459
100	0.3825	0.0071	0.5650	0.0434
250	0.3830	0.0067	0.5710	0.0477
500	0.3838	0.0074	0.5663	0.0366
1000	0.3788	0.0136	0.5738	0.0389

Table 12 – Bubble Model Tuning Migrating Case, Results by Depth

Charge Depth (m)	**E_{ret1} Average**	**E_{ret1} Std Dev**	**E_{ret2} Average**	**E_{ret2} Std Dev**
20	0.3767	0.0082	0.5783	0.0488
30	0.3770	0.0116	0.5680	0.0426
40	0.3830	0.0067	0.5640	0.0412
50	0.3860	0.0052	0.5660	0.0427
60	0.3883	0.0041	0.5667	0.0408

As a result of this study, values for E_{ret1} and E_{ret2} were chosen to be 0.38 and 0.56, respectively. These values cause the bubble model to produce results for bubble characteristics which are most consistent with calculated values from the similitude equations, with percent errors no greater than two or three percent for most migrating explosion scenarios and no greater than

five or six percent for most non-migrating explosion scenarios. These values are also consistent with experimentally observed values of energy dissipation at bubble minimums.

2.3.2 Exclusion of Heave and Pitch Modes

The motions that result from the heave and pitch modes of the ship as calculated by the model are not considered for the whipping analyses. These rigid body modes, by definition, do not cause the ship structure to bend, and bending is the main cause of hull failure being evaluated. Therefore, not including these mode shapes will not affect the whipping results.

2.3.3 Addition of Time without Forcing

To allow for the ship to experience the full effects of the last bubble pulse, an additional amount of time is added to the simulation where there are no fluid accelerations or forcing acting on the ship. This method prevents the possibility of potential maximum deflections or bending moments being ignored if they result from the momentum produced by the last simulated bubble pulse. Choosing not to simulate more than three bubble pulses is necessary because the bubble assumptions and equations break down significantly during later pulses, meaning the accuracy of the calculated pressure pulses is suspect. This is especially true after the third pulse. Also, the pressure pulses emitted after the fourth and later bubble cycles are small compared to the first and second pulses.

2.4 Model Assessment

A series of comparisons were made between model-produced results and results given by empirical methods and previous analyses to determine the accuracy of the bubble and whipping model. Throughout this section and the remainder of this thesis, the model described in this chapter is referred to as the "VT model."

2.4.1 Bubble Model

The accuracy of the VT bubble model was assessed using two methods: comparing model results to similitude equations and to the sample results provided in referenced works [20, 21]. The

similitude equations are considered to be the correct and desired result, specifically if the two methods disagree, as they were derived from a large body of experimental data. The sample results are used to confirm the VT model behavior between the points highlighted by the similitude equations, which is important in assessing migration results and the results from charges close to the surface. The scenarios outlined in Table 13 are investigated with the goal of evaluating the performance of the VT model for bubble radius, migration, or fluid acceleration against other prediction models and methods. Scenarios 1, 2, and 6 were chosen based on similar cases found in existing literature.

Table 13 – Bubble Model Assessment Scenarios

Scenario	Source	Charge Weight	Charge Depth	Compared
1	[21]	45.5 kg	7.6 m	Radius, Migration
2	[21]	227 kg	45 m	Radius, Migration
3	N/A	544 kg	30 m	Radius
4	N/A	260 kg	20 m	Radius
5	N/A	1500 kg	60 m	Radius
6	[20]	500 lb	50 ft	Fluid Acceleration

The bubble radius and depth time histories for two explosion scenarios produced by the VT model were compared with those given by Vernon [21]. Vernon utilizes the same potential flow-based method as the VT model to develop his bubble model. Scenario 1 is a 45.5 kg charge of TNT at a depth of 7.6 meters. Bubble migration, the free surface effect, and the pseudo drag coefficient are included. Figure 23 shows the bubble radius time histories for both the VT model simulation (blue line) and Vernon's simulation (green line with circles), which is from the migrating near a free surface results (solid line) in Figure 24. The differences between the maximum radius and period calculated by the two methods is negligible. The time histories for both simulations have a maximum bubble radius of slightly approximately 4.8 meters that occurs approximately 0.3 seconds after detonation and a bubble period of 0.62 seconds.

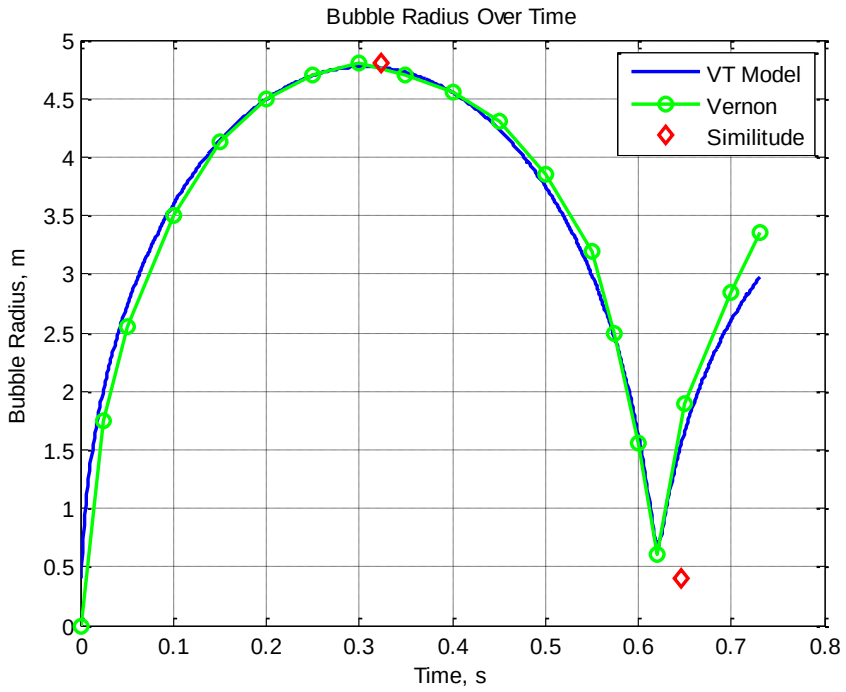

Figure 23 – Bubble Radius Time Histories, Scenario 1, from VT Model (blue) and Vernon [21] (green)

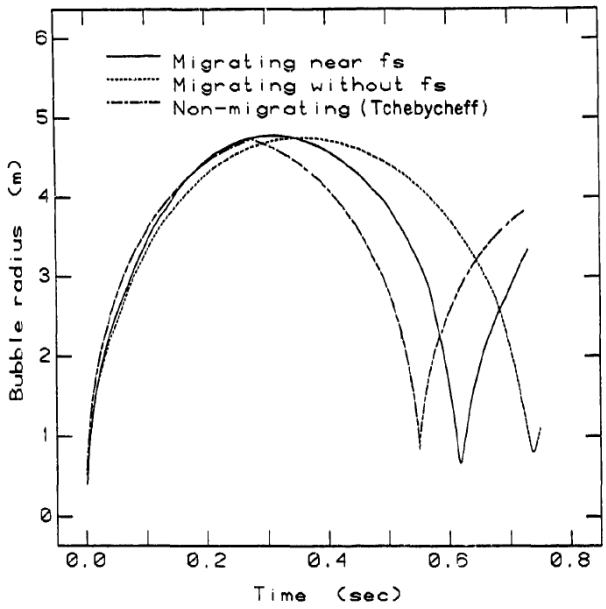

Figure 24 – Bubble Radius Time History, Scenario 1, from Vernon [21]

The red diamonds on the bubble radius time history plot represent the values of both the maximum and minimum bubble radius and the time at which they occur, as calculated by the similitude equations in section 1.2.3.1. For charges near the surface, the VT model results are

slightly different than the similitude results. This is primarily due to the free surface correction factor applied to the similitude equation being treated as a constant one for this analysis, though it tends to vary slightly with the ratio of maximum radius to depth. For charge 1, the value of maximum radius is a close match, but it occurs earlier than predicted by similitude. The minimum radius also occurs earlier than predicted by similitude.

The bubble depth time histories for scenario 1 are shown in Figure 25. The blue line represents the VT model results and the green line represents Vernon's results, which are from the migrating near a free surface results (dotted line) in Figure 26. The lines on the plots represent the position of the bubble center as it moves through the water column. Both models predict that the bubble will migrate quickly between 0.55 and 0.62 seconds after detonation, though Vernon predicts the bubble will migrate 0.3 meters further. Both models also predict that the bubble will migrate slowly until approximately 0.55 seconds after detonation, though the exact depth of the bubble center predicted differs by up to 0.17 meters between the calculations. Similitude predicts that the bubble should have migrated a greater distance by approximately half of one meter. Similar to the radius time history, this is not a significant problem because the charge is close to the free surface where the accuracy of the similitude equations is suspect.

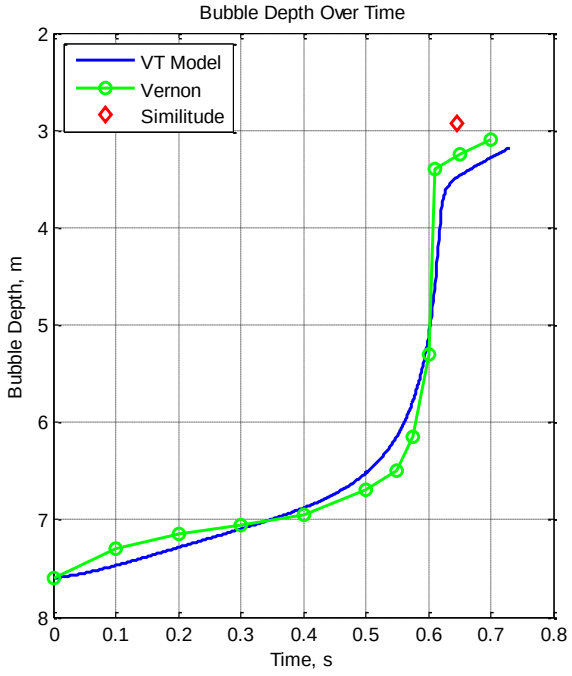

Figure 25 – Bubble Depth Time Histories, Scenario 1, from VT Model (blue) and Vernon [21] (green)

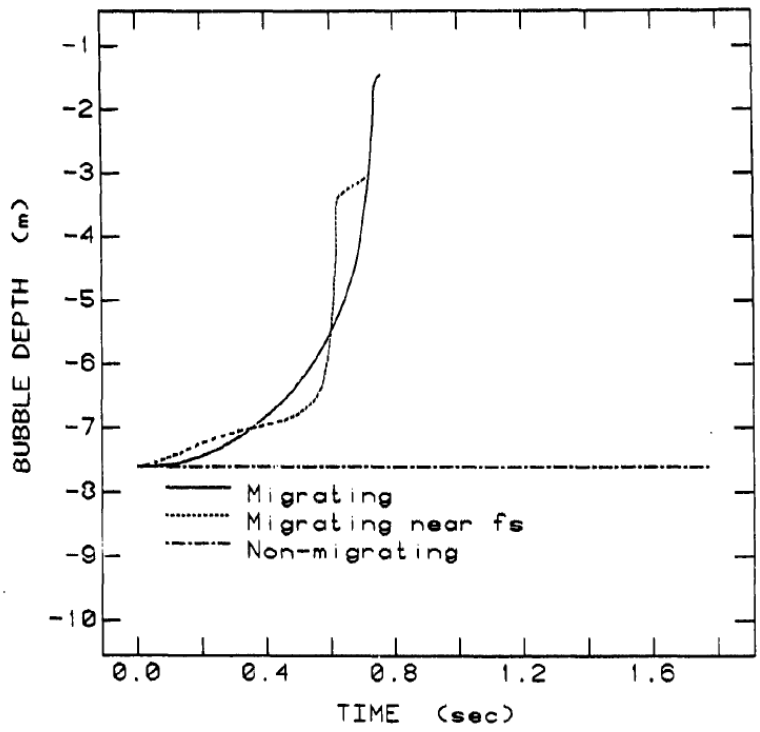

Figure 26 – Bubble Depth Time History, Scenario 1, from Vernon [21]

Scenario 2 is a 227 kg charge of TNT at a depth of 45 meters. Bubble migration, the free surface effect, and the pseudo drag coefficient are included. Figure 27 shows the bubble radius time histories for both the VT model simulation (blue line) and Vernon's simulation (green line), which is from the migrating near a free surface results (solid line) in Figure 28. For the first pulse, the differences between the maximum radius and period calculated by the two methods is negligible. The time histories for both simulations have a maximum bubble radius of approximately 5.4 meters that occurs after 0.22 seconds have elapsed and a bubble period of approximately 0.45 seconds. For the second pulse, the two methods calculate a different maximum radius and bubble period. The VT model calculates a maximum radius that is approximately 0.35 meters smaller than the one calculated by Vernon's method. The bubble period calculated by the VT model is shorter than the one calculated by Vernon by approximately 0.03 seconds. These differences can be attributed to a greater amount of energy being included during the second pulse in the calculations done by Vernon.

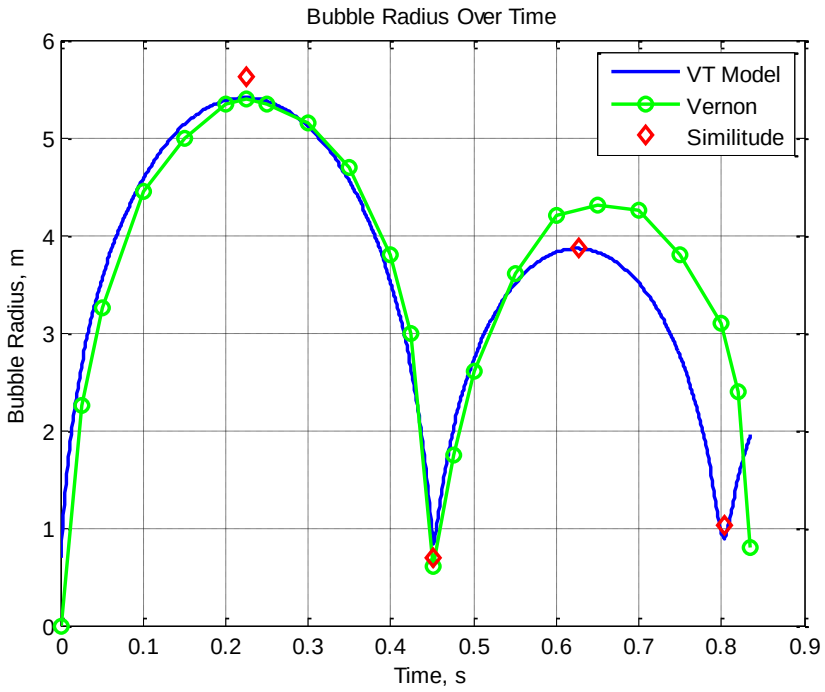

Figure 27 – Bubble Radius Time Histories, Scenario 2, from VT Model (blue) and Vernon [21] (green)

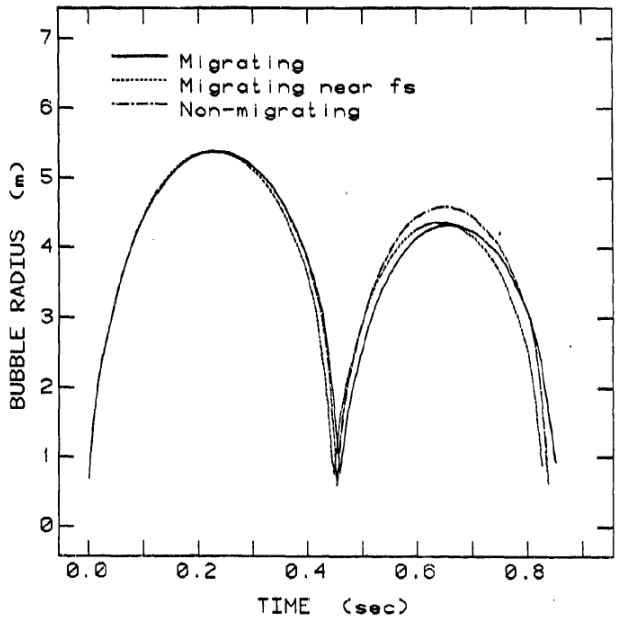

Figure 28 – Bubble Radius Time History, Scenario 2, from Vernon [21]

The similitude values for the second pulse on the plots were calculated using the updated values of depth at the first bubble minimum, as outlined in section 1.2.3.1. The agreement between the VT model and similitude predictions is strong. The time that both maximum and minimum

radii occur closely match those predicted by similitude. The second maximum radius calculated by the VT model almost exactly matches the similitude prediction, while the first maximum radius is approximately 0.2 meters smaller.

The similitude value for second bubble pulse minimum radius was estimated by increasing the value of the first minimum by a factor inversely proportional to the factor used to decrease the similitude maximum radii:

$$A_{min2} = f_2 W^{1/3} = \frac{f_1}{J_2/J_1} W^{1/3} \tag{122}$$

where f_2 is the second pulse bubble minimum radius similitude constant and f_1 is the first pulse bubble minimum radius constant. A similar method was applied for the third pulse, when necessary:

$$A_{min3} = f_3 W^{1/3} = \frac{f_2}{J_3/J_2} W^{1/3} \tag{123}$$

where f_3 is the third pulse bubble minimum radius similitude constant. The minimum radius indicators are used strictly as a visual aide to indicate the times of the minimums, as the times of the minimums are exactly as calculated by similitude, and show that the minimum bubble radius for each successive pulse is larger than its predecessor. The values for the second and third minimum bubble radii are estimations that follow similitude methodology, but have not been confirmed by experiment or study.

The bubble depth time histories for charge 2 are shown in Figure 29. The blue line represents the VT model results and the green line represents Vernon's results, which are from the migrating near a free surface results (dotted line) in Figure 30. The two models predict similar migration paths for the first pulse, as both migrate slowly until approximately 0.4 seconds after detonation, then migrate quickly until slowing down at a depth of approximately 41.3 meters at the first bubble minimum. Some differences exist for the second pulse, as the VT model predicts the bubble will migrate quickly 0.03 seconds sooner than Vernon's model. Both models predict that the bubble will slow before reaching a depth of approximately 38.8 meters at the second bubble minimum. The distance the bubble migrated by the first minimum calculated by the VT model matches the similitude prediction.

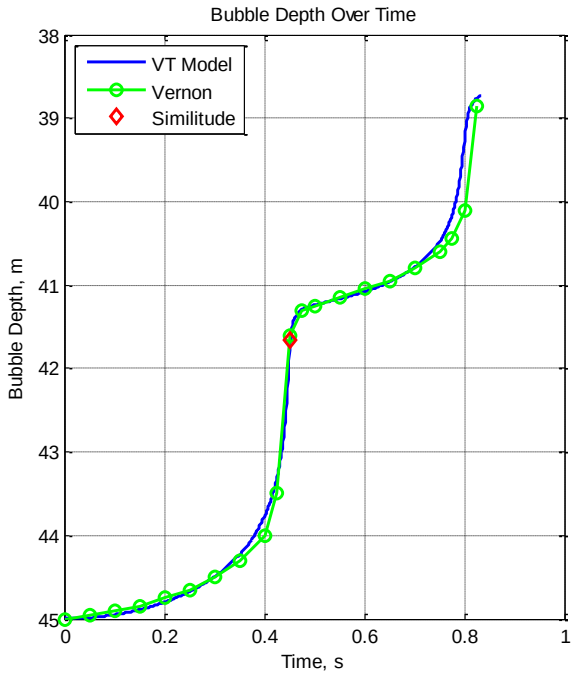

Figure 29 – Bubble Depth Time Histories, Scenario 2, from VT Model (blue) and Vernon [21] (green)

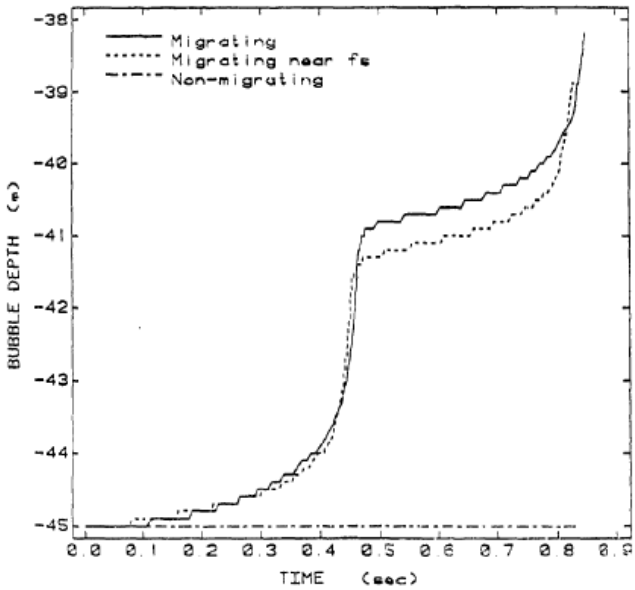

Figure 30 – Bubble Depth Time History, Scenario 2, from Vernon [21]

Scenarios 3, 4, and 5 were simulated for three full bubble pulses to show the agreement of the VT model with similitude for charges similar to those carried on torpedoes or within mines. All percent errors referenced in these comparisons are calculated according to equations (120) and (121). The radius time history for scenario 3, a 544 kg TNT charge at a depth of 30 meters, is

shown in Figure 31. The greatest difference between the similitude and VT model calculations is the first maximum radius, where the model predicts a radius about three percent smaller than that predicted by similitude. The bubble minimums and maximums for both methods are at the same times, with no errors greater than one percent, and the maximum radii for the two secondary pulses are within 1.5 percent.

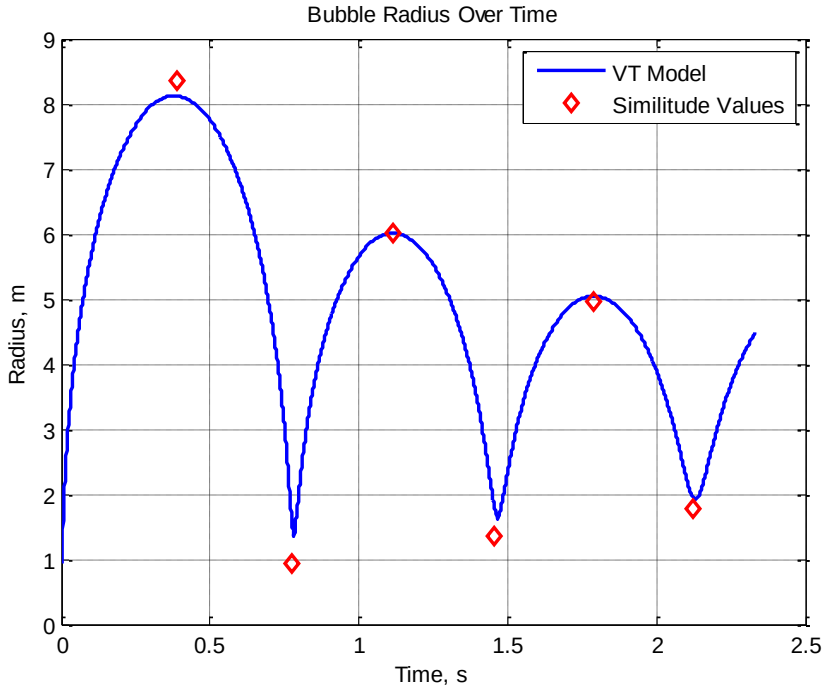

Figure 31 – Scenario 3 Bubble Radius Time History

The radius time history for the scenario 4, a 265 kg TNT charge at a depth of 20 meters, is shown in Figure 32. The greatest difference between the similitude and VT model calculations is during the third bubble pulse, where the model predicts a radius about three percent larger and a period 4.6 percent shorter than those predicted by similitude. The first and second bubble minimums for both methods are at the same times, with errors less than half of one percent, and their associated maximum radii agree within three percent.

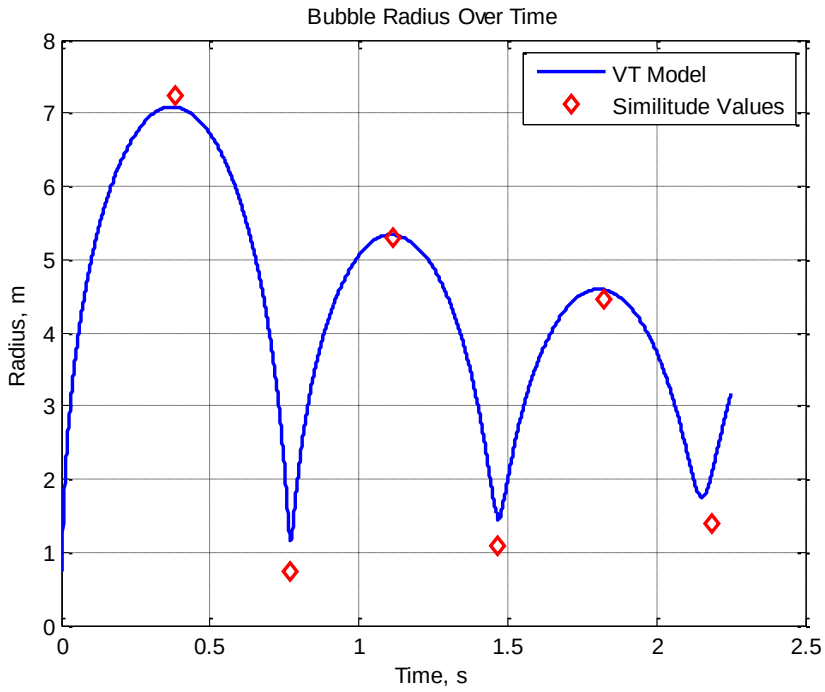

Figure 32 – Scenario 4 Bubble Radius Time History

The radius time history for scenario 5, a 1500 kg TNT charge at a depth of 60 meters representing a large, deep water mine, is shown in Figure 33. The greatest difference between the similitude and VT model calculations is the first maximum radius, where the model predicts a radius 4.2 percent smaller than that predicted by similitude. The first and second bubble minimums and maximums for both methods are at the same times, with errors less one percent. The maximum radii for the two secondary pulses are within 1.5 percent, while the third period is within two percent.

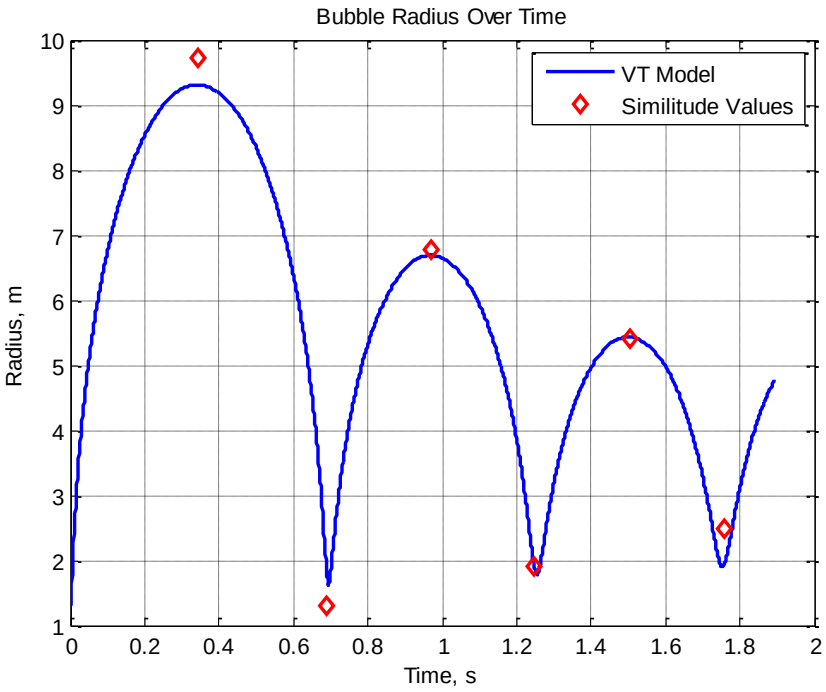

Figure 33 – Scenario 5 Bubble Radius Time History

Table 14 contains the percent errors between the similitude and VT model calculations for scenarios 1 through 5. The consistently small percent errors across all presented scenarios indicates a strong agreement between similitude and model results, which further verifies the accuracy of the VT bubble model.

Table 14 – Bubble Assessment Scenario Percent Errors

Scenario	**1st Pulse %Error A_{max}**	**1st Pulse % Error T**	**2nd Pulse % Error A_{max}**	**2nd Pulse % Error T**	**3rd Pulse %Error A_{max}**	**3rd Pulse % Error T**
1	-0.66%	-4.12%	N/A	N/A	N/A	N/A
2	-3.70%	0.07%	-0.04%	-0.77%	N/A	N/A
3	-2.78%	0.68%	0.17%	0.99%	1.50%	-0.84%
4	-2.07%	0.32%	0.94%	0.05%	2.80%	-4.64%
5	-4.24%	0.56%	1.26%	0.27%	0.44%	-1.94%

The fluid accelerations produced by the VT model were compared with plots from Hicks [20] for a 500 pound (lb) charge at a depth of 50 feet (ft). The blue line in Figure 34 represents the results produced by the VT bubble model, while the green line with circles shows the migrating bubble results (dashed line) from Hicks (Figure 35). The peak fluid acceleration values are

approximately the same and occur at the same time. The shapes of the two curves are slightly different, with the VT model predicting a greater impulse before the peak occurs. While this doesn't match with the published results of Hicks, it does match the shape of the fluid pressure results which are the directly related to fluid accelerations, from small explosion experiments by given by Arons [52].

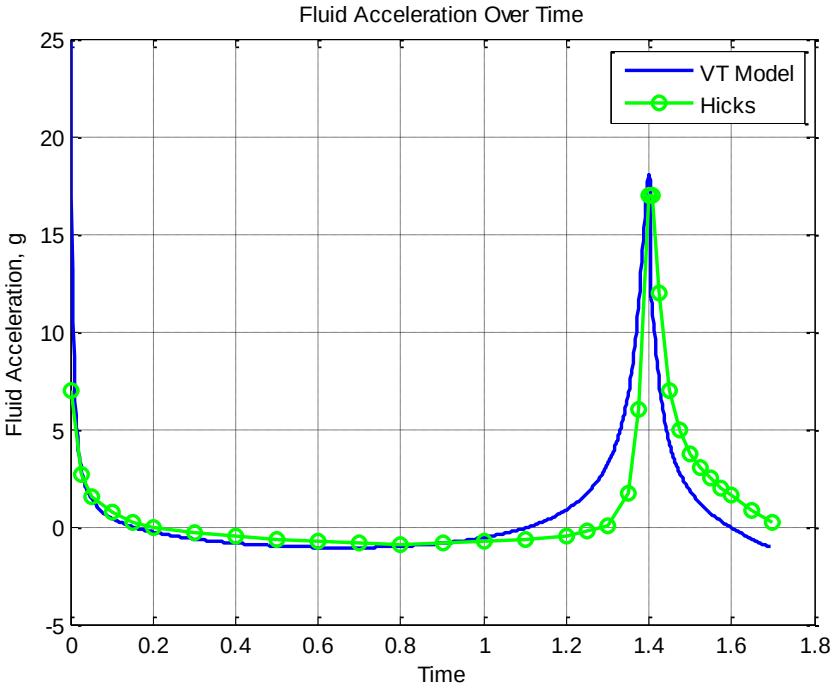

Figure 34 – Scenario 6 Surface Fluid Accelerations, from VT Model (blue) and Hicks [20] (green)

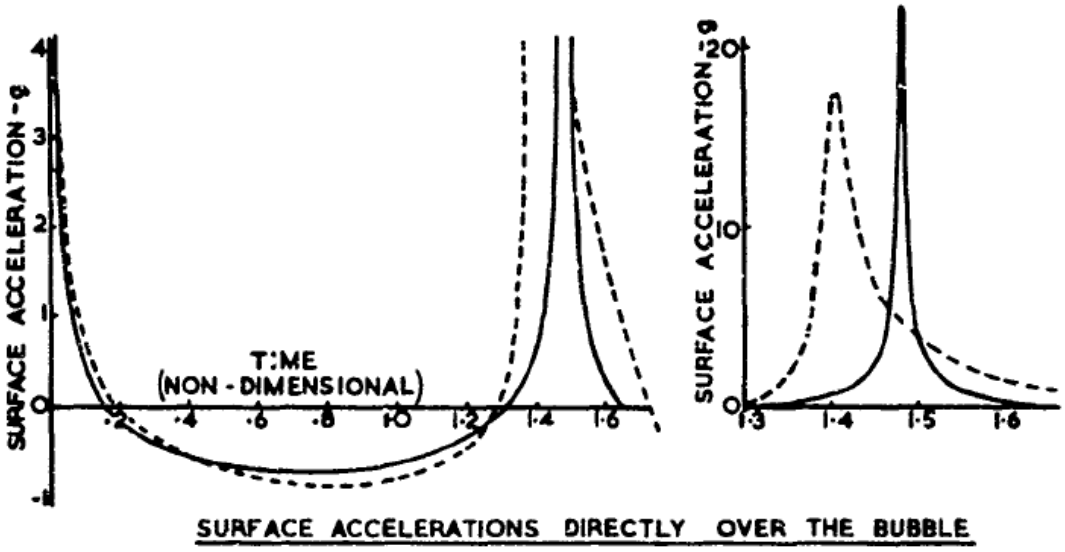

Figure 35 – Surface Fluid Accelerations, 500 lb charge at 50 ft, from Hicks [20]

Throughout these example scenarios, it was shown that the VT model produces results that closely match the bubble behavior predicted by similitude and sample results from previous analyses using similar models. In saying this, the VT model accurately calculates the behavior of UNDEX bubbles and is suitable for use in ship whipping analyses.

2.4.2 Ship Whipping Model

There is little publically available data from ship whipping experiments, and much of it does not contain the details necessary to set up a model to compare results, which severely limited the options for rigorous model assessment. Instead, a comparison of VT model results with the results presented by Hicks [20], Vernon [21], and Zhang and Zong [51] is used as the primary method of assessing the accuracy of the VT model.

Each of the published model results has a combination of knowledge gaps, caused by lack of provided details, and significant internal inconsistencies. The results published by Hicks are accompanied by the most thorough model and methodology descriptions. However, it is unclear how a doubling effect of the fluid accelerations is included in his calculations. The VT model consistently calculates deflections that are approximately half the magnitude of the deflections calculated by Hicks, though the bubble and fluid acceleration results calculated by the two methods are similar.

Vernon provides a complete outline of the derivation of his bubble model and fluid acceleration equations. His bubble model was used to assess the accuracy of the VT bubble model in section 2.4.1. It was found that the two models calculate nearly identical behavior for the first bubble pulse, with some slight differences in results for the second pulse. The VT bubble model was determined to be more accurate for the second pulse because its predicted results compared more favorably with the output from the similitude equations. However, no description of the structural model is provided by Vernon and only limited details are given for the ship model used in the whipping results calculations. Also, Vernon's deflection results are small when compared to those from the VT model.

Zhang and Zong provide a complete summary of the methodology used to perform their bubble, structural, and whipping calculations. However, a complete lumped mass representation of the ship used is not given. Also, the provided hull girder natural vibration frequencies do not match the behavior of the whipping results. This could be due to an error reporting the natural

frequencies or a significant problem in the vibration equations of motion. In addition, the bubble results given by Zhang and Zong do not match similitude results as well as the VT bubble model.

Throughout the following comparisons, it is shown that the VT whipping model gives consistent results within the extremes of the other methods. However, more detailed and accurate data is needed to validate and verify the whipping responses predicted by the VT model.

2.4.2.1 Hicks Results Comparison

Hicks utilized a sample destroyer to present his results. The characteristics of this ship are given in Appendix A. A comparison of the mode shapes for the ship calculated by the VT model and Hicks is shown in Figure 36. The circles on the plots represent the location of each lumped mass. As shown in Figure 37, Hicks did not include a scale on the vertical axis of his plots, so the Hicks values shown on the plots are scaled to give a magnitude similar to the VT model results.

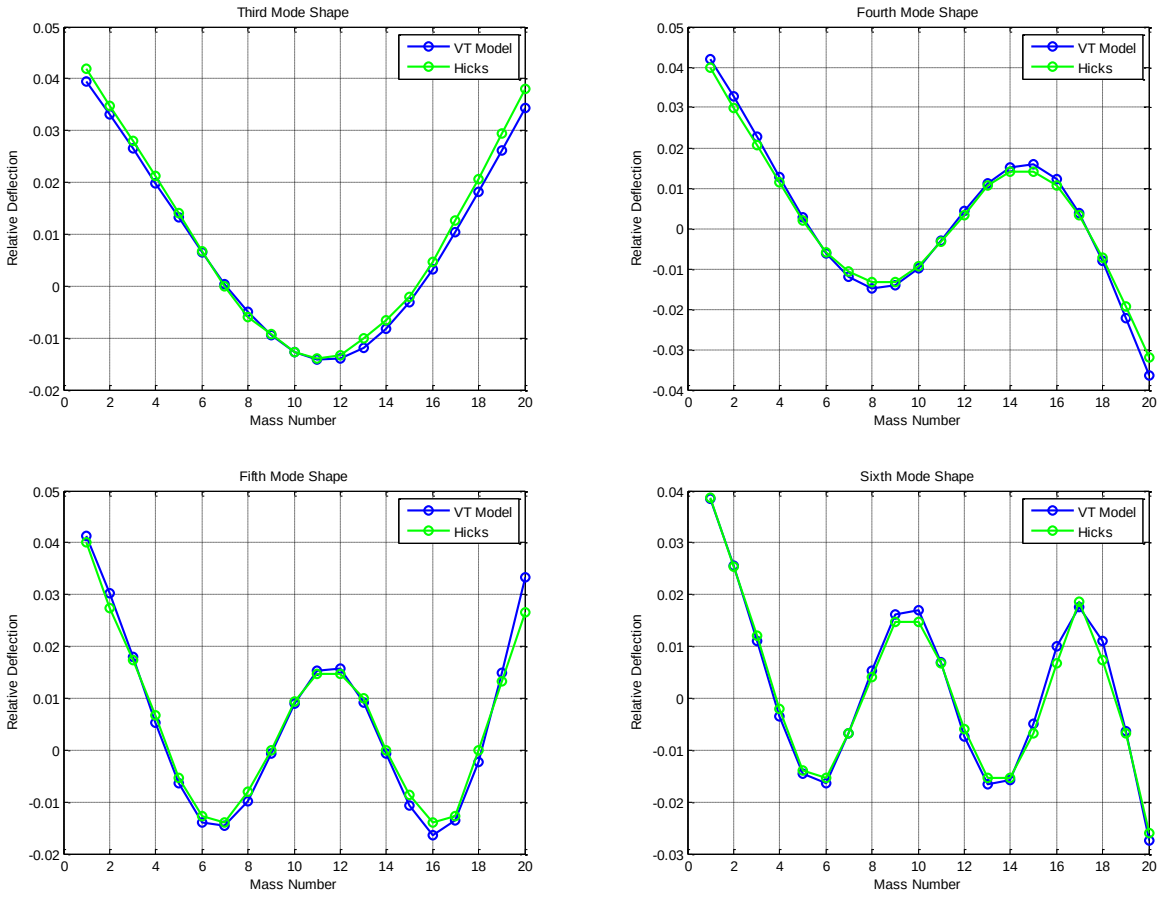

Figure 36 – Destroyer Mode Shapes, from VT Model (blue) and Hicks [20] (green)

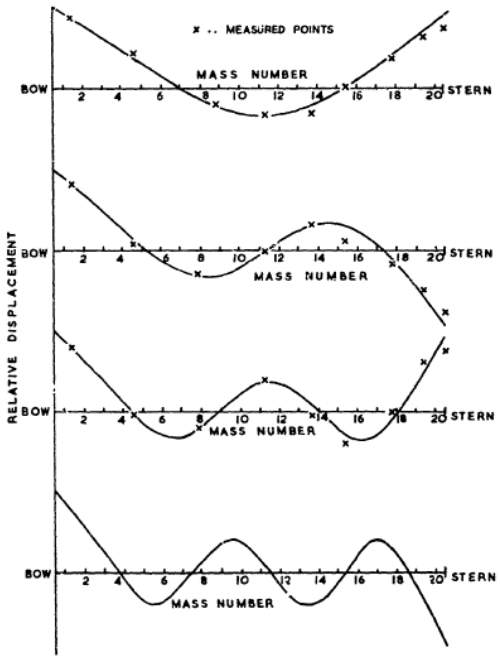

Figure 37 – Destroyer Mode Shapes [20]

The natural vibration frequencies of the hull girder were also calculated and compared. The values from both the VT model and Hicks are shown in Table 15. The VT model-produced frequencies agree well with the Hicks calculated frequencies, with percent errors between one and two percent for each mode shape. The small variations between the two sets of values may be due to a difference in the selected material constants, such as Young's modulus or Poisson's ratio, used in the calculations.

Table 15 – Destroyer Natural Vibration Frequencies, from VT Model and Hicks [20]

Mode	VT Model Frequency (Hz)	Hicks Frequency (Hz)
1 (Heave)	0.207	0.21
2 (Pitch)	0.227	0.23
3	1.513	1.54
4	3.092	3.13
5	4.609	4.67
6	6.333	6.42
7	8.001	8.09
8	9.501	9.61

The modal coefficient produced by a migrating bubble resulting from a 500 pound charge of TNT at a depth of 45 feet directly below midship of the destroyer for its third vibration mode is shown in Figure 38. The circles on the line showing Hicks's results represent the data points used in creating the approximate curve. The modal coefficients from Hicks shown in Figure 38 are scaled by a factor of ten to better compare with the VT model-produced results. Prior to the arrival of the first bubble pulse, the third mode modal coefficient has the same shape as the result given by Hicks. After the arrival of the bubble pulse, the VT model results begin to deviate from the sample results of Hicks. The VT model calculates a larger magnitude of motion than Hicks's model in response to the bubble pulse, though the overall pattern of the motion is the same. This difference is likely due to the greater impulse acting on the ship that is predicted by the VT bubble model compared to Hicks's bubble predictions, as shown in Figure 34. Also, the bubble pulse from the VT model occurs later than the one predicted by Hicks, which causes the peaks of the second oscillation to not occur at the same time.

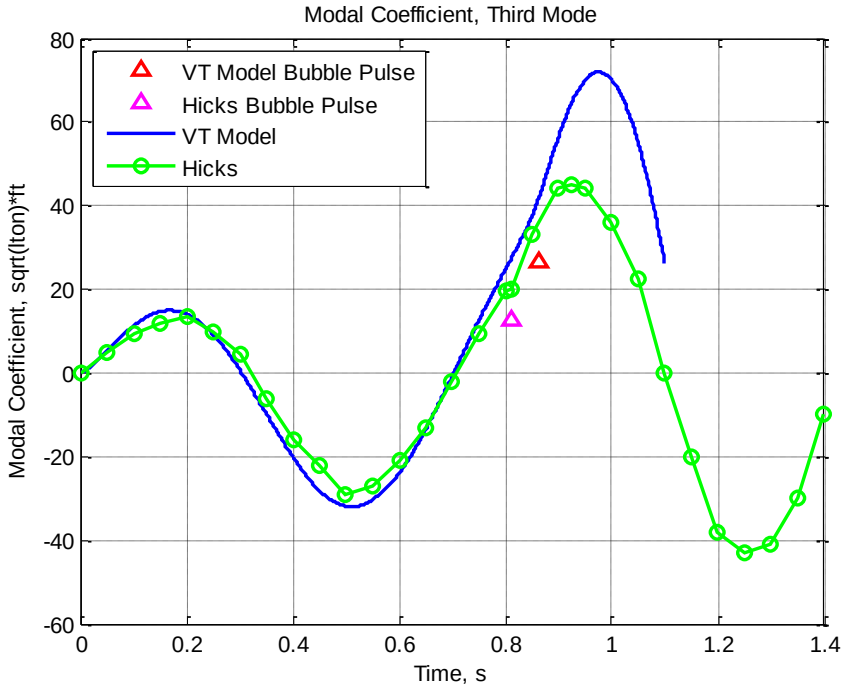

Figure 38 – Destroyer Third Mode Modal Coefficients Comparison

The resulting whipping response of the midship section of the destroyer to the same charge is shown in Figure 39. The rigid body modes were included in the analyses done by the VT model in this section because they were included in the analyses done by Hicks. The shape of both plots are essentially the same, especially before the arrival of the bubble pulse, though the magnitudes

are different. Before the bubble pulse, the deflections predicted by the VT model are approximately half of those predicted by Hicks. After the bubble pulse, the deflections are much closer, though the ones predicted by Hicks are still larger. Also, the VT model predicts that the peak of the second oscillation is greater than the first peak, while Hicks predicts the opposite. The effects of a later bubble pulse arrival are also evident, as the time of the second peak predicted by the VT model is later than what is predicted by Hicks. In addition, the VT model predicts a negative deflection just prior to the arrival of the bubble pulse, while Hicks does not.

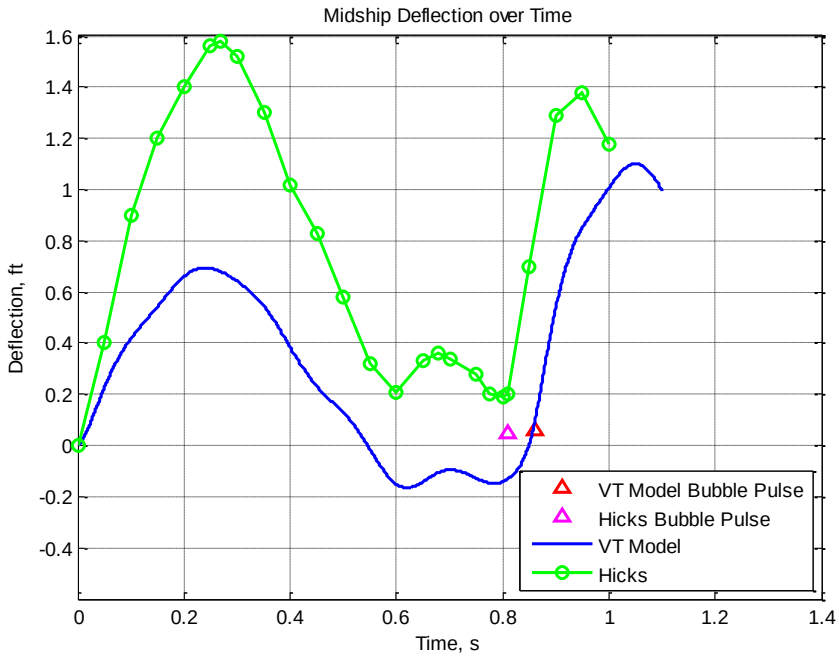

Figure 39 – Destroyer Midship Deflection due to 500 lb charge at 45 ft below midship from VT Model (blue) and Hicks [20] (green)

Figure 40 shows the deflection at midship caused by a migrating bubble resulting from a 500 pound charge of TNT at a depth of 60 feet directly below midship of the destroyer. The rigid body modes are included in the analysis. The plots follow very similar patterns, with peaks and minimums occurring at approximately the same times, though the magnitudes are off by a factor of roughly two. Also, the VT model predicts a period of negative deflection just prior to the bubble pulse arriving, while Hicks does not.

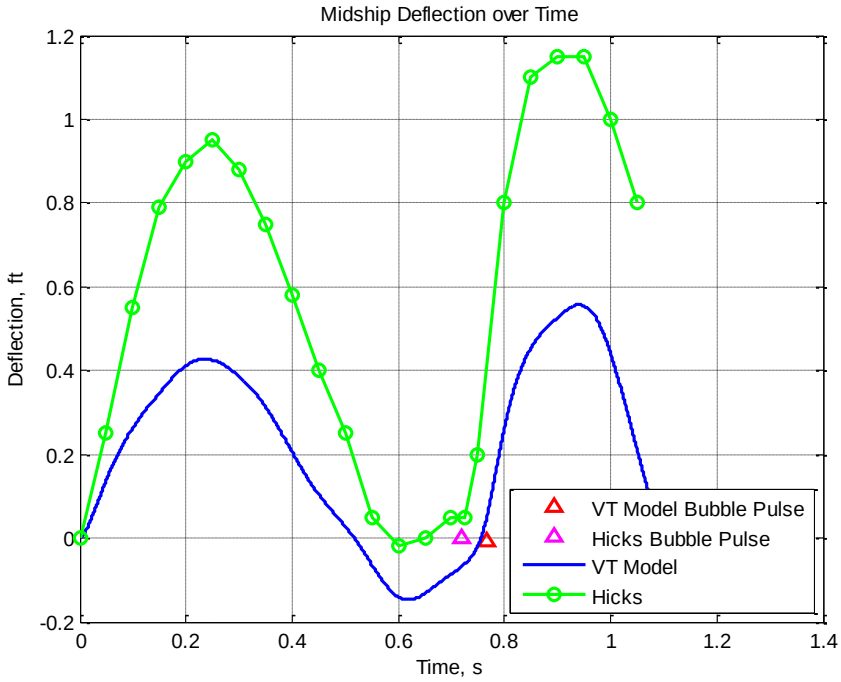

Figure 40 – Destroyer Midship Deflection due to 500 lb charge at 60 ft below midship from VT Model (blue) and Hicks [20] (green)

2.4.2.2 Vernon Results Comparison

Vernon presents one case of whipping results, but doesn't provide a lumped mass ship model. However, some ship particulars are provided, so an attempt was made to recreate the results using an approximate ship model that matched the given particulars. The ship is said to be a "typical frigate-sized warship" with a third vibration frequency of 1.68 Hertz and a fourth vibration frequency of 3.94 Hertz. Only modes three, four, and five were included in the analysis. The ship also experiences its greatest whipping deflections from charges placed 70 meters aft of the bow, which is said to be just aft of midship. A damping equivalent to five percent was also applied during the simulation performed by Vernon.

A sample lumped mass ship model developed from a MAESTRO model, which is discussed in Chapter 3, was utilized as the approximate ship model. The ship's displacement is 6450 metric tons and its length is 124.2 meters, which are both within the range of modern frigate sizes. Its third and fourth vibration frequencies were tuned to match Vernon's ship by scaling the section shear areas and moments of inertia. This model experiences its greatest deflections from

charges placed just aft of midship, and the ship length was selected so this point was 70 meters aft of the bow. No damping was added to the VT model for this analysis.

Vernon selected a 167 kg TNT charge located at a depth of 24 meters below the surface, which produces a bubble with an oscillation frequency similar to the natural frequency of the ship. The charge was placed 70 meters aft of the bow directly below the ship and the bubble was allowed to migrate. The deflection results from the simulation at the bow and stern are shown in Figure 41 and Figure 42, respectively. The results for the VT model and Vernon's model follow similar patterns throughout the entire simulation at both locations, as they have peak values and cross the horizontal axis at roughly the same times. The shapes are mostly similar, specifically at the stern, though the VT model results at the bow are not as smooth as those given by Vernon. However, the VT model results are approximately four times larger than Vernon's.

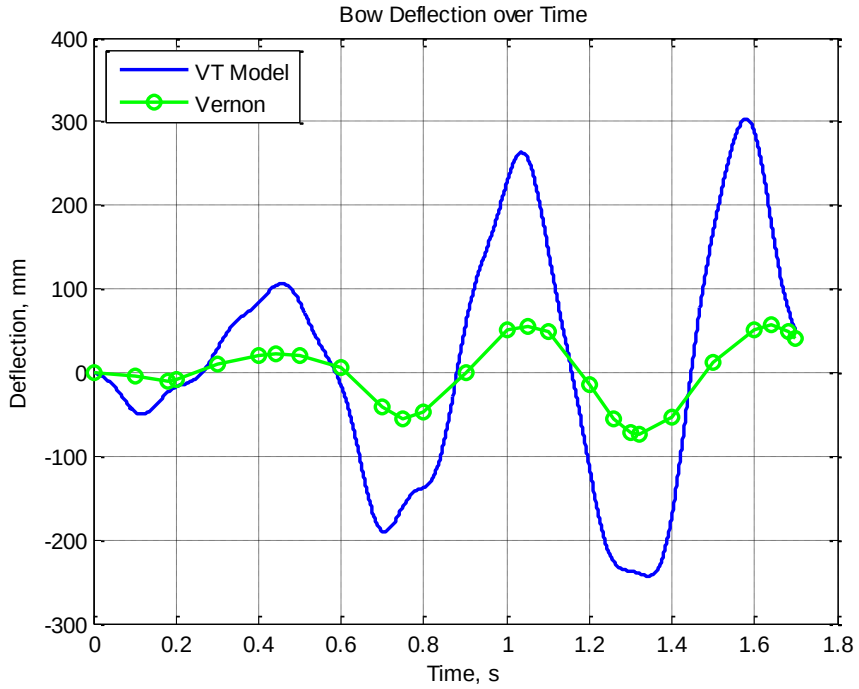

Figure 41 – Frigate Bow Deflection due to 167 kg charge at 24 m depth from VT Model (blue) and Vernon [21] (green)

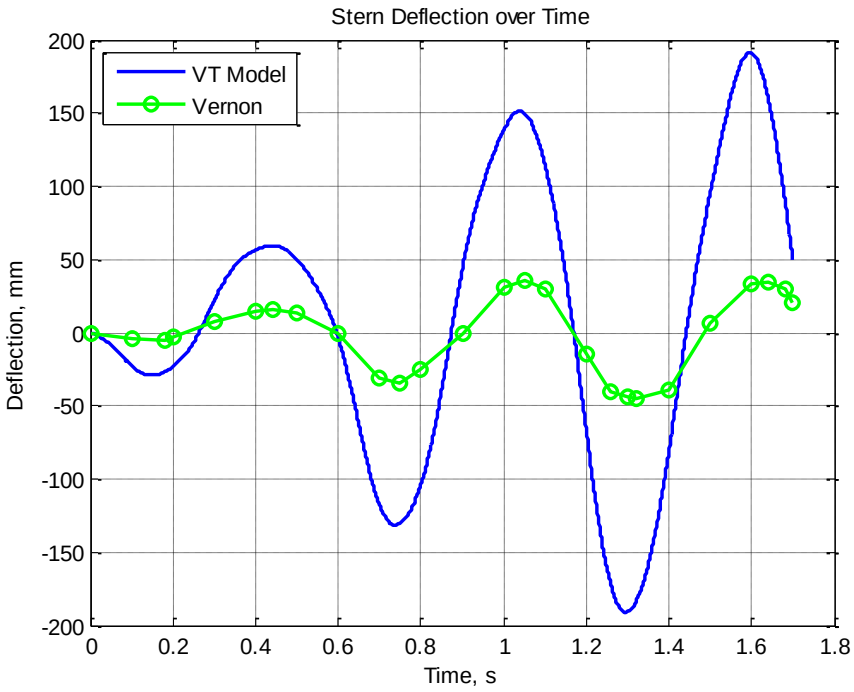

Figure 42 – Frigate Stern Deflection due to 167 kg charge at 24 m depth from VT Model (blue) and Vernon [21] (green)

2.4.2.3 Zhang and Zong Results Comparison

Zhang and Zong present deflection-time histories for multiple whipping scenarios calculated using a potential flow-based migrating bubble model and an elastic ship vibration model that utilizes a lumped mass formulation. However, they do not provide a lumped mass ship model. They do provide several ship characteristics, which make it possible to develop an approximate ship model with similar whipping behaviors. The particulars given by Zhang and Zong and the same particulars of the approximate ship used in the VT model simulations are shown in Table 16. The approximate ship model was developed from the destroyer described by Hicks by scaling the ship properties until the length, displacement, and natural vibration frequencies matched the values given by Zhang and Zong.

Table 16 – Zhang and Zong Ship Particulars

Characteristic	Zhang and Zong	Approximate Model
Length Overall (m)	215	215
Length Between Perpendiculars (m)	204	-
Displacement (tonnes)	61046	61046
Third Natural Frequency (Hz)	2.03	2.028
Fourth Natural Frequency (Hz)	4.12	4.121
Added Mass (tonnes)	-	89402

First, the two bubble models are compared. The bubble radius comparison for a migrating bubble resulting from a 200 kilogram charge of TNT at a depth of 20 meters is shown in Figure 43. The first oscillation of the bubble is fairly similar between the two models, with the shapes being similar and maximum radii approximately equal. However, the VT model predicts a longer first oscillation period than Zhang and Zong. The two curves are not close during the second oscillation, as the VT model calculates a much smaller maximum radius and oscillation period. This is likely due to Zhang and Zong not applying an energy dissipation factor between oscillations.

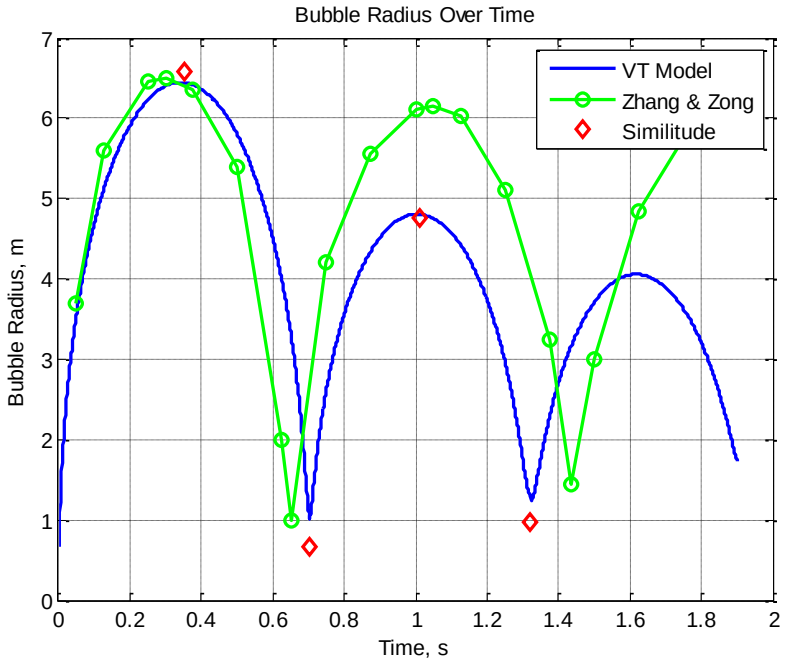

Figure 43 – Bubble Radius, 200 kg charge at 20 m, from VT Model (blue) and Zhang and Zong [51] (green)

The fluid accelerations output by the two bubble models for the same charge are shown in Figure 44. The fluid accelerations were set to zero for the first 0.05 seconds to ignore the kickoff velocity produced by the initial bubble expansion and shock wave, as done by Zhang and Zong. For both pulses, the VT model predicts a higher peak fluid acceleration by approximately 25 meters per second squared than the values presented by Zhang and Zong. Also, the VT model has a more negative minimum and has a negative value over a longer period of time during each oscillation. The shapes of the curves are also different, with the results given by Zhang and Zong having a greater curvature and impulse prior to the peak, while the impulse calculated by the VT model is more symmetric about the peak. The peaks also do not occur at the same time, but this was expected given the difference in the predicted oscillation periods shown by the bubble radius comparison.

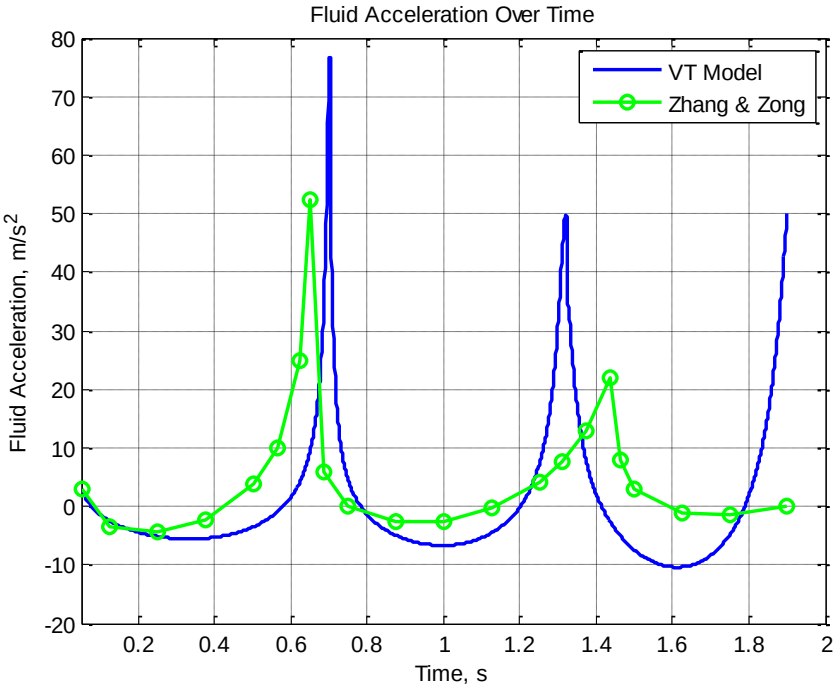

Figure 44 – Surface Fluid Accelerations, 200 kg charge at 20 m, from VT Model (blue) and Zhang and Zong [51] (green)

The deflection at midship caused by a migrating bubble resulting from a 200 kilogram charge of TNT at a depth of 30 meters directly below midship of the ship is shown in Figure 45. The first 0.05 seconds of the fluid accelerations are ignored. The most significant difference between the two curves is in the overall vibration behavior of the ships. The VT model is oscillating roughly two times per second, while the ship in the analysis done by Zhang and Zong completes

approximately eighty percent of an oscillation per second. This implies that the natural vibration frequencies of the ship model reported by Zhang and Zong are not correct. Several other whipping deflection scenarios are included in the analysis done by Zhang and Zong, and the ship behaves in this way during each analysis. Though it is notable that the VT model-predicted deflections are less than those predicted by Zhang and Zong, further comparison is not useful due to the inaccurate ship data provided by Zhang and Zong.

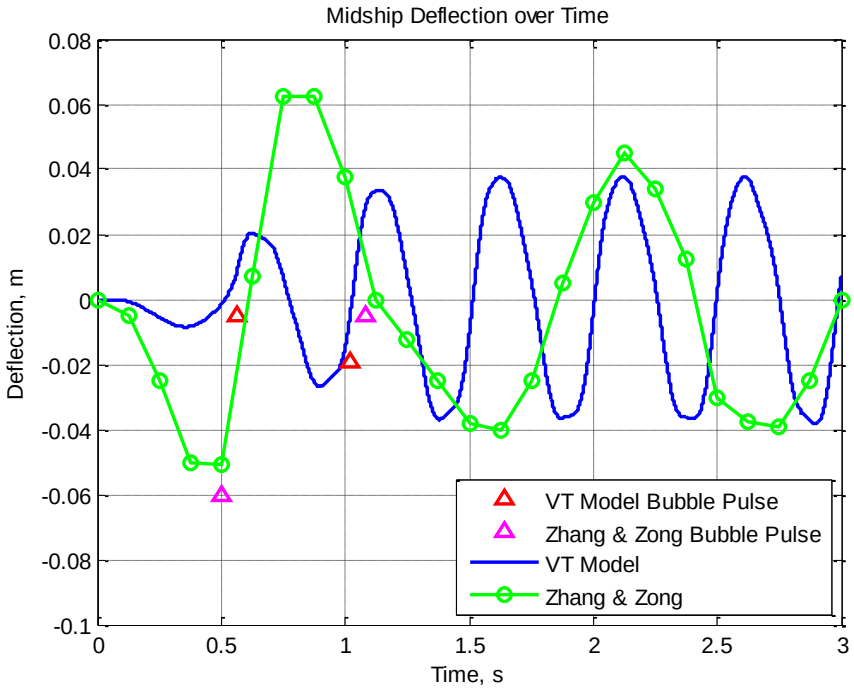

Figure 45 – Midship Deflection due to 200 kg charge at 30 m below midship from VT Model (blue) and Zhang and Zong [51] (green)

2.4.2.4 Conclusion

The scarce and incomplete publically available UNDEX-induced ship whipping data has made it difficult to assess the accuracy and validity of the VT whipping model. This was further complicated by the inconsistencies between the results of the published methods in the predicted severity of whipping motions. Despite these difficulties, it was shown that the VT whipping model gives consistent results within the extremes of these results.

Though the VT model was unable to reproduce any of the results from the available methods, the methods used to develop the VT model are sound and the bubble model was shown to accurately predict the behavior of an UNDEX bubble for up to three pulses. For this reason, and

the noted inconsistencies in the available results, the author is confident the whipping results produced by the VT model are correct. However, more detailed and accurate data is needed to validate and verify the whipping responses predicted by the VT model.

Chapter 3 Structural Analysis of Ship Whipping Deformations

3.1 Overview

This chapter describes the methodology used to analyze the overall response of a ship structure to the whipping deflections predicted by the VT whipping model described in Chapter 2. The behavior of the ship structure while under its most severe UNDEX-induced whipping bending load is investigated as a quasi-static load case. The dynamic load caused by the ship whipping is assumed to be quasi-static due to the low frequency of its motions, especially compared to the loading that results from an UNDEX shock wave impact. Analyzing only a small number of the worst case loading conditions the ship experiences also keeps the analysis time and necessary computer resources to a minimum. MAESTRO is utilized as the structural analysis tool, with its failure mode evaluation capability being the primary method in determining if the structure will fail as a result of the loading.

3.1.1 MAESTRO Failure Mode Evaluation

MAESTRO provides the user with numerous analysis tools and methods which allow for the evaluation of both the local and global ship structure in response to various loading conditions. One of the primary methods to determine the ability of a structure to withstand a given loading condition is failure mode evaluation.

A failure mode, also known as a limit state, is a condition in which the structure fails to perform its intended function [41]. MAESTRO provides two different types of failure mode evaluations for stiffened panels, MAESTRO and ALPS/ULSAP (Analysis of Large Plated Structures)/(Ultimate Limit State Assessment Program), and one failure mode evaluation for the progressive collapse of the hull girder, ALPS/HULL. Each of these evaluations investigate a number of possible limit states for each component of the structure under the given loading condition. In general, failure modes are component-specific, with all parts of the structure (panels, beams, and all of their corresponding elements), evaluated against a set criteria to determine if an ultimate or serviceability limit state is reached. An ultimate limit state, such as collapse or buckling, is defined as a state in which the structure fails in its load-bearing role. A serviceability limit, such as a material yielding, involves the deterioration or loss of less vital functions of the component [41].

To evaluate if the structure is capable of withstanding the applied load condition, MAESTRO first calculates a limiting load effect for each element in each failure mode. This value is compared to the load effect caused by the loading condition for the same failure mode. For the structure to be safe under the given loading condition, the limiting load effect must be greater than the load effect by a certain factor of safety. From this requirement, a strength ratio, *R*, is defined as:

$$R = \frac{\gamma Q}{Q_L} \leq 1 \tag{124}$$

where Q is the load effect, Q_L is the limiting load effect, and γ is the factor of safety [41]. This strength ratio is then used to define the adequacy parameter, *g(R)*, which is a normalized measure of safety against structural failure defined as:

$$g(R) = \frac{1 - \gamma R}{1 + \gamma R} \tag{125}$$

The value of adequacy will always lie between negative one and one [41]. A structural element with a value of negative one under a given loading condition in a specific failure mode indicates the structure is fully incapable of bearing the load in that failure mode, while a value of one indicates a completely robust structure. An element with a positive value of adequacy is capable of bearing the load from the loading condition without failing. Adequacy is used to detail and describe the ability of the ship structure to withstand the loading conditions caused by the whipping motion in each MAESTRO structural analysis presented. Figures showing the adequacy of the structure will display the minimum calculated value of adequacy from any of the analyzed failure modes.

3.1.1.1 Stiffened Panel Failure Modes

MAESTRO offers two different methods of failure mode evaluation for stiffened panels and their components: MAESTRO and ALPS/ULSAP. MAESTRO evaluates fourteen different failure modes, including the collapse, yield, serviceability, and failure of panels and the tripping, collapse, and yield of beams. These failure modes analyze the structure for a possible deficiency in nearly all directions and combinations of loading. The listing of all evaluated failure modes, along with a simplified methodology and description for each mode, is available in the MAESTRO Help manual [41]. More detailed theory and descriptions can be found in Hughes [39].

ALPS/ULSAP is an ultimate limit state analysis of the failure modes of stiffened panels. Its thirteen total limit states cover various failure modes associated with the ultimate strength of panels, girders, and frames [41]. These failure modes analyze the structure for a possible deficiency in nearly all directions and combinations of loading. The listing of all evaluated failure modes is available in the MAESTRO Help menu [41]. ALPS/ULSAP assumes a stiffened panel is subject to a combined in-plane and lateral pressure load, as shown in Figure 46. The detailed definitions, theory, and methodology for each of the failure modes evaluated by ALPS/ULSAP can be found in various works by Paik [53, 54, 55].

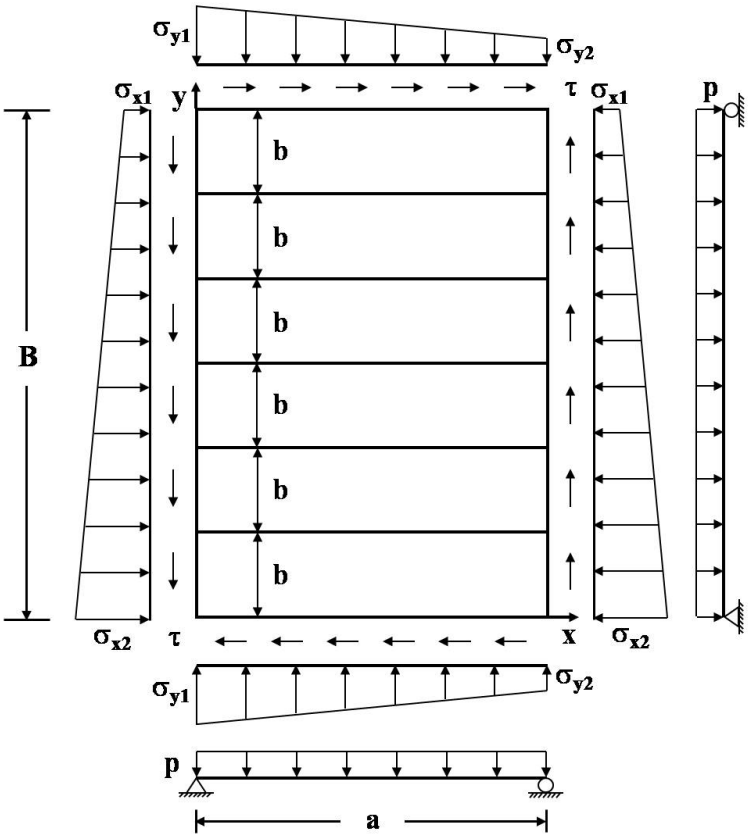

Figure 46 – Stiffened panel subject to a combined in-plane and lateral pressure load [53]

Due to its use of ultimate strength criteria, instead of allowable working stress properties, ALPS/ULSAP failure mode analysis tends to predict that a structure is more robust when compared to MAESTRO failure mode analysis. For the purpose of this whipping analysis, an ultimate strength approach is more appropriate, as ship survival is the primary concern. In addition, ALPS/ULSAP has been extensively validated [53, 56], and it is used as the primary method of determining the adequacy of the ship structure to withstand the whipping loading.

3.1.1.2 Hull Girder Collapse: ALPS/HULL

The ALPS/HULL module in MAESTRO calculates the progressive collapse behavior of ship hulls using ultimate strength criteria. This is done by progressively increasing the magnitude of the applied load on a section of interest. To decrease the necessary computation and modelling time, only one section of the hull is modeled with large structural units. This section is then analyzed using the intelligent super-size finite element method (ISFEM) [57]. It can accommodate the effects of all possible hull girder load components, such as vertical and horizontal bending, vertical and horizontal shearing force, torsion, and local pressure loads [41]. These sectional load components are shown in Figure 47. A listing of each failure mode investigated by ALPS/HULL is given in. Table 17. A more detailed description of the theoretical basis for ALPS/HULL modes can be found in various works by Paik [57, 58].

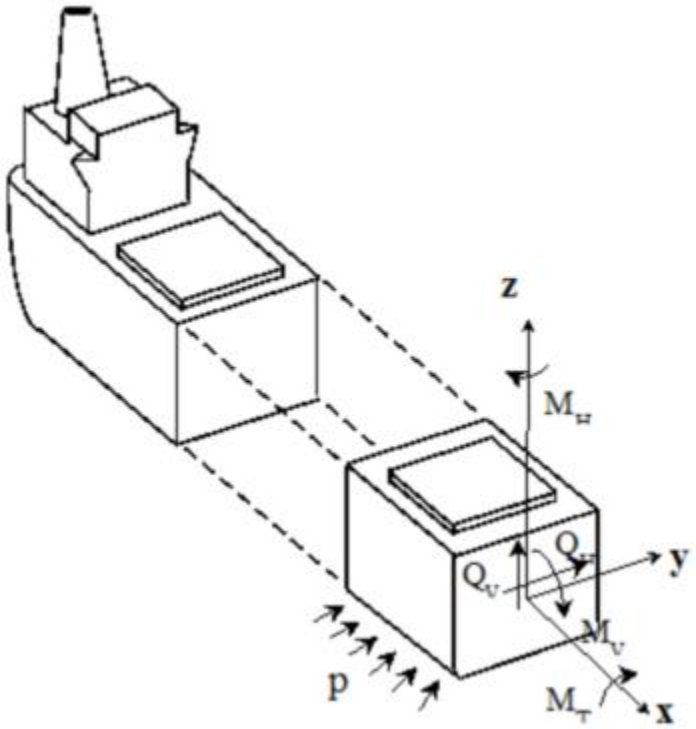

Figure 47 – Hull Girder Sectional Load Components [41]

Table 17 – ALPS/HULL Failure Modes [41]

Failure Mode Description	Acronym
Overall Collapse	OC
Collapse of plating between stiffeners	PB
Beam-Column Type Collapse	BCC
Local Buckling of Stiffener Web	SWB
Flexural-Torsional Buckling of Stiffener	TR
Gross Yielding	GY
Rupture due to Tension	RT
Crushing due to Compression	CC

3.1.2 Ship Model Description

The ship model used in this study is a 6,160 metric ton, 138 meter small guided missile destroyer (DDG). The ship's mission includes anti-submarine and anti-surface warfare, among other things, with possible operations in littoral zones. With this mission comes the threat of experiencing an UNDEX event, whether from a torpedo launched by a submarine or a mine moored to the ocean floor. The ship, shown in Figure 48, features a deckhouse forward of midship, a large hangar aft of the deckhouse, and a flight deck at the stern.

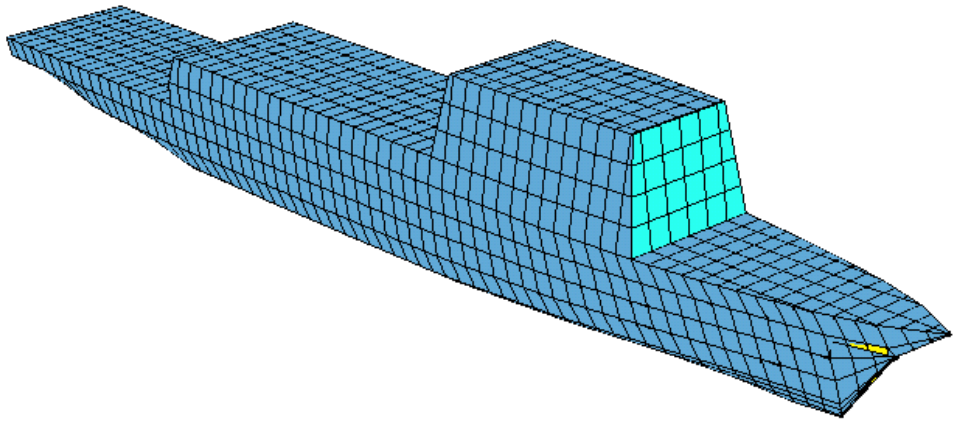

Figure 48 – DDG MAESTRO Model

The ship structure was designed to meet the requirements for classification outlined in the American Bureau of Shipping Naval Vessel Rules. These regulations require that the ship structure must have the ability to withstand the loading from a design wave. For this ship, the design wave

has an amplitude of 3.44 meters and a wavelength of 131.4 meters, which is equal to the design waterline length of the ship. The deformation of the hull girder while under the hogging design wave loading, magnified by 230 to allow for better visualization of the deflected shape, is shown in Figure 49. The response of the structure in terms of the MAESTRO adequacy of each element for this loading condition is shown in Figure 50. All elements are adequate, with the elements along the keel near midship closest to being inadequate.

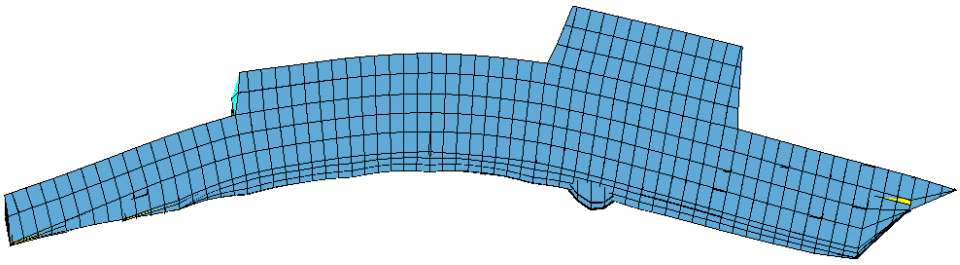

Figure 49 – DDG Hull Girder Deformation, Hogging Design Wave

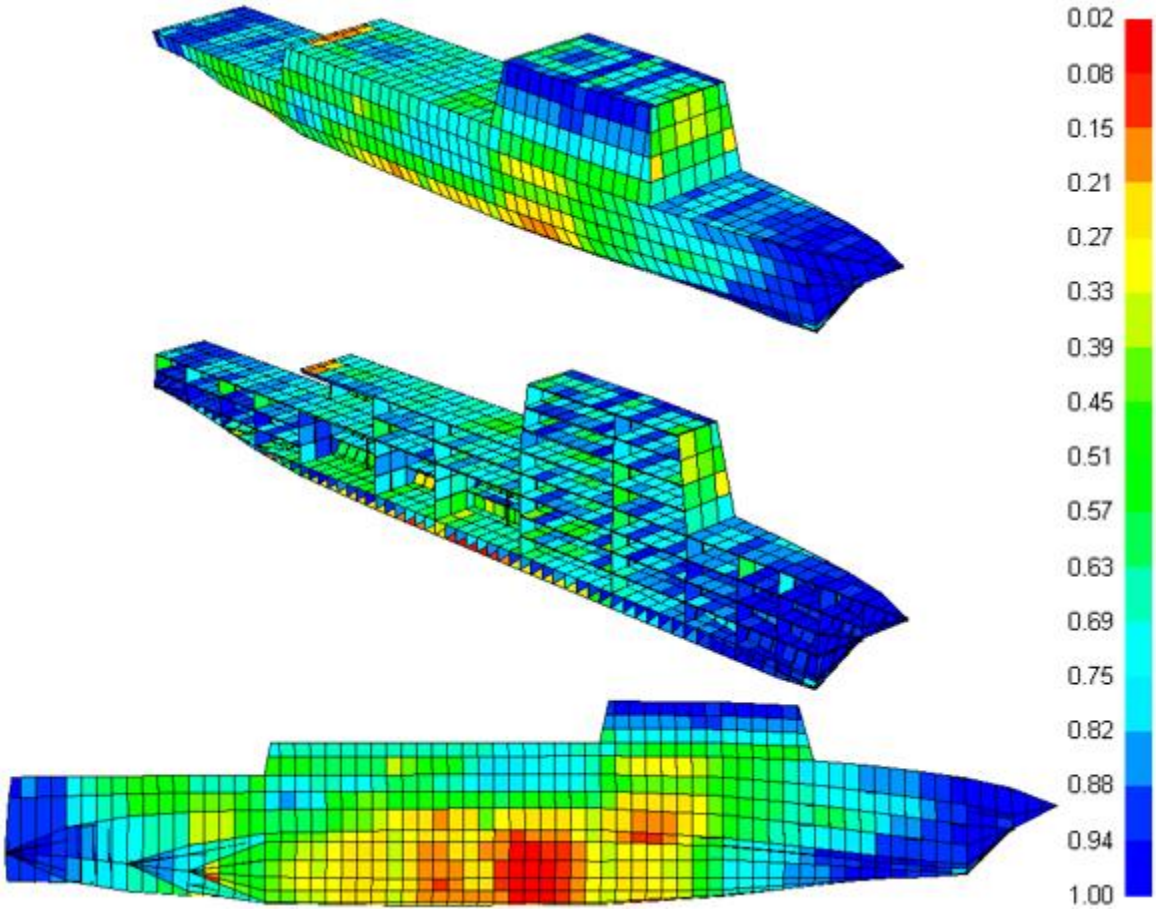

Figure 50 – Adequacy of DDG Structure, Hogging Design Wave

The deformation of the hull girder under the sagging design wave loading, magnified by 130 to allow for better visualization of the deflected shape, is shown in Figure 51. The response of the structure in terms of the MAESTRO adequacy of each element for this loading condition is shown in Figure 52. All elements are adequate, though several small groups of elements are close to being inadequate. These areas of low adequacy are located near the forward and aft bottom edges of the deckhouse, forward of the deckhouse just below the waterline, and along the bottom of the ship just forward of the stern. The transverse bulkhead below the hangar entrance also has a low value of adequacy.

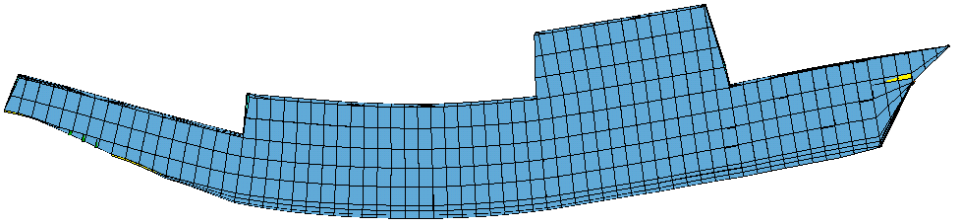

Figure 51 – DDG Hull Girder Deformation, Design Sagging Wave

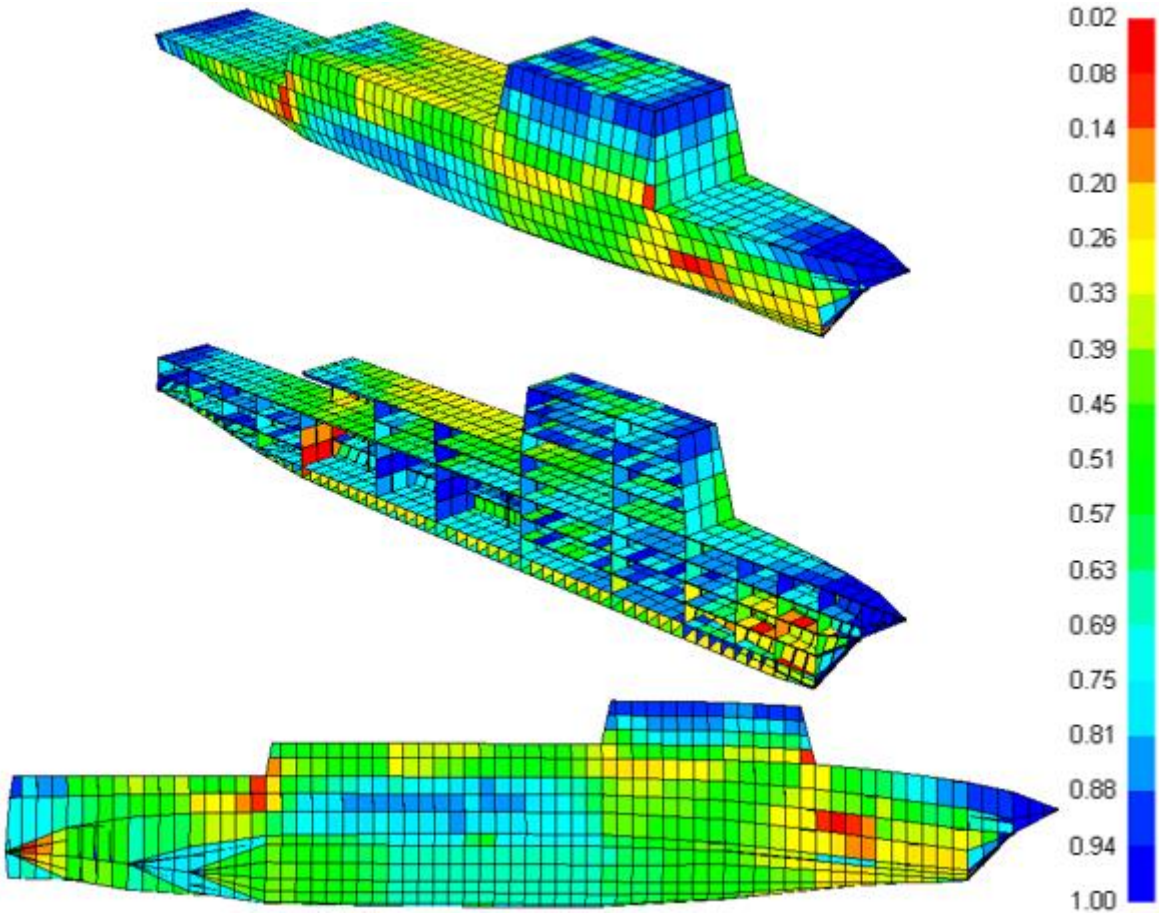

Figure 52 – Adequacy of DDG Structure, Sagging Design Wave

The views shown in Figure 50 and Figure 52, from top to bottom, are perspective, inboard profile perspective, and under keel. These views provide a nearly complete overview of the ship structure, showing the entirety of the hull plating of the starboard side and the majority of internal structure, including the decks and transverse bulkheads, of the port side. Due to the port-starboard symmetry of the vessel, the response of the starboard side structure in the views is also reflective of the port side response and vice versa. These views are used for all figures showing the response of the ship structure to whipping loads throughout this and subsequent chapters.

3.2 MAESTRO UNDEX Assessment Setup and Methodology

The process of preparing and performing an UNDEX-induced whipping analysis for the MAESTRO ship model using the VT whipping model described in chapter 2 is presented. A method of applying the results of the whipping analysis to the ship model in MAESTRO is also described. In addition, the availability of the necessary ship characteristic data within MAESTRO and its applicability and limitations for use in the VT whipping model are discussed. Methods are presented for the analysis of both the local (stiffened panel) and global (ALPS/HULL) ship structure.

3.2.1 ALPS/ULSAP Stiffened Panel Analysis

3.2.1.1 Extraction of Ship Characteristic Data from MAESTRO Model

In order to properly represent the ship as a series of equally-spaced lumped masses in the VT whipping model, several characteristics are extracted from MAESTRO. The general ship characteristics that are needed include the overall ship length, draft forward, and draft aft. The necessary characteristics for each of the lumped masses are the weight (w), buoyancy (m_b), added mass in the vertical direction (m_w), buoyant force per unit immersion (k), and location relative to the bow (x). The required beam properties, which are to reflect the cross-section at the midpoint between two lumped masses, include moment of inertia about the transverse axis (I_{zz}), shear area (A_s), and neutral axis height (h_{NA}). All weight terms have units of kilograms, while kilograms per meter (kg/m) are used for buoyant force per unit immersion. All length and length-derived terms have units of meters.

The draft forward and aft are output as part of the hydrostatic balance calculation ("Model" menu, "Balance…" submenu). The results of the balance calculations are shown in Figure 53, with the drafts highlighted. The model should be restrained and experiencing only still water loading to ensure the correct drafts are output.

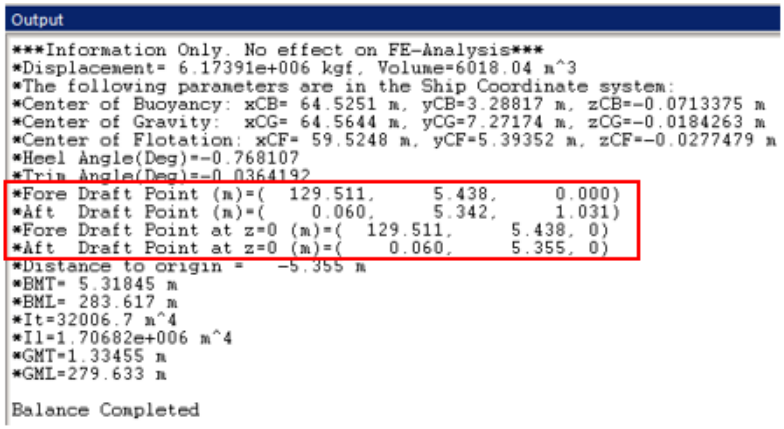

Figure 53 – MAESTRO Balance Results

The lumped mass and beam characteristics can be obtained from the "Hull" menu in MAESTRO. The characteristics of the ship are automatically lumped into values at each station, of which there are 21 for this ship model. The weight and buoyancy at each lumped mass can be copied from the output window for the "View Gross Weight" and "View Buoyancy" options, respectively. These outputs are shown in Figure 54 and Figure 55. There is not a simple option to output lumped values for buoyant force per unit immersion in MAESTRO, so it is estimated using the lumped buoyancy and the draft assuming a box-shaped section. The location of each station, which is the location of each lumped mass, is included in these outputs. The distance between each lumped mass is calculated from this information as the difference between two station locations. The overall length (*LOA*) is equal to the longitudinal position of the twenty-first station.

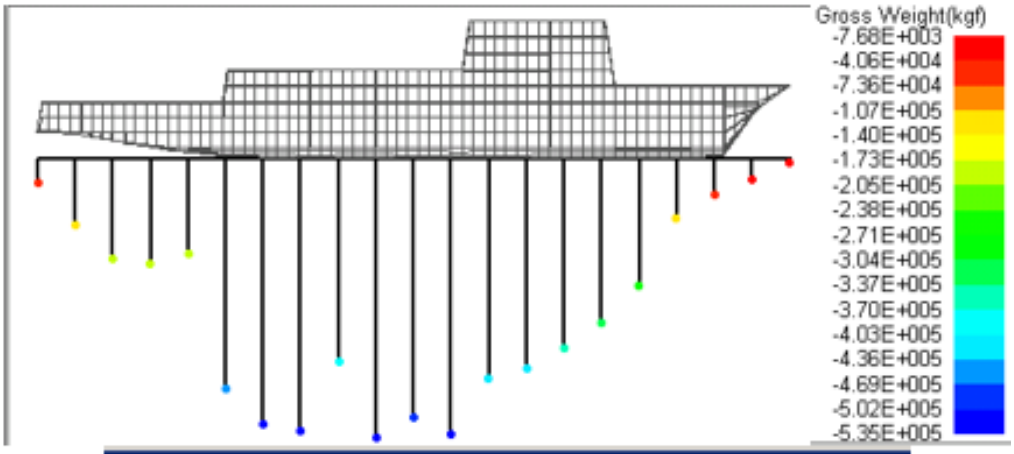

Output

Gross Vertical Force, excluding End shear and Buoyancy
Load Case =1, "Full Load Hogging"

Station	X(m)	Weight(kgf)
0	0	-48210.6
1	6.9	-128340
2	13.8	-193504
3	20.7	-201773
4	27.6	-184360
5	34.5	-443078
6	41.4	-510365
7	48.3	-522300
8	55.2	-390748
9	62.1	-535134
10	69	-496763
11	75.9	-530280
12	82.8	-422679
13	89.7	-404626
14	96.6	-364602
15	103.5	-316229
16	110.4	-244166
17	117.3	-115187
18	124.2	-69258.2
19	131.1	-39344.8
20	138	-7677.98

Total Force(Full Ship)=-6.16863e+006(kgf)=-6.16863e+006(kg)

Figure 54 – MAESTRO Gross Weight Output

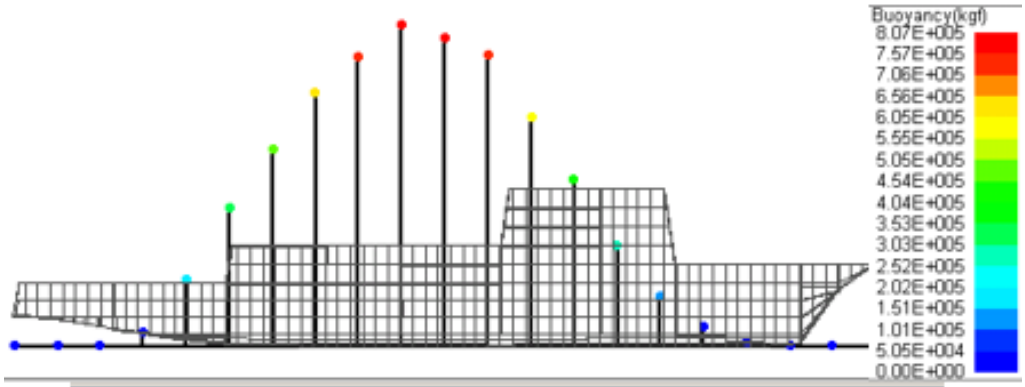

Output

Vertical Force due to Buoyancy
Load Case =1, "Full Load Hogging"

Station	X(m)	Force(kgf)
0	0	0
1	6.9	0
2	13.8	355.144
3	20.7	34023.4
4	27.6	166660
5	34.5	346735
6	41.4	496035
7	48.3	640075
8	55.2	729865
9	62.1	807332
10	69	777468
11	75.9	735330
12	82.8	575026
13	89.7	417522
14	96.6	253208
15	103.5	126247
16	110.4	48731.8
17	117.3	12692.2
18	124.2	1618.93
19	131.1	10.9681
20	138	0

Total Force(Full Ship)=6.16893e+006(kgf)=6.16893e+006(kg)

Figure 55 – MAESTRO Buoyancy Output

A table of structural properties at each station is output when “Properties” is selected from the “View Longitudinal” submenu of the “Hull” menu, which is shown in Figure 56. The values of each property in this table include any contributions from the deckhouse and hangar. This table includes moment of inertia (“Izz(V)”), shear area (“AreaY”), and neutral axis height (“Neutral Axis Y”) at each station. The values of Young’s modulus and Poisson’s ratio are set to 204 GigaPascals (GPa) and 0.3, respectively, which reflect the properties of the steel used in the model. These can be found by selecting “Materials…” from the “Model” menu.

Output

	Section	xLoc(m)	Status	Izz(V)(m^4)	Iyy(H)(m^4)	J(m^4)	Iww(m^6)	Area(m^2)	AreaZ(m^2)	AreaY(m^2)	Neutral Axis Z(m)	Neutral Axis Y(m)
1	0	0	OK	9.55424e-006	0.000321731	9.01794e-005	2.25878e-008	0.0339372	0.0322718	0.0119016	0.0001768	5.03565
2	1	6.9	OK	4.27547	23.1137	8.67022	5.36679	0.890168	0.803773	0.18516	5.59294e-016	7.51928
3	2	13.8	OK	5.48528	23.922	10.4633	2.21066	0.89764	0.804266	0.182356	0.0129095	7.12812
4	3	20.7	OK	9.28397	27.7026	15.075	1.2042	1.07568	0.968657	0.22343	-0.00662248	6.26323
5	4	27.6	OK	13.5526	34.9446	19.954	8.58708	1.29064	1.12949	0.31425	-0.0140342	5.7967
6	5	34.5	OK	17.5175	42.3373	19.0177	481.878	1.05071	0.72957	0.432374	-5.38225e-016	6.0616
7	6	41.4	OK	42.3443	55.8312	53.6632	36.0434	1.38312	0.989533	0.527005	-1.88132e-018	8.30658
8	7	48.3	OK	43.0856	56.4768	54.3374	36.1489	1.39506	0.994373	0.534246	3.7926e-017	8.2408
9	8	55.2	OK	46.137	55.8608	51.0476	77.7606	1.52459	1.1869	0.463193	-0.0042668	8.24545
10	9	62.1	OK	46.807	59.4723	54.7042	60.1652	1.57135	1.17587	0.520241	9.823e-008	8.22178
11	10	69	OK	47.18	59.43	54.7616	61.6564	1.57554	1.17431	0.526064	1.05598e-007	8.195
12	11	75.9	OK	47.4123	59.2836	54.814	62.9596	1.5764	1.17273	0.528438	1.13165e-007	8.18204
13	12	82.8	OK	138.81	77.9448	92.4652	1130.02	2.41692	1.92618	0.678683	1.19647e-015	11.75
14	13	89.7	OK	133.336	71.9343	87.5785	1033.38	2.34021	1.86488	0.674827	-5.68183e-016	11.9263
15	14	96.6	OK	114.456	56.9923	75.3902	746.759	1.9924	1.566	0.621463	-0.00516547	11.9637
16	15	103.5	OK	103.27	45.9909	62.948	577.925	1.84196	1.42444	0.622154	-0.00130497	12.3318
17	16	110.4	OK	18.1313	15.0744	13.0489	19.6575	0.967964	0.754853	0.382275	-0.0214623	7.20169
18	17	117.3	OK	12.7581	7.82453	7.1799	10.1117	0.719323	0.521715	0.335612	3.24361e-016	7.39976
19	18	124.2	OK	9.68983	3.76498	3.51558	3.73228	0.576677	0.368441	0.323116	-0.000510187	7.65506
20	19	131.1	OK	1.04396	0.965889	0.655991	0.0757659	0.290478	0.216633	0.155876	0.0840031	10.9661
21	20	138	OK	9.78086e-009	5.75648e-009	8.12789e-008	3.23121e-014	0.00321614	0.00304739	0.00303194	4.11515e-021	13.2135

Figure 56 – MAESTRO Longitudinal Properties Table

An option to output a lumped added mass at each station is not available in MAESTRO. However, added mass values for each wetted panel in all six degrees of freedom is output during the processing of a natural frequency analysis. The added mass values in the y-direction are all that are needed. In order to obtain a lumped value at each mass, these individual element values are summed if they fall within the longitudinal range of the lumped mass. For example, station 2 is located a longitudinal distance of 6.9 meters from the stern and station 3 is located 13.8 meters from the stern. The added mass for station 2 is the sum of the elemental added masses for elements with a position between 3.45 meters and 10.35 meters, and the added mass for station 3 is the sum of the elemental added masses for elements with a position between 10.35 meters and 17.25 meters. However, each panel has a length of two meters, meaning that many panels are partially in the ranges for two lumped masses. To allow for a simpler calculation of the lumped value, the upper and lower boundary of the ranges are rounded to the nearest multiple of two. For example, the longitudinal limits for the added mass calculation at station 2 are 4.0 meters and 10 meters, while the limits for station 3 are 10 meters and 18 meters. At this point, all of the necessary data has been extracted from MAESTRO. A table listing the properties of the lumped mass representation as they are entered into the VT whipping model is given in Appendix B.

3.2.1.2 Lumped Mass Representation

The shear area and moments of inertia of the most forward and aft stations are very close to zero. For this reason, the structural characteristics of these stations are excluded from the lumped mass representation of the ship. The ship is modeled as a series of 20 lumped masses connected by 19 weightless beams.

To consolidate the mass, buoyancy, and added mass from the given 21 stations to the necessary 20 lumped masses, the value of each property at each station is averaged with the one forward of it. For example, the mass at station 2 is averaged with the mass at station 3 to calculate the mass at the second new lumped mass location. Using this representation, half of the property value of the most forward and aft station is not included in the representation. To avoid this, the previously excluded amount is added to the most forward and aft lumped masses for each property. For example, the mass at the first new lumped mass location is calculated as the sum of the entire mass at the station 1 plus half the mass at station 2. Also, the mass at the twentieth new lumped mass location is calculated as the sum of half the mass at station 20 and the entire mass at station 21. The positions of the 20 lumped masses are the midpoints between the original stations.

No adjustment or change of position is required for the properties of the 19 weightless beams. No adjustment is necessary to the values of section inertia or neutral axis height output by MAESTRO to obtain a reasonable representation of the ship, but an adjustment is required to the shear area.

In MAESTRO, the shear areas are calculated as the vertical projection of the material cross-section area [59]. When these values were used to calculate the natural frequencies of the hull girder, the resulting frequencies were too high. Hicks experienced a similar problem while performing frequency calculations. He noted that the beam theory method of calculating shear area:

$$A_s = \frac{It}{m} \tag{126}$$

where t is plate thickness at the neutral axis, I is the moment of inertia, and m is the first area moment of area above neutral axis of the cross section, lead to much better frequency results [20]. On average, this shear area formulation calculated values that were approximately half of the vertical projection method [20]. To account for this difference, the shear areas used in the lumped mass representation, $A_{s,adj}$, are equal to the shear areas output by MAESTRO divided by a shear area adjustment factor, $c_{s,adj}$:

$$A_{s,adj} = \frac{A_s}{c_{s,adj}} \tag{127}$$

The shear area adjustment factor will vary as different ship models are used. It is selected so that the frequencies of the lumped mass representation calculated by the VT whipping model are as close as possible to those calculated by the natural frequency analysis in MAESTRO. For the DDG model, a shear area adjustment factor of 2.75 is found to produce a model with the best agreement, and is used in all analyses that utilize this ship model.

3.2.1.3 Vibration and Whipping Analysis

After successfully entering the characteristics of the lumped mass representation of the ship into the VT whipping model, the mode shapes and natural vibration frequencies are calculated. These properties are compared to those calculated by the natural frequency analysis in MAESTRO. The two sets of calculated natural frequencies are listed in Table 18. There is strong agreement between the two sets of frequencies, specifically for the third and fourth modes. The third, fourth, and fifth mode shapes calculated by the VT whipping model and MAESTRO are shown in Figure 57, Figure 58, and Figure 59, respectively. The deflections in each of the figures are increased in scale as a visual aide. Again, there is strong agreement between the two calculations. It was difficult to identify the sixth vertical vibration mode from the MAESTRO natural frequency calculations due to the noise from other degrees of freedom present in the higher frequency mode shapes. For this reason, no comparison for the sixth mode shape was done.

Table 18 – Calculated Natural Frequency Comparison

Mode Shape	VT Model Frequency (Hz)	MAESTRO Frequency (Hz)
3 (2-node)	1.456	1.455
4 (3-node)	2.651	2.665
5 (4-node)	3.789	3.847

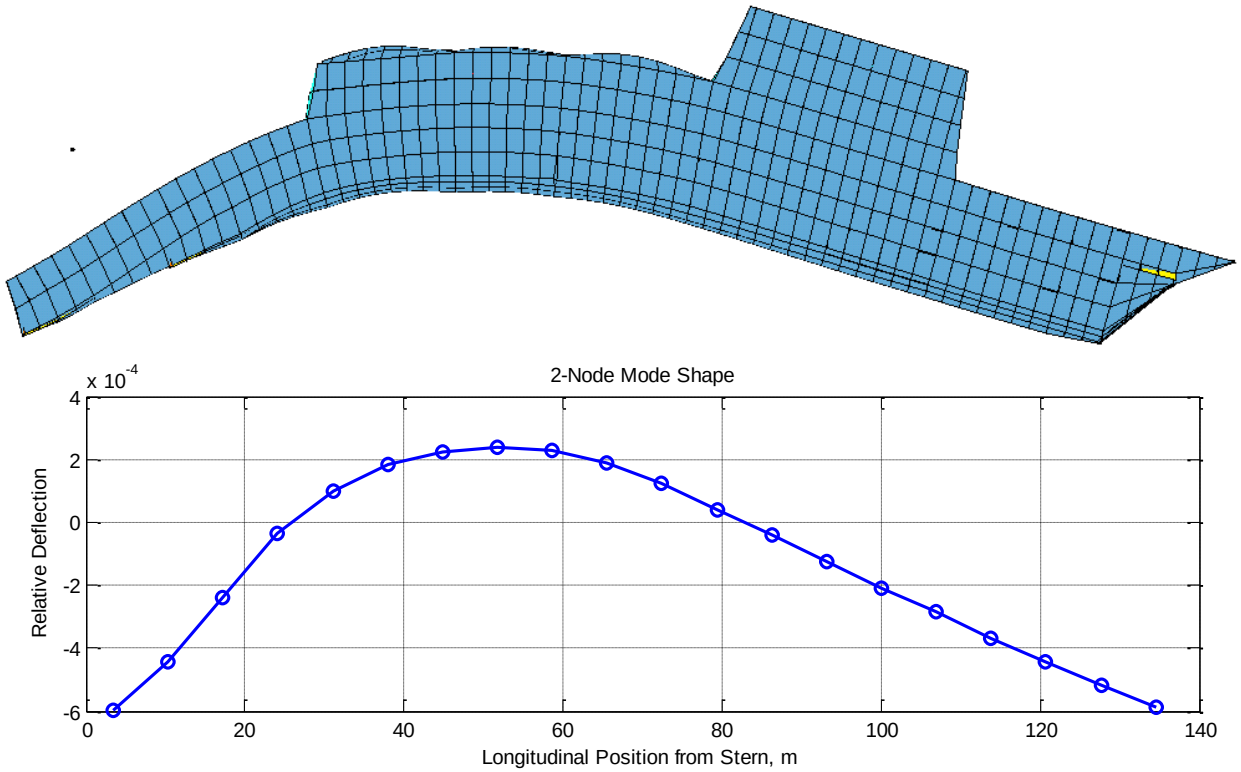

Figure 57 – MAESTRO (top) and VT Whipping Model (bottom) Calculated 2-Node Mode Shapes

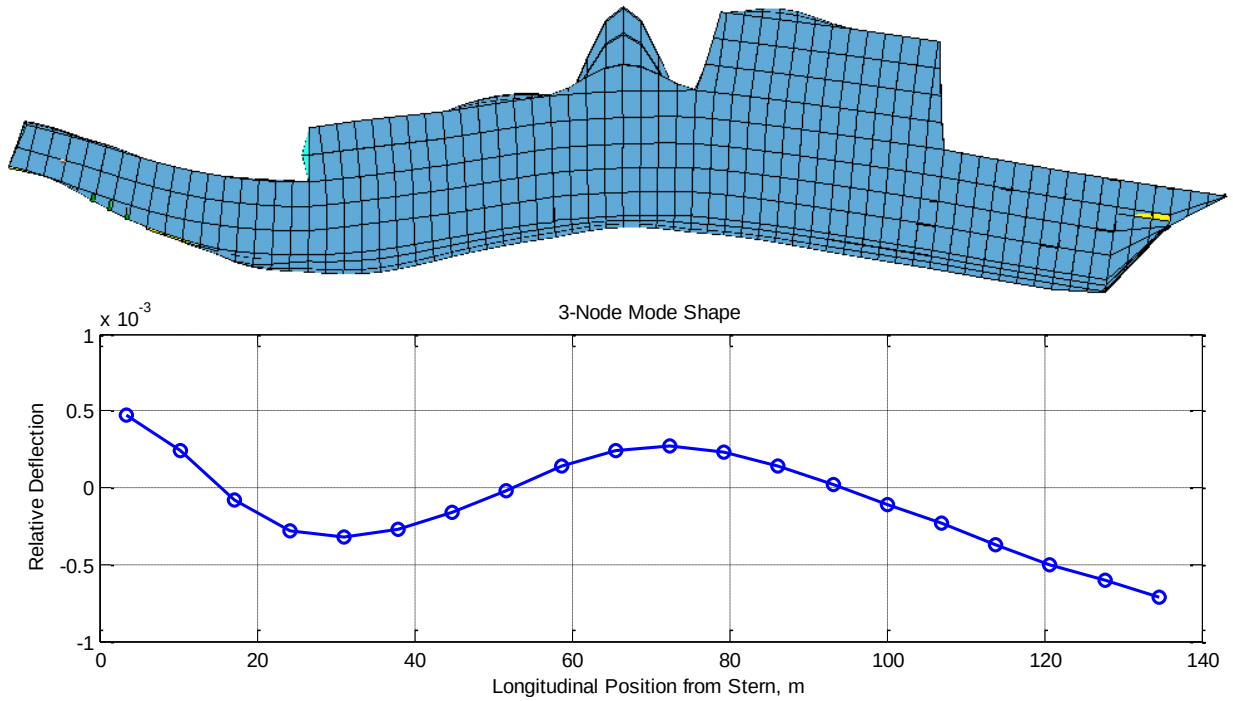

Figure 58 – MAESTRO (top) and VT Whipping Model (bottom) Calculated 3-Node Mode Shapes

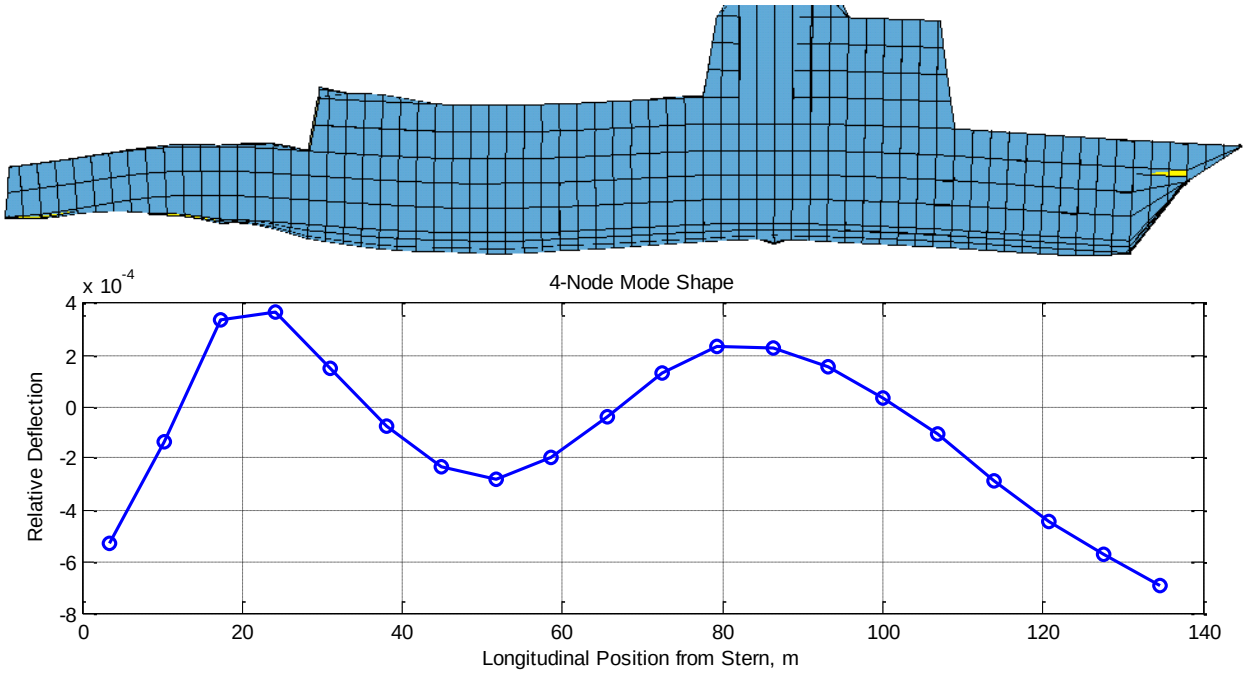

Figure 59 – MAESTRO (top) and VT Whipping Model (bottom) Calculated 4-Node Mode Shapes

Next, bubble forcing is applied to the lumped mass model of the ship in the VT whipping model. The whipping model calculates a deflection and bending moment time history at each beam midpoint for the entire simulation time. The whipping design load cases are defined by the deflections at the moments in time that the largest magnitude bending moments occur. Whipping design load cases are defined for both hogging and sagging, which correspond to the largest magnitude negative and positive bending moments, respectively. For both design load cases, the VT whipping model outputs the shape of the ship, the values of the deflections at each beam midpoint, and the maximum magnitude bending moment.

3.2.1.4 Application of Whipping Results in MAESTRO

In order to analyze the behavior and strength of the ship structure under whipping loads, the MAESTRO ship model is bent into the deflection shapes for the design load cases. Forced displacement restraints in MAESTRO are used to do this. These restraints allow the user to set the position of a group, module, or other collection of nodes a desired distance away from its original location. To simplify the application of these displacements, a series of nodal groups are created using all nodes at the transverse bulkhead (TBHD) locations. The locations of the nodal groups along the ship are shown in Figure 60. A body plan view of a cross-section forward of midship showing the location of each node included in the group is given in Figure 61. The locations of the

THBD's do not coincide with the output locations from the VT model. The deflections at the TBHD's are calculated using a polynomial curve fit of the deflection output from the VT model.

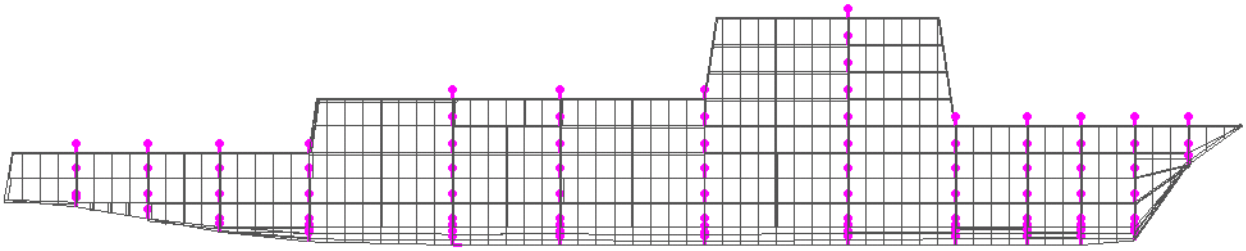

Figure 60 – Locations of Nodal Groups

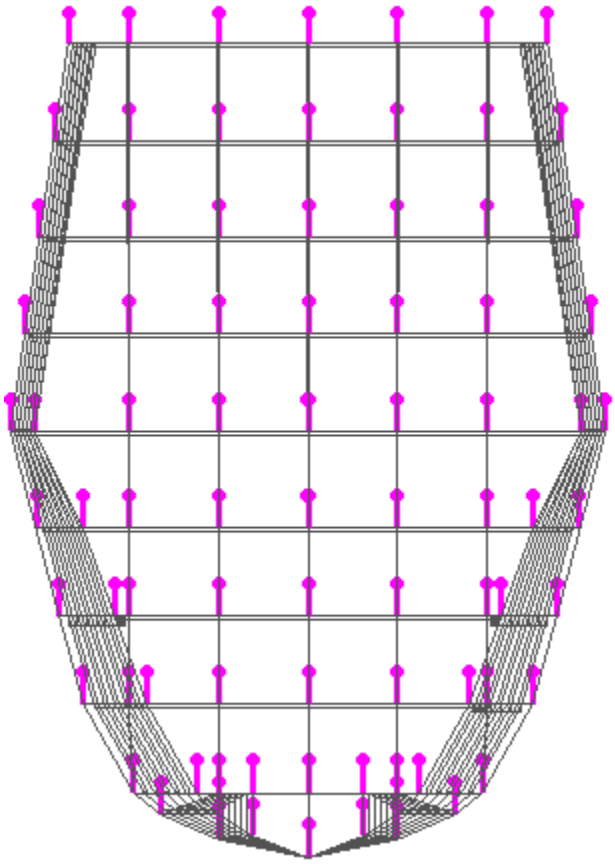

Figure 61 – Body Plan Showing Sample Nodal Group

A forced displacement restraint in the vertical direction is applied to each nodal group. A separate load case is created for both the hogging and sagging cases, with the ship experiencing only still water conditions in addition to the loading due to whipping. After MAESTRO analyzes the global and local structural response to the design load cases, the stresses acting throughout the ship and the adequacy of each panel are investigated to determine if the structure is capable of withstanding the loading due to whipping.

3.2.2 ALPS/HULL Hull Girder Collapse Analysis

3.2.2.1 Model Creation and Analysis Setup

For the ALPS/HULL analysis, a one-bay model of a section of the ship is created. This section is created by making a general group of all quad elements in the bay. The section is then refined for an ALPS/HULL analysis, which is done by right-clicking on the group in the "Groups" tab in the "Parts Tree" and selecting the "Refine" option. The refined section is shown in Figure 62. The section was created between 48 meters and 50 meters forward of the stern, as shown in Figure 63. This position is near the location where the largest magnitude bending moment is expected to occur based on the vibration mode shapes of the hull, which are discussed in section 3.2.1.3.

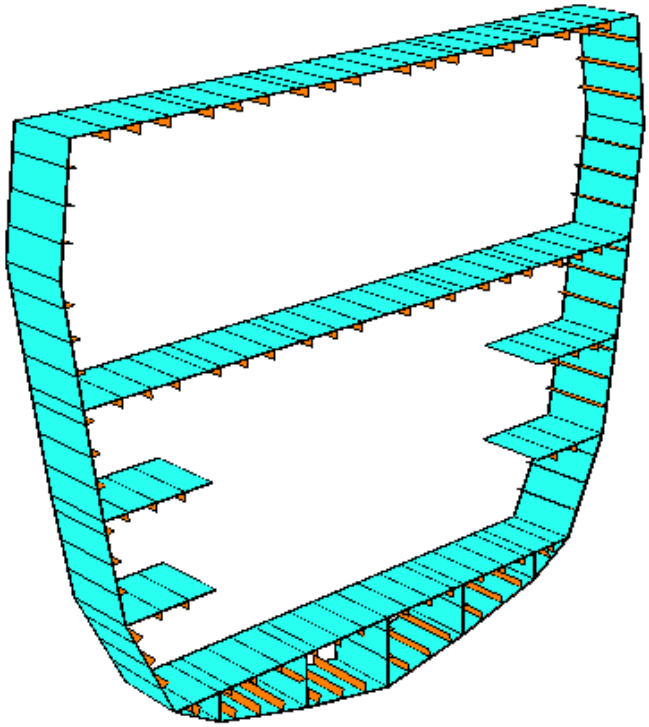

Figure 62 – ALPS/HULL Analysis One-Bay Section Model

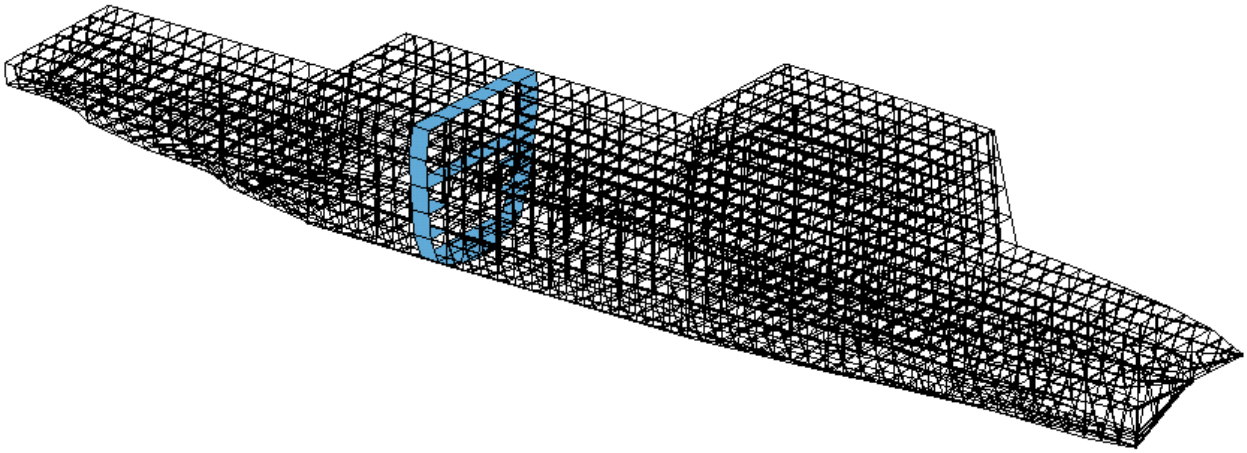

Figure 63 – Longitudinal Location of ALPS/HULL Model

The refined model is now available under the "finemesh" folder in the "Parts" tab in the "Parts Tree." The ALPS/HULL analysis can be performed by selecting the refined model in the "Parts Tree" and selecting the "Hull Girder Collapse" option under the "Analyze" menu. From this menu, the type of loading (hogging or sagging), number of loading steps, and the vertical rotation increment are chosen. The number of loading steps and the vertical rotation increment are chosen to ensure the section is loaded beyond its ultimate strength bending moment. All other input options are kept as their default values. A sample analysis setup is shown in Figure 64. After the analysis is complete, the condition and the calculated vertical bending moment of the section can be viewed by right-clicking in the "Modeling Space." The step with the maximum bending moment is noted with "MomMax." The value of "MomMax" is the ultimate strength bending moment for the section in the chosen load type. This value will vary slightly based on the chosen vertical rotation increment.

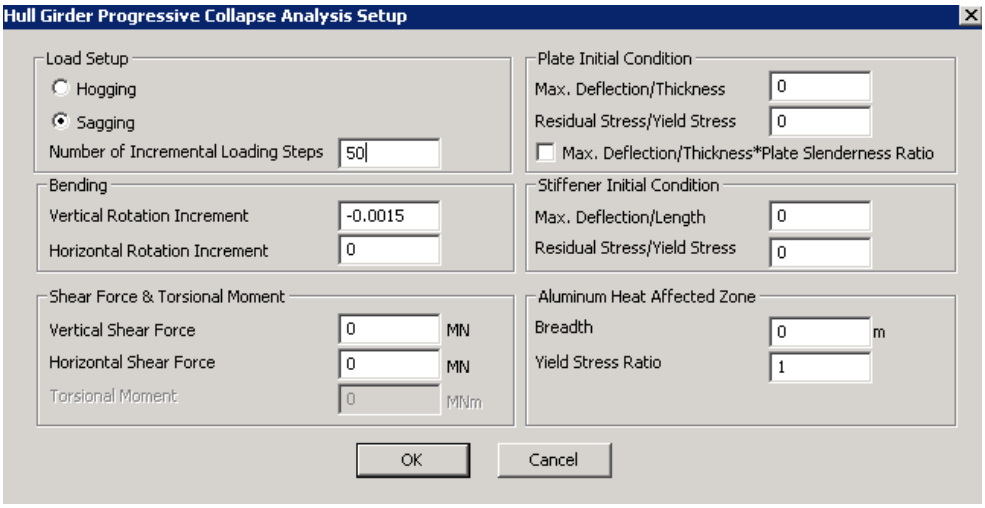

Figure 64 – ALPS/HULL Analysis Setup Menu

For the hull girder collapse analysis, the hull girder is considered to have failed if the magnitude of the most severe bending moment caused by the whipping loading is greater than the ultimate strength maximum bending moment predicted by ALPS/HULL. For hogging, the magnitude of ultimate strength bending moment is 1,172 MN-m and the failure modes of the structure under this bending moment are shown in Figure 65. For sagging, the ultimate strength bending moment is 1,617 MN-m and the failure modes of the structure under this bending moment are shown in Figure 66. If the ship is loaded in a manner that produces a bending moment greater than the ultimate strength bending moment, the failure modes will progress through the entire section. An example of total section failure from an extreme sagging load case is shown in Figure 67. The failure mode acronyms are given in Table 17.

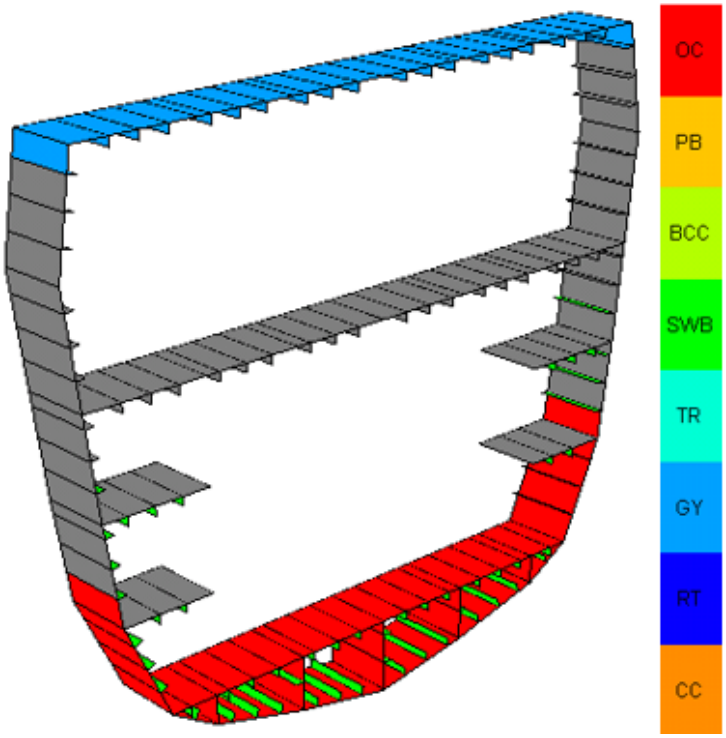

Figure 65 – ALPS/HULL Failure Modes at Ultimate Strength Hogging Bending Moment

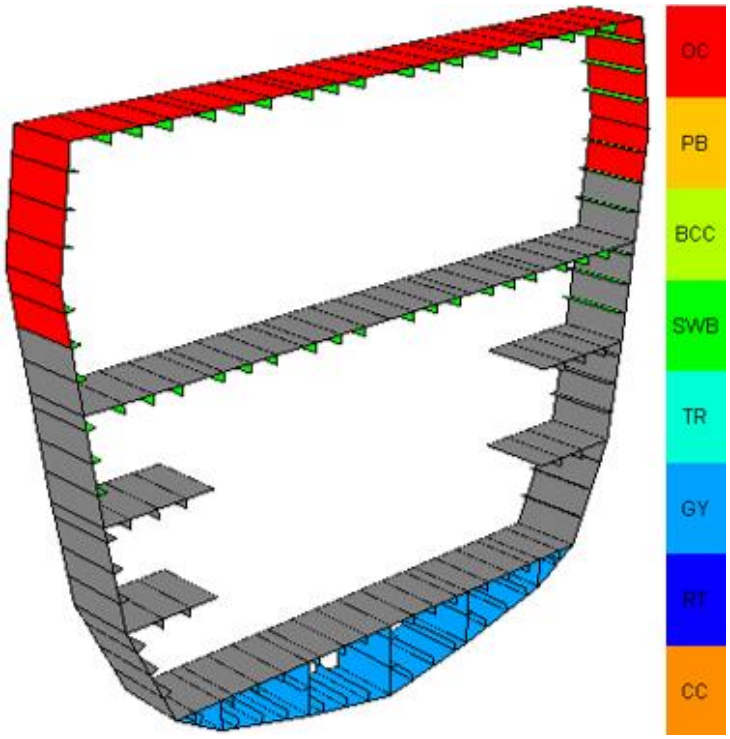

Figure 66 – ALPS/HULL Failure Modes at Ultimate Strength Sagging Bending Moment

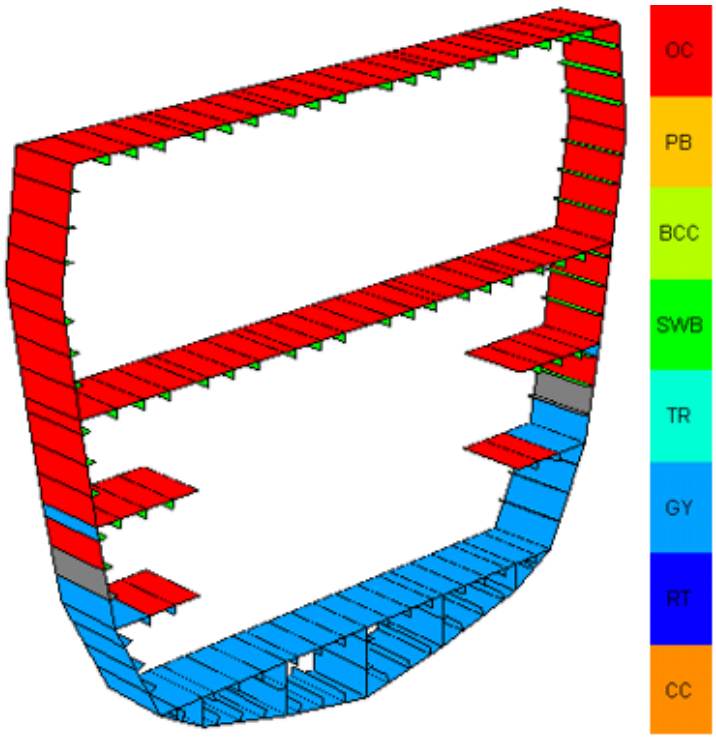

Figure 67 – ALPS/HULL Failure Modes at Total Section Failure due to Extreme Sagging

3.2.2.2 Application of Whipping Loads

The bending moment distributions of the ship for the whipping design load cases are calculated to determine if the hull girder will collapse. This distribution is not calculated directly as a result of the imposed deflections. However, the restraints are transformed into a load vector acting on the finite element model during the FEA calculation [59]. This load vector is output to the output window as a series of nodal reaction forces during the FEA, including a sum of the forces acting on the nodes in each nodal group with a forced displacement restraint (i.e. at each TBHD location). The values of these summed forces are then manually added to the load case as point forces acting on the nodal groups at the TBHDs. This is done using the "Point Force" tab in the "Create/Modify…" tool under the "Loads" menu, as shown in Figure 68. Point forces are included in the hull girder load calculations, but do not affect the FEA results.

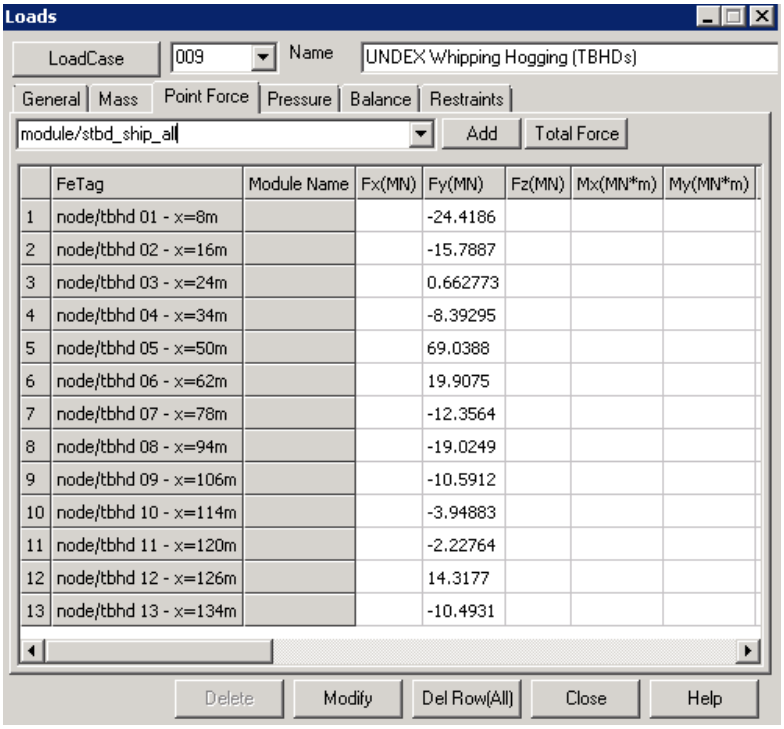

	FeTag	Module Name	Fx(MN)	Fy(MN)	Fz(MN)	Mx(MN*m)	My(MN*m)
1	node/tbhd 01 - x=8m			-24.4186			
2	node/tbhd 02 - x=16m			-15.7887			
3	node/tbhd 03 - x=24m			0.662773			
4	node/tbhd 04 - x=34m			-8.39295			
5	node/tbhd 05 - x=50m			69.0388			
6	node/tbhd 06 - x=62m			19.9075			
7	node/tbhd 07 - x=78m			-12.3564			
8	node/tbhd 08 - x=94m			-19.0249			
9	node/tbhd 09 - x=106m			-10.5912			
10	node/tbhd 10 - x=114m			-3.94883			
11	node/tbhd 11 - x=120m			-2.22764			
12	node/tbhd 12 - x=126m			14.3177			
13	node/tbhd 13 - x=134m			-10.4931			

Figure 68 – Addition of Point Forces to Load Case

The hull girder bending moment distribution for the design load cases can now be viewed by selecting "Bending Moment" from the "View Longitudinal" submenu of the "Hull" menu. The values of the bending moment at each station location are also output to the output window. The maximum magnitude bending moment calculated by the hull girder analysis for the load case is compared to the corresponding ultimate strength bending moment predicted by ALPS/HULL to determine if the hull will collapse. The bending moment outputs for the rigid body ship are shown

in Figure 69. A maximum magnitude bending moment of 36.08 MN-m occurs at station 8, which is 55.2 meters forward of the stern.

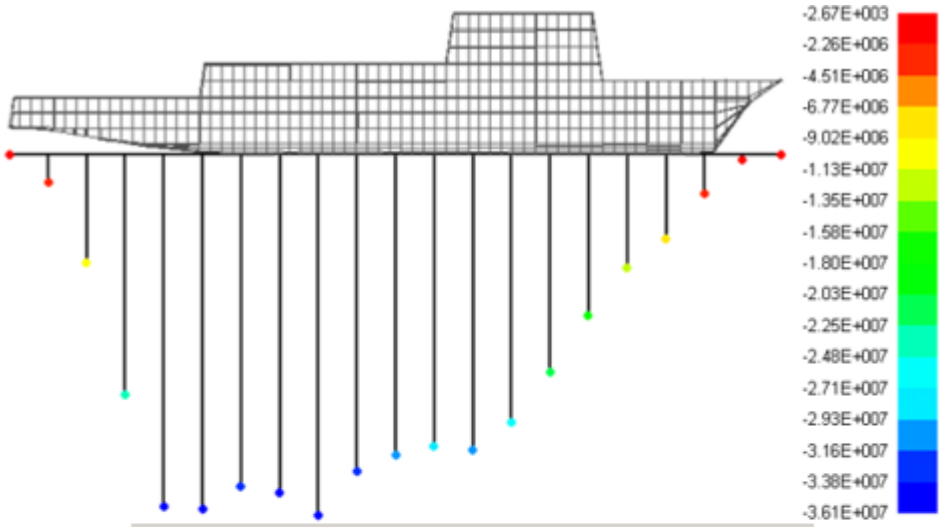

Output

Station	X(m)	Bending Moment(MN*m)
0	0	-0.00267302
1	6.9	-2.77286
2	13.8	-10.8052
3	20.7	-24.0961
4	27.6	-35.3073
5	34.5	-35.4728
6	41.4	-33.2875
7	48.3	-33.8345
8	55.2	-36.075
9	62.1	-31.7646
10	69	-30.1199
11	75.9	-29.1868
12	82.8	-29.5717
13	89.7	-26.8775
14	96.6	-21.8371
15	103.5	-16.1743
16	110.4	-11.2936
17	117.3	-8.45692
18	124.2	-3.9615
19	131.1	-0.53273
20	138	-0.0145405

Maximum Bending Moment(Full Ship) in Structural Coordinates:
M=-36.075(MNm)

Figure 69 – DDG Rigid Body Longitudinal Bending Moment Output

3.3 Case Study Results and Assessment

The whipping response of the DDG structure to bubble loading representing the detonation of a MK-48 torpedo with a charge equivalent to 544 kilograms of TNT at a depth of 35 meters is presented in this section. This charge depth is chosen so that the bubble oscillation frequency is close to the third mode natural vibration frequency of the ship and the bubble is allowed to complete three full oscillations and emit three pressure pulses without migrating close to the ship. The charge is located directly under the centerline of the ship at a distance of 48.3 meters from the stern. This position is the charge location that is most likely to excite the ship in its third vibration mode based on the mode shape. The bubble periods and peak fluid accelerations at the surface

directly above the charge for each oscillation are given in Table 19. The bubble radius and migration time histories for this explosion are shown in Figure 70 and Figure 71, respectively. The fluid accelerations at the surface directly above the charge are shown in Figure 72.

Table 19 – Case Study Bubble Characteristics

Oscillation	Period (s)	Peak Fluid Acceleration (m/s^2)
1st	0.709	34.84
2nd	0.599	16.71
3rd	0.559	11.50

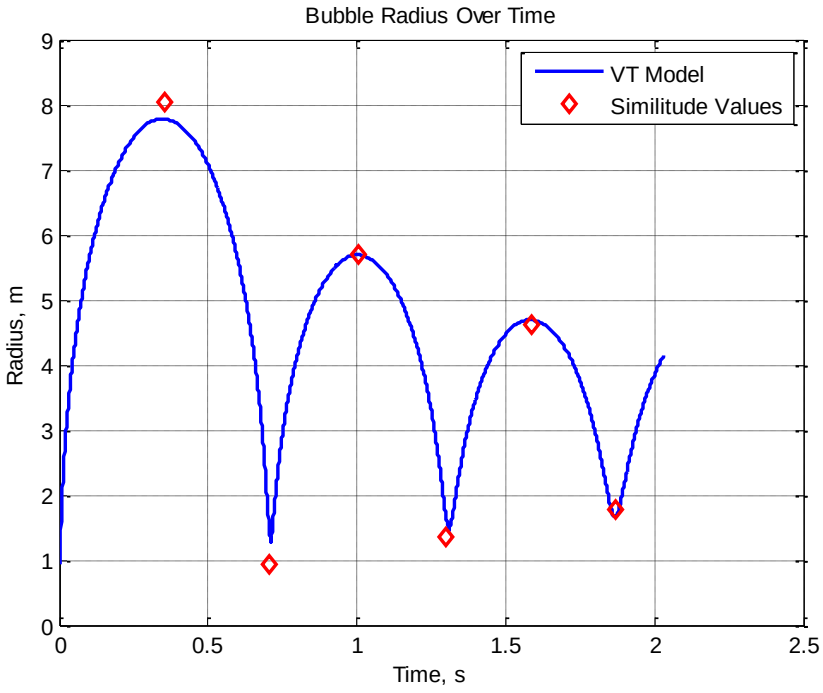

Figure 70 – MK-48 Bubble Radius Time History

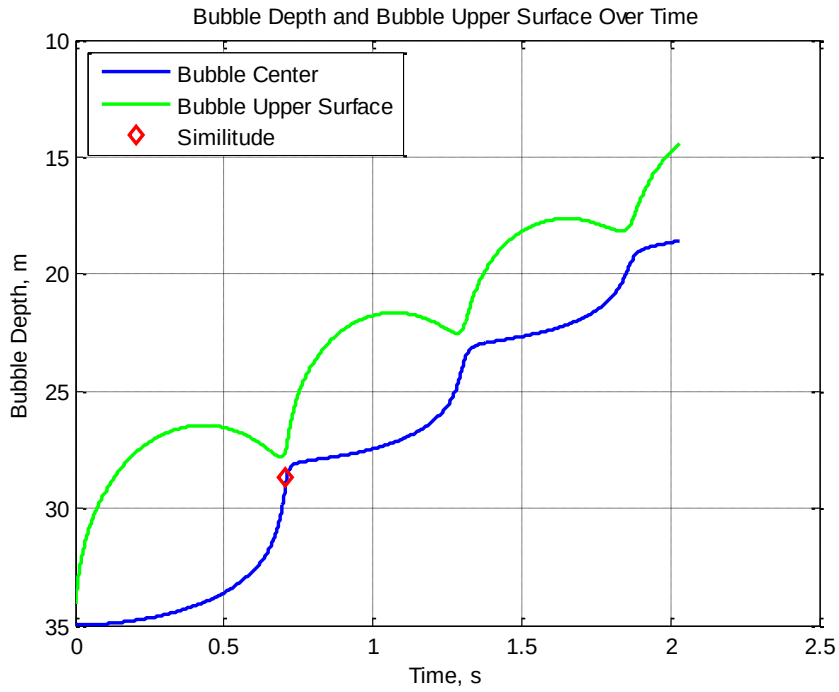

Figure 71 – MK-48 Bubble Migration Time History

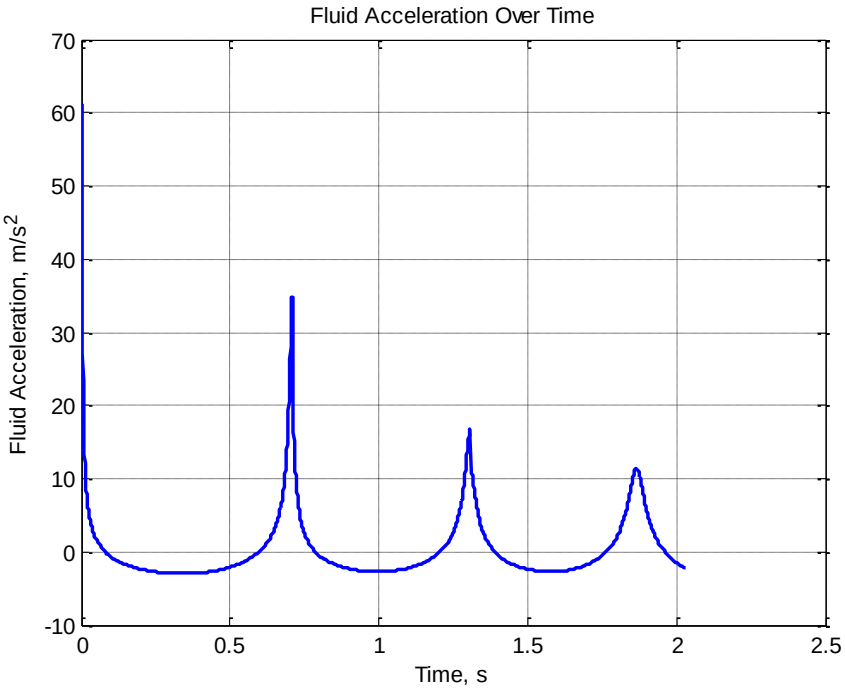

Figure 72 – MK-48 Bubble Pulse Fluid Acceleration Time History

The deformation of the ship caused by the hogging whipping design load case is shown in Figure 73. The deformations are increased to be 35 times larger than their original magnitude as a

visual aide. The shape of the ship under this loading is very similar to that of its third mode shape, Figure 57, indicating that the ship is vibrating primarily in this mode.

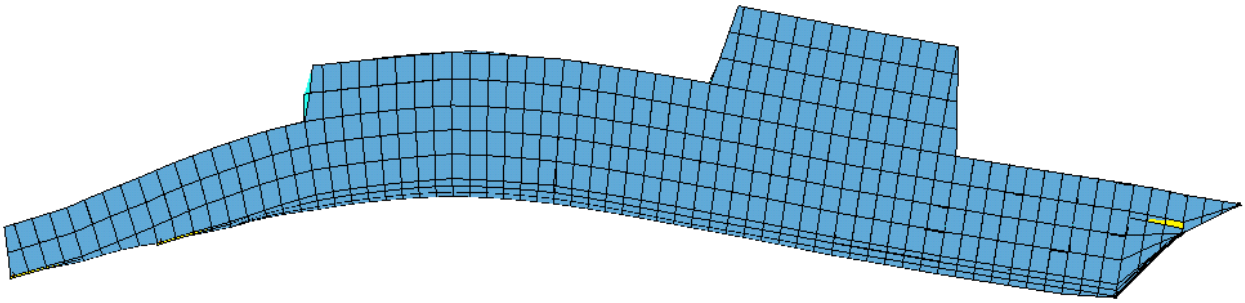

Figure 73 – DDG Deformation, Hogging Whipping Design Load Case

Figure 74 shows the ULSAP adequacy of the DDG structure under this loading condition. According to the color scale, any elements that are a shade of yellow, orange, or red are inadequate in at least one limit state in the loading condition. Many of the elements along the side and keel of the ship near and aft of midship are inadequate. The elements that have failed most severely are grouped along the side of the ship near the flight deck and along the keel below the hangar. This pattern was expected based on the shape of the ship, as there is a large compressive stress along the keel beneath the hangar because of the extreme curvature at this location. Much of the structure in the deckhouse and forward of midship is adequate. This was also expected, as this area of the ship is not experiencing significant curvature. The majority of the internal decks and bulkheads are adequate, with the exception of the top of the innerbottom in the area of extreme curvature.

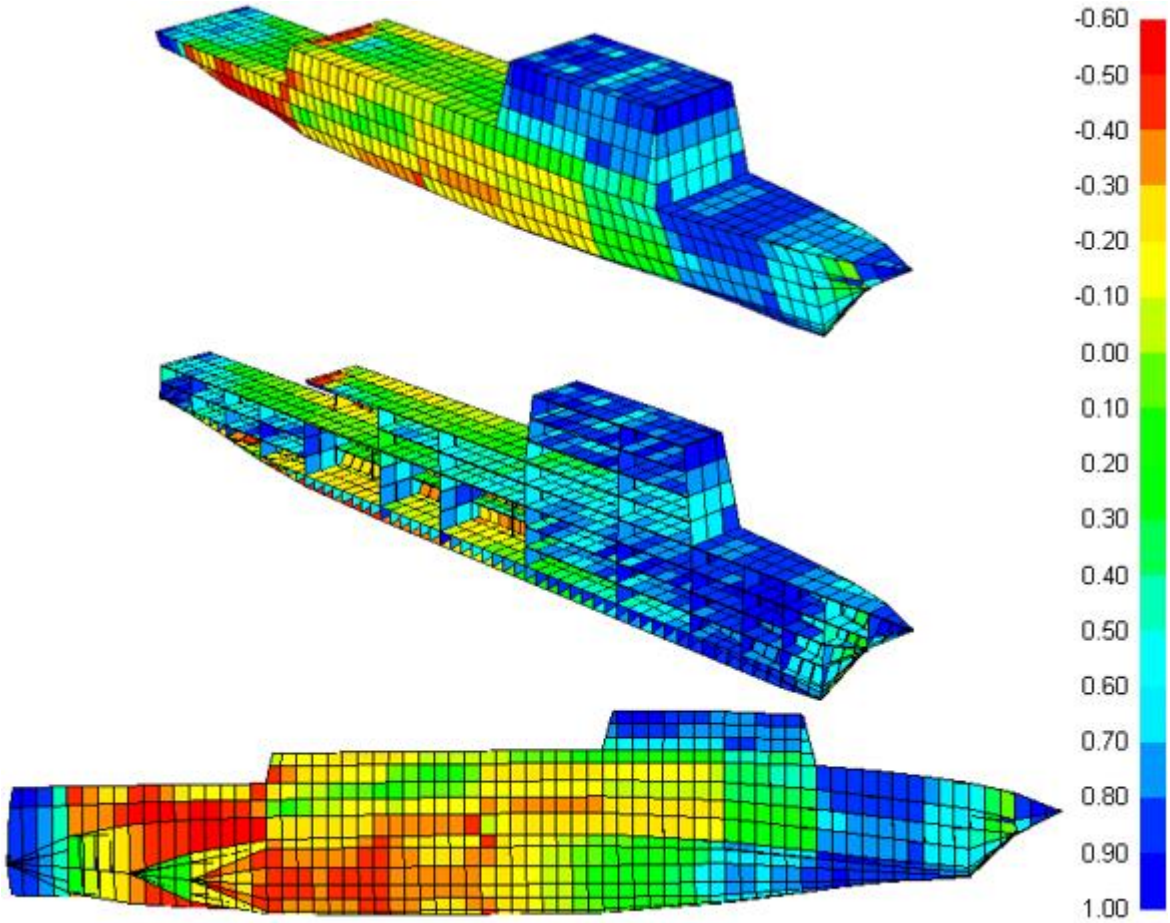

Figure 74 – Adequacy of DDG Structure, Hogging Whipping Design Load Case

The deformation of the ship caused by the sagging whipping design load case is shown in Figure 75. The deformations are increased to be 35 times larger than their original magnitude as a visual aide. The shape of the ship under this loading is very similar to the mirror about the horizontal axis of its third mode shape, Figure 57, indicating that the ship is vibrating primarily in this mode.

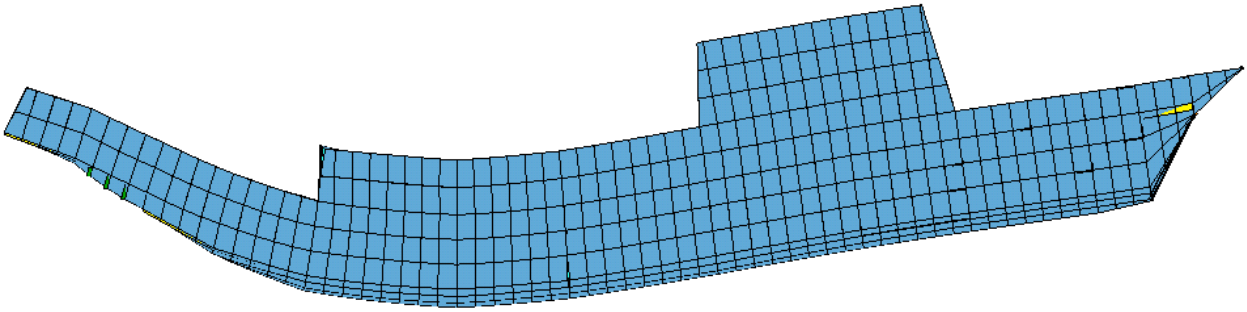

Figure 75 – DDG Deformation, Sagging Whipping Design Load Case

Figure 76 shows the adequacy of the DDG structure under this loading condition. Many of the elements on the ship exterior near and aft of midship are inadequate. The elements that have failed most severely are grouped along the side of the ship near the flight deck and at the edge of the hangar top and side. This pattern was expected based on the shape of the ship, as there is a large compressive stress along the top of hangar and large tension stress along the keel below the hangar and flight deck because of the extreme curvature at these locations. Much of the structure in the deckhouse and forward of midship is adequate. This was also expected, as this area of the ship is not experiencing significant curvature. The majority of the internal decks and bulkheads are adequate, with the exception of the deck inside of the hangar and a few spots on the lower decks in the area of extreme curvature.

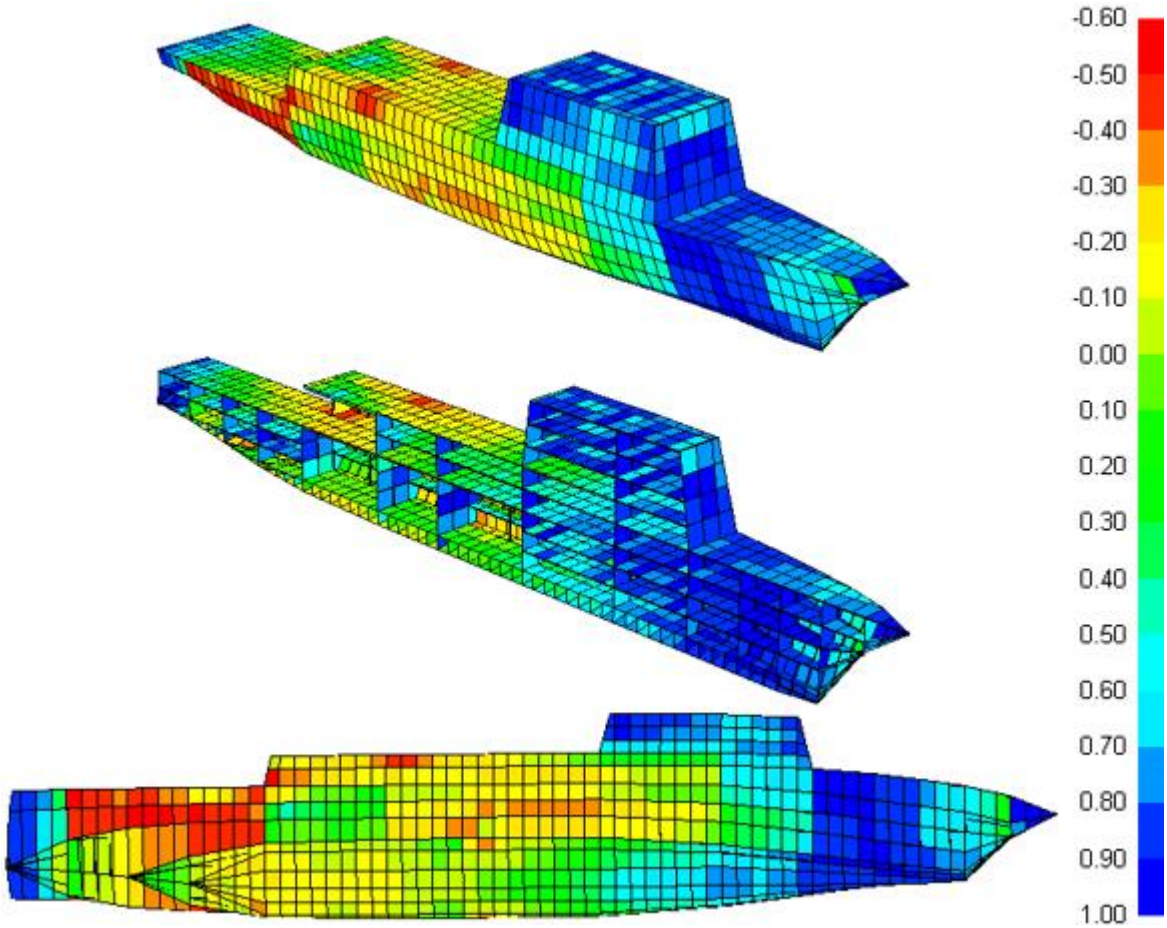

Figure 76 – Adequacy of DDG Structure, Sagging Whipping Design Load Case

As shown in Figure 74 and Figure 76, the deflected shapes of the ship in the whipping design load cases are capable of causing significant damage to the ship structure. Many panels

along the ship are inadequate and large areas of failed elements exist in both loading conditions. However, it is not possible to make a determination about the overall condition of the hull girder due to the localized nature of this analysis.

To determine if the hull girder has failed, the bending moment distributions are investigated and the maximum bending moments are compared to the ultimate strength bending moments predicted by ALPS/HULL. The bending moment distributions for the hogging and sagging whipping design load cases are shown in Figure 77 and Figure 78, respectively. The magnitude of the maximum hogging bending moment is 1,567 MN-m, while the maximum sagging bending moment is 1,463 MN-m. Both of these occur 48.3 meters forward of the stern. Due to the maximum hogging bending moment having a larger magnitude than the ultimate strength hogging bending moment, it is likely that the hull girder will collapse as a result of this whipping loading. The VT whipping model calculates a maximum hogging bending moment magnitude of 1,385 MN-m and a maximum sagging bending moment of 1,314 MN-m. These values are between 10 and 12 percent smaller than the maximum bending moments calculated by the bending moment analysis in MAESTRO, which is close enough to be compared to the ultimate strength bending moments as an approximate method to determine if the hull will collapse.

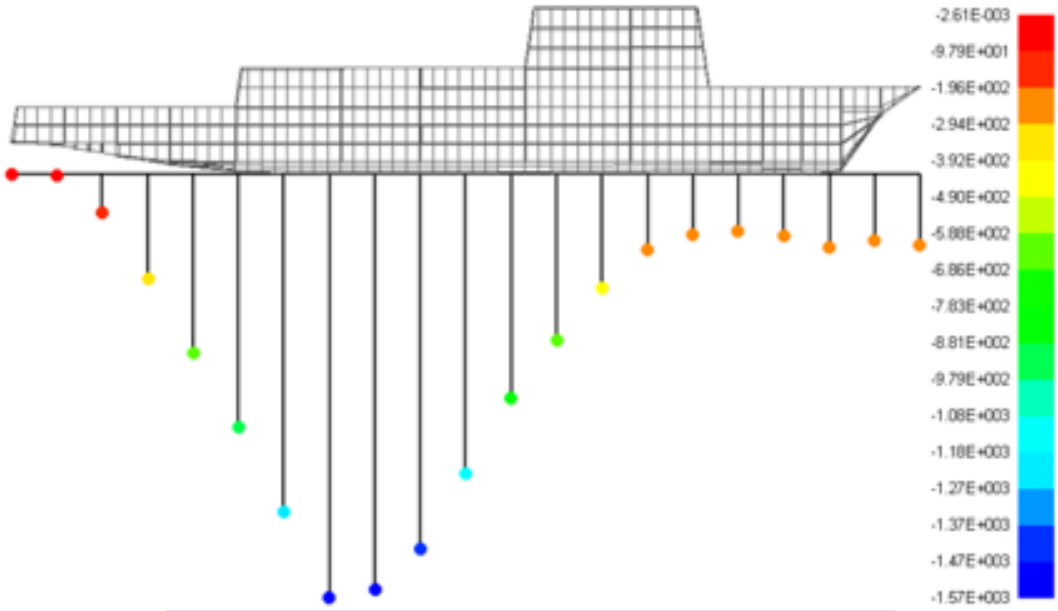

Output

Station	X(m)	Bending Moment(MN*m)
0	0	-0.00261098
1	6.9	-2.77722
2	13.8	-139.821
3	20.7	-384.016
4	27.6	-662.245
5	34.5	-933.006
6	41.4	-1248.61
7	48.3	-1566.98
8	55.2	-1537.52
9	62.1	-1385.35
10	69	-1105.8
11	75.9	-826.982
12	82.8	-612.105
13	89.7	-421.562
14	96.6	-280.414
15	103.5	-224.195
16	110.4	-208.687
17	117.3	-228.606
18	124.2	-268.497
19	131.1	-245.122
20	138	-259.392

Maximum Bending Moment(Full Ship) in Structural Coordinates:
M=-1566.98(MNm)

Figure 77 – Bending Moment Distribution, Whipping Hogging Design Load Case

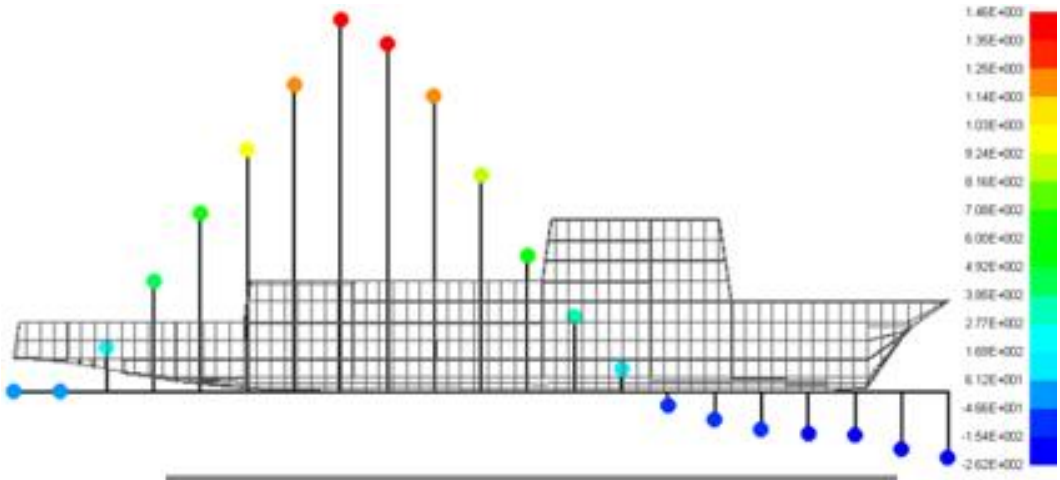

Output

Station	X(m)	Bending Moment(MN*m)
0	0	-0.00267306
1	6.9	-2.77286
2	13.8	169.807
3	20.7	432.67
4	27.6	699.301
5	34.5	952.322
6	41.4	1208.91
7	48.3	1462.77
8	55.2	1367.93
9	62.1	1164.6
10	69	848.911
11	75.9	532.513
12	82.8	292.797
13	89.7	90.2851
14	96.6	-56.3204
15	103.5	-113.724
16	110.4	-149.337
17	117.3	-168.955
18	124.2	-175.431
19	131.1	-231.981
20	138	-262.234

Maximum Bending Moment(Full Ship) in Structural Coordinates:
M=1462.77(MNm)

Figure 78 – Bending Moment Distribution, Whipping Sagging Design Load Case

Chapter 4 Parametric Study

4.1 Problem Statement

In this chapter, a parametric study of the VT UNDEX-induced ship whipping model described in Chapter 2 is performed using the lumped mass model derived from the MAESTRO DDG model in Chapter 3. The goal of the study is to identify a worst case UNDEX-induced whipping scenario for the ship model. Charge and bubble characteristics are varied through a design space encompassing a wide range of potential threats. ModelCenter [60] is used to perform the trade study. Once a worst case scenario is determined, the overall response of the ship structure is analyzed in MAESTRO using the method described in sections 3.2.1.4 and 3.2.2.2 to determine if the ship is capable of surviving the UNDEX event.

The design space for the study is set up to ensure that a wide range of potential threats are investigated. The design space consists of three design variables (DVs): charge size, charge weight, and charge longitudinal position along the ship. These variables can be controlled by a potential attacker, so it is important to be aware of advantages and vulnerabilities presented by of each combination of DVs.

The limits of the design space for each DV are given in Table 20. The charge size limits are selected to represent the warhead sizes of past and present underwater explosive threats, which are given in Table 1 and Table 2. The lower limit of charge depth is the minimum depth required for a bubble resulting from a 100 kg charge to emit one full bubble pulse before reaching the surface. The upper limit of charge depth is chosen to limit the number of explosion bubbles which result in small or insignificant fluid accelerations arriving at the ship. The longitudinal charge position limits are set so that the charge can be placed anywhere between the bow and stern of the ship, with a value of zero representing that the charge is at the bow.

Table 20 – Design Space Variables and Limits

Description	Name	Units	Lower Limit	Upper Limit
Charge Size (TNT or TNT Equivalent)	W	kg	100	650
Charge Depth	D	m	12	40
Charge Position (Fraction of Ship Length from Bow)	L_charge_percent	-	0	1

Several variables are held constant an individual trade study, but can still be changed at the discretion of the user prior to the starting the study. Values for these variables are listed in Table 21. The charge is placed directly under the centerline of the ship because this setup is the shortest distance from the bubble center to the ship, therefore exposing the ship to the largest possible fluid accelerations from a given charge at a given depth. The three bubble model control variables are set so that the analysis is for a migrating bubble. The number of vibration modes is set to six because only the first few low frequency vibration modes are needed to accurately represent the vibration behavior of a ship, as discussed in sections 2.2.5 and 2.2.6. This number includes the rigid body modes which are ignored when calculating the final results, meaning only modes three through six are included in the results of the analysis. The output location for the bending moment and deflection results is chosen to be at the midpoint of the weightless beams connecting the lumped masses. The time step is selected to be small enough to obtain an accurate representation of the bubble behavior, but large enough to ensure that computation time is not negatively affected. The ship is assumed to be vibrating in a body of salt water. Finally, the material properties selected are for steel.

Table 21 – Parametric Study Constants

Description	Name	Units	Default Value
Horizontal Distance from Charge Location to Ship Centerline	H_charge	m	0
Bubble Model Migration Control Variable (1 = migrating, 0 = no migration)	alpha_bubble	-	1
Bubble Model Free Surface Effect Control Variable (1 = on, 0 = off)	beta	-	1
Bubble Pseudo Drag Coefficient Control Variable	Cd	-	2.25
Number of Vibration Modes Included in the Analysis	n_modes	-	6
Position of Output as a Fraction of Weightless Beam Length	xbar_percent	-	0.5
Time Step	tstep	s	0.001
Gravitational Acceleration	g	m/s^2	9.81
Water Density	rho	kg/m^3	1025
Young's Modulus	E	GPa	204
Poisson's Ratio	nu	-	0.3

4.2 UNDEX-Induced Whipping Model in ModelCenter

A simple two module ModelCenter model was developed to run the study. It consists of an input component linked to a Matlab component, which contains the UNDEX-Induced whipping code presented in Chapter 2. The model setup is shown in Figure 79. ModelCenter allows modules to be linked, Design of Experiments to be run, and Response Surface Models to be fit to the results. Various types of optimizations may also be performed.

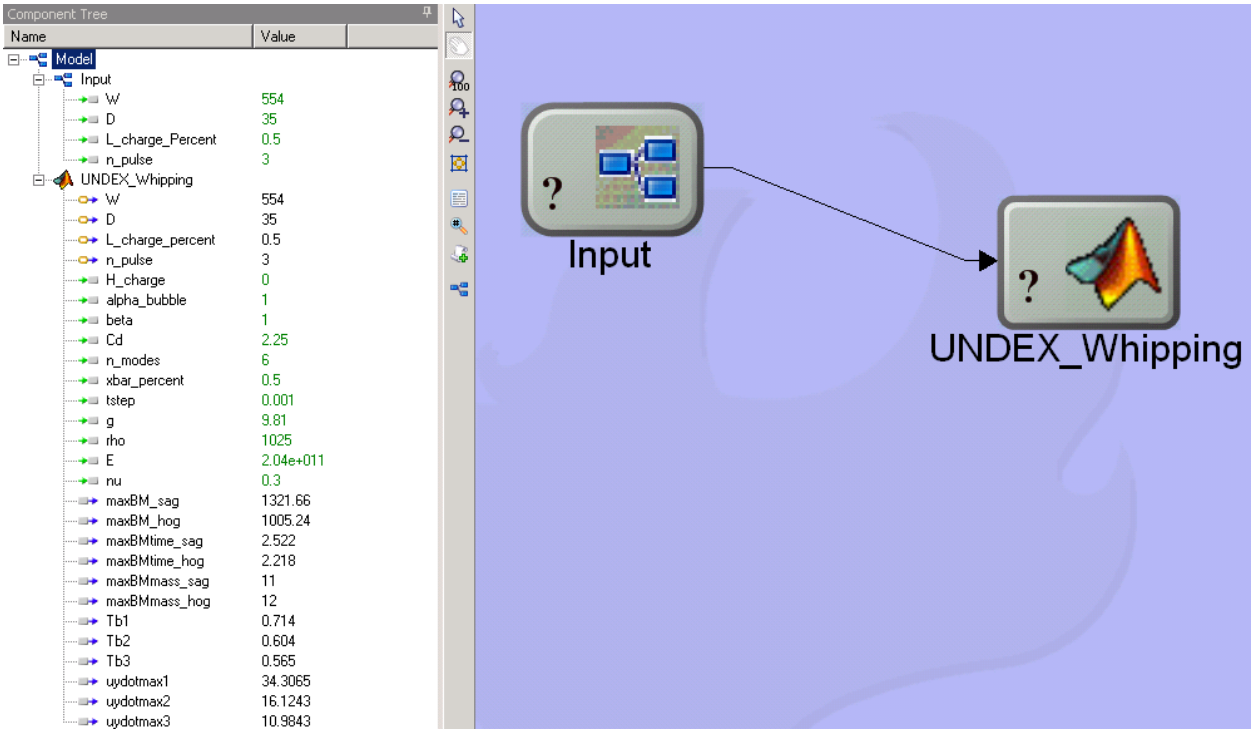

Figure 79 – ModelCenter UNDEX-Induced Whipping Model Component Setup

The variables output by the ModelCenter whipping model are listed in Table 22. The value of maximum bending moment is used to determine the severity of the whipping load. The location and time of the maximum bending moments are provided for reference only. The bubble output variables are also included for reference, as they are significant factors in determining the whipping loads. Including these variables as outputs allows for simpler analysis and identification of trends during post-processing.

Table 22 – ModelCenter Whipping Model Output Variables

Description	Name	Units
Maximum Sagging Bending Moment	maxBM_sag	MN-m
Maximum Hogging Bending Moment	maxBM_hog	MN-m
Time Max Sagging BM Occurs	maxBMtime_sag	s
Time Max Hogging BM Occurs	maxBMtime_hog	s
Lumped Mass Location of Max Sagging BM	maxBMmass_sag	-
Lumped Mass Location of Max Hogging BM	maxBMmass_hog	-
First Bubble Oscillation Period	Tb1	s
Second Bubble Oscillation Period	Tb2	s
Third Bubble Oscillation Period	Tb3	s
First Oscillation Bubble Pulse Peak Pressure	uydotmax1	m/s^2
Second Oscillation Bubble Pulse Peak Pressure	uydotmax2	m/s^2
Third Oscillation Bubble Pulse Peak Pressure	uydotmax3	m/s^2

4.2.1 Design of Experiments

The Design of Experiments (DOE) tool in ModelCenter was used to conduct the study. The DOE tool explores the design space and helps the user to determine which DVs have the greatest impact on outputs. Due to the large design space, three-thousand runs were performed to include DV combinations which represent the entire design space. The specific combinations of DVs were generated by the Latin Hypercube DOE algorithm, which randomly generates DV combinations that cover the design space. The DOE inputs ("Design Variables"), outputs ("Responses"), and setup are shown in Figure 80. A runtime variable, *n_pulse*, is added as an input to automatically control the length of the simulation and is discussed in the following section.

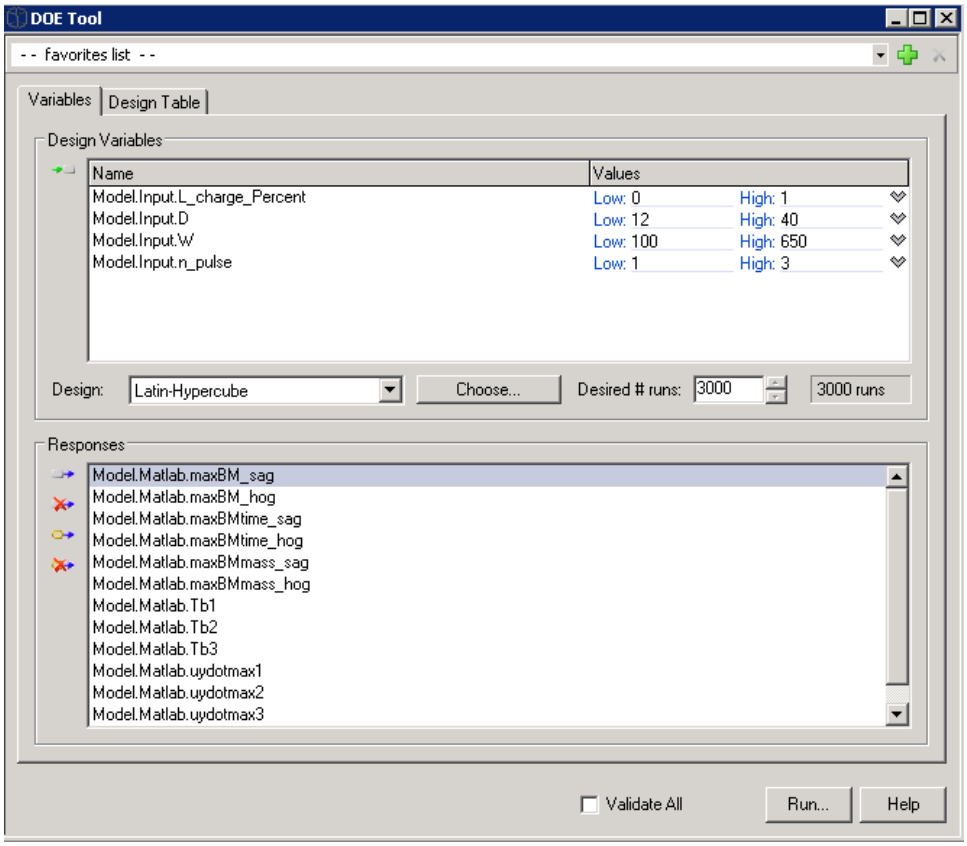

Figure 80 – DOE Setup

4.2.2 Code Automation Modifications

Many of the randomly generated DV combinations result in scenarios that the VT model cannot analyze due to a violation of key assumptions made during the model derivation, such as the bubble reaching the water surface. The original code relied on the user to select combinations of charge size, charge depth, and explosion simulation time that allowed for the desired number of bubble pulses to reach the ship. The user was also responsible for ensuring the chosen combinations did not violate any of the assumptions made during the model development. Each of these functions has been automated to ensure the smooth operation of the study for all DV combinations. A series of checks are also included to avoid code instabilities. With these checks applied, roughly thirty percent of the DV combinations result in errors and give no results.

The explosion bubble simulation time is calculated based on the number of pulses included in the analysis. The *n_pulse* runtime variable is used to assign the number of bubble pulses to be included in each run. Runs with one, two, or three pulses are possible. Three pulses is the maximum number the VT bubble model can reliably calculate. The similitude equation for bubble period,

equation (2), is used to calculate the simulation time required to complete the inputted number of pulses. Using migration-adjusted depths improved the stability and accuracy of the period calculations. The similitude equation for bubble migration, equation (9), is used to calculate the depth of the bubble center at the start of each secondary oscillation for use in the time calculations. The total migration distance at the start of the third oscillation is estimated using the same equation with an adjusted constant to ac3count for the loss of energy between the first and second oscillation. An additional percentage of the final bubble period is also included in the explosion simulation time to allow for the total impulse of the final pulse to be incorporated in the analysis. The equations used to calculate the explosion bubble simulation time are listed below:

$$T_{exp,1} = 1.2T_1 \tag{128}$$

$$T_{exp,2} = T_1 + 1.21T_2 \tag{129}$$

$$T_{exp,3} = T_1 + T_2 + 1.21T_3 \tag{130}$$

$$Z_{0,2} = Z_0 - m \tag{131}$$

$$Z_{0,3} = Z_0 - 1.8m \tag{132}$$

where a subscript number is the oscillation or pulse number, T is the bubble oscillation period, T_{exp} is the explosion bubble simulation time, Z_0 is the pressure head at the initial charge depth for use in the similitude equations, and m is the migration distance during the first bubble oscillation.

The first check to determine if a given combination of charge size, charge depth, and number of pulses would reach the surface prior to the completion of the explosion bubble simulation is performed concurrent with the explosion bubble simulation time calculations. If the predicted migration distance is greater than the initial charge depth, an error is output to stop the simulation. The simulation will also stop if an error occurs during the integration of the bubble EOM, which often occurs if the bubble reaches the surface.

Two more checks are conducted after the bubble behavior and fluid accelerations are calculated, but before any whipping calculations occur. These conditions are used because they are characteristic of a bubble migrating close to the surface and will cause the VT model to output unreliable whipping results if true. The first check determines if the upper surface of the bubble is within one meter of the water surface. If this is true, an error is output to stop the simulation. The second check ensures that shape of the fluid acceleration curve is reasonable. This is done by comparing the minimum and peak fluid accelerations for the last pulse with those from the previous pulses:

$$\dot{u}_{y,max,2} > 2\dot{u}_{y,max,1} \tag{133}$$

$$\dot{u}_{y,max,3} > \dot{u}_{y,max,1} \tag{134}$$

$$\dot{u}_{y,end} < 2\dot{u}_{y,min,n} \tag{135}$$

where $\dot{u}_y$ is a fluid acceleration, a subscript *max* indicates a maximum value, a subscript *min* indicates a minimum value, a subscript number is the bubble oscillation number, a subscript *n* indicates a value from the last bubble oscillation, and a subscript *end* indicates the last value of the vector. An error is output and the simulation is stopped if any of these conditions are met.

4.3 Results

The data collected by the DOE is viewed using the Data Explorer in ModelCenter. Data Explorer gives the user numerous visualization and analysis options to help determine the influence of the DVs on the output. It is also possible to set up visualizations to show the effect of the reference outputs, such as bubble period and peak fluid accelerations, on the output.

A histogram showing the distribution of each DV and output during the study is given in Figure 81. A nearly even distribution of runs at each longitudinal charge position were completed. A greater number of deep charge runs were completed compared to shallow charge runs. Also, more runs were completed with smaller charges and with fewer bubble pulses. These trends were expected due to the existence of large charge at shallow depth combinations within the design space.

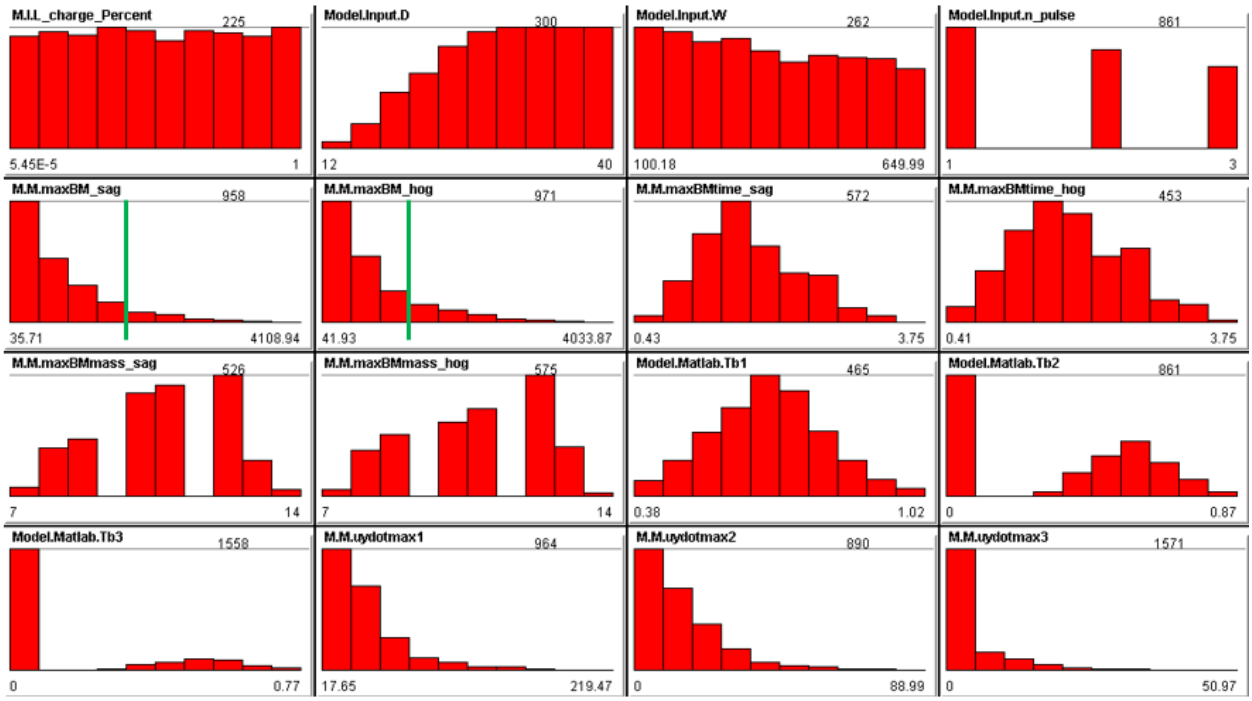

Figure 81 – DV and Output Histogram

The green lines on the maximum bending moment output represent the approximate ultimate strength bending moments. The majority of the runs produced maximum bending moments that do not result in a failure of the hull girder, as the results are heavily skewed toward lower values of bending moments. However, the largest calculated bending moments are significantly greater than the ultimate bending strength of the hull girder. The maximum bending moments tend to occur near midship, with the most frequent location being at the location of the ninth, tenth, and twelfth lumped masses, or 62.1, 69, and 82.8 meters aft of the bow. The distance of the lumped masses from the bow is calculated by multiplying the lumped mass number by 6.9 meters.

The Variable Influence Profiler plot for the maximum hogging and sagging bending moments are given in Figure 82 and Figure 83, respectively. The charge depth is the DV that has the largest impact on bending moment results, with longitudinal charge position and charge weight both having significant effects. A combination of charge weight and charge depth also significantly affect this result.

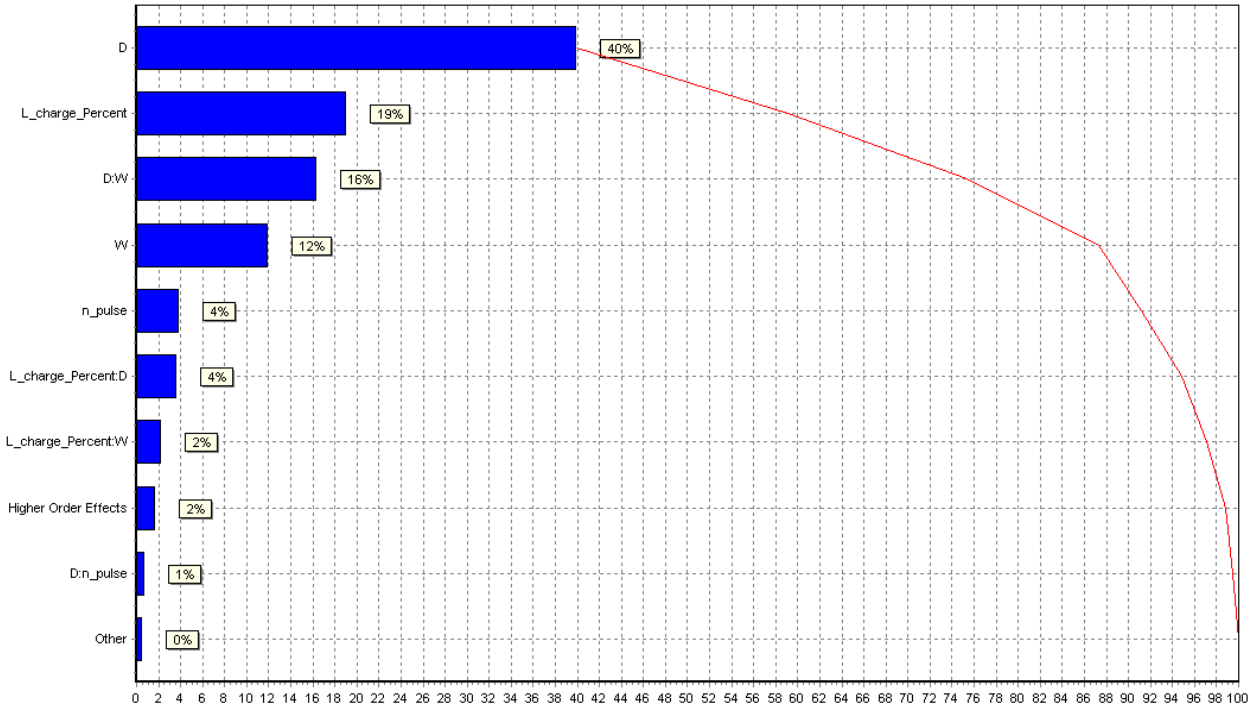

Figure 82 – Variable Influence Profiler Plot, Maximum Hogging Bending Moment

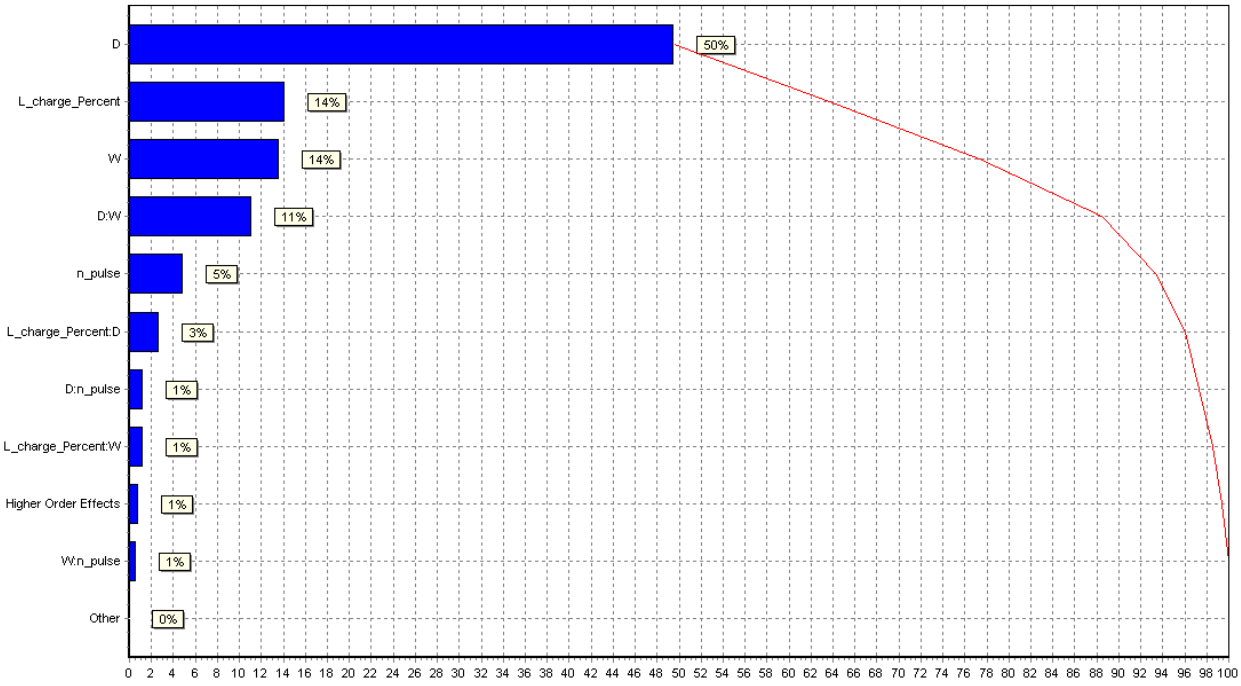

Figure 83 – Variable Influence Profiler Plot, Maximum Sagging Bending Moment

The Sensitivity Summary is another visualization which shows how much the DVs influence each of the outputs. Some statistics for the outputs are also provided. The Sensitivity Summaries for both maximum bending moment outputs are shown in Figure 84. In general, the

maximum bending moments are expected to increase with decreasing charge depth, increasing charge size, and as the charge is moved closer to the stern. The strongest correlation is with charge depth. Also, the ultimate strength bending moments are either within or just outside of one standard deviation from the mean.

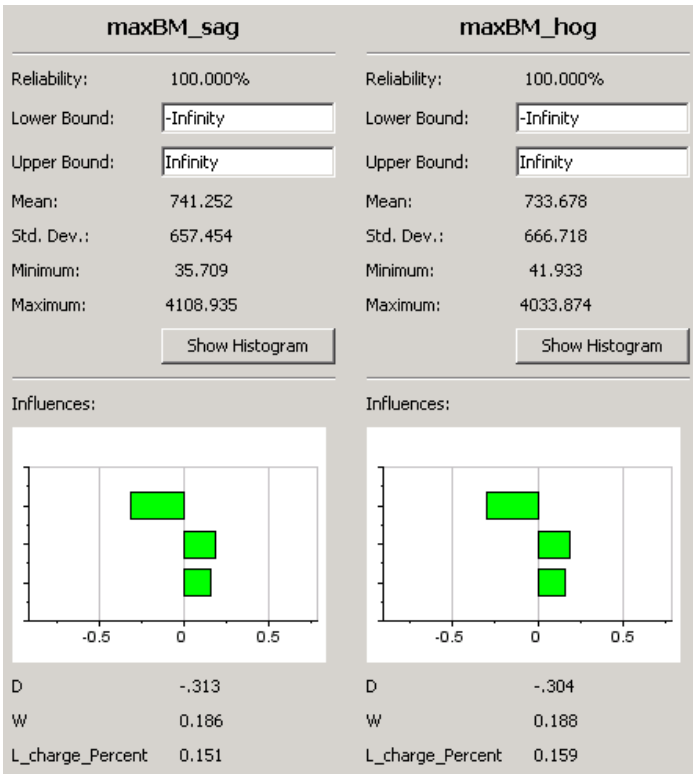

Figure 84 – Sensitivity Summaries, Maximum Bending Moments

The Prediction Profiler allows the user to visualize and interactively investigate the design space [61]. It also creates a series of curves which predict the values of an output variable for a combination of DVs. This tool can be used to determine specific ranges and combinations of DVs that result in an "optimized design." For this study, an "optimized design" is considered to be a set of DVs that result in the largest possible maximum bending moment.

The Prediction Profiler plots for the maximum hogging bending moment output are shown in Figure 85. These curves are not for an "optimized design." The inputs are set to be the midpoint of the design space for each DV, which are represented by the black diamonds on the plots, for a two pulse simulation. These values are given in Table 23. Only the maximum hogging bending moments are shown because the overall trends are the same for both bending moment cases and the ultimate strength hogging bending moment calculated by ALPS/HULL is lower than the one

calculated for sagging. Each plot shows how the bending moment will vary due a change in the value of an individual DV given that the remaining DVs are held constant.

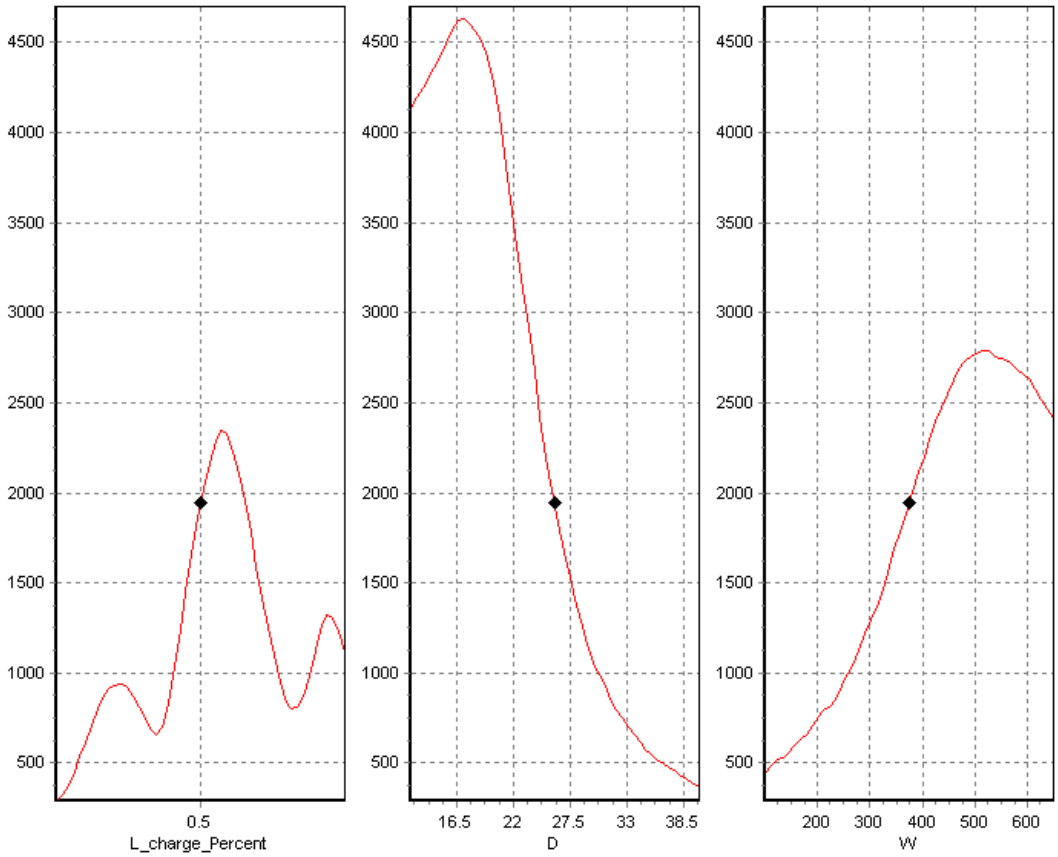

Figure 85 – Prediction Profiler Plots, Maximum Hogging Bending Moment, Design Space Midpoint Case

Table 23 – DV Values at Midpoint of Design Space

Design Variable	Value
Charge Weight (kg)	375
Charge Depth (m)	26
Charge Longitudinal Position	0.5

The charge location that will produce the largest bending moments is slightly aft of midship. The ship is most likely to be excited in its third vibration mode with the charge at this location. Local minimums exist near the bow and stern, 29 and 130 meters from the bow, respectively. Charges at these locations are likely to excite the ship in its fourth vibration mode. Both moving the charge closer to the ship and increasing the size of the charge are predicted to

increase whipping loading on the ship, but only to a certain point. This indicates that some combination of charge depth and charge weight is necessary to produce the greatest whipping loading on the ship. The maximum possible bending moment is predicted for charge depth of approximately 16.5 meters. The maximum bending moment is predicted for a charge weighing approximately 520 kg. Allowing the simulation to run for three bubble pulses would also likely increase the severity of the whipping loading on the ship. The bending moment predicted for this combination of DVs is 1,942 MN-m, while the VT whipping model calculates a hogging bending moment of 2,033 MN-m. The difference between these two values equates to a percent error of 4.5 percent.

It is also possible to produce a number of scatter plots that show the relationships between various DVs and outputs. All DV combinations completed during the study are included on the plots. Points that are gray in color are DV combinations that result in a maximum hogging bending moment less than 1,172 MN-m, the ultimate strength hogging bending moment for the ship predicted by ALPS/HULL. Though the VT whipping model and MAESTRO methods of calculating bending moments will produce slightly different results, this threshold is still a good estimate of which cases will cause catastrophic damage to the ship. Approximately 19 percent of successful runs resulted in a bending moment greater than 1,172 MN-m.

Figure 86 shows the scatter plot of longitudinal charge position versus maximum hogging bending moment. The color scale shows the longitudinal location of the maximum bending moment. The plot shows that the charge location that produces the largest bending moments is slightly aft of midship, between approximately 72 and 98 meters aft of the bow. There are also two local minimums near the bow and stern. These trends are similar to those predicted by the longitudinal positon curve calculated by the Prediction Profiler in Figure 85.

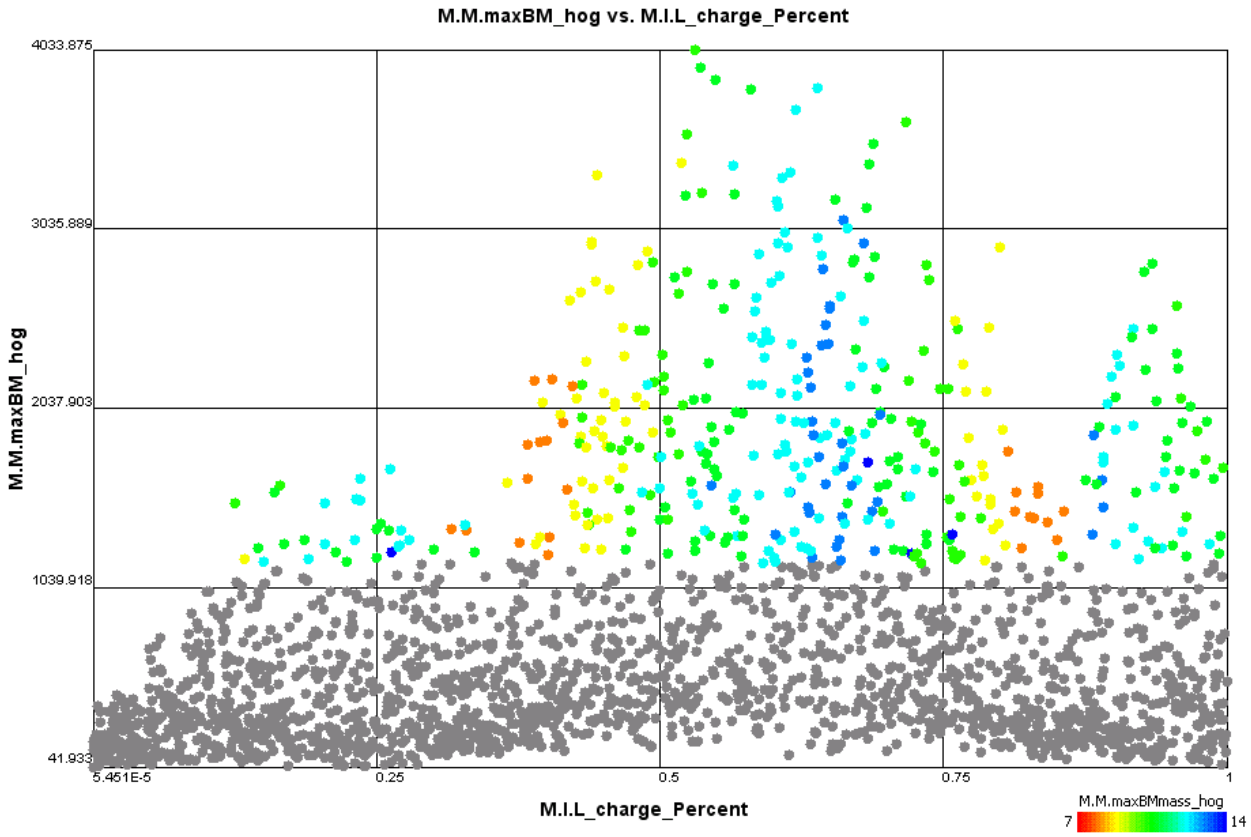

Figure 86 – Longitudinal Charge Position vs. Maximum Hogging Bending Moment vs. Longitudinal Location of Maximum Bending Moment

Figure 87 shows the scatter plot of charge depth versus charge weight. The color scale shows the maximum hogging bending moment. In general, larger charges placed close to the ship result in larger bending moments. However, the largest bending moments are produced by small charges very close to the ship or large charges weighing between 550 and 625 kg positioned approximately 28 meters below the ship. The red curve on the figure is an approximate trend line following the areas of larger bending moments. The combinations of charge size and depth along this curve likely produce bubbles with oscillation frequencies close to the natural vibration frequency of the hull in its third vibration mode.

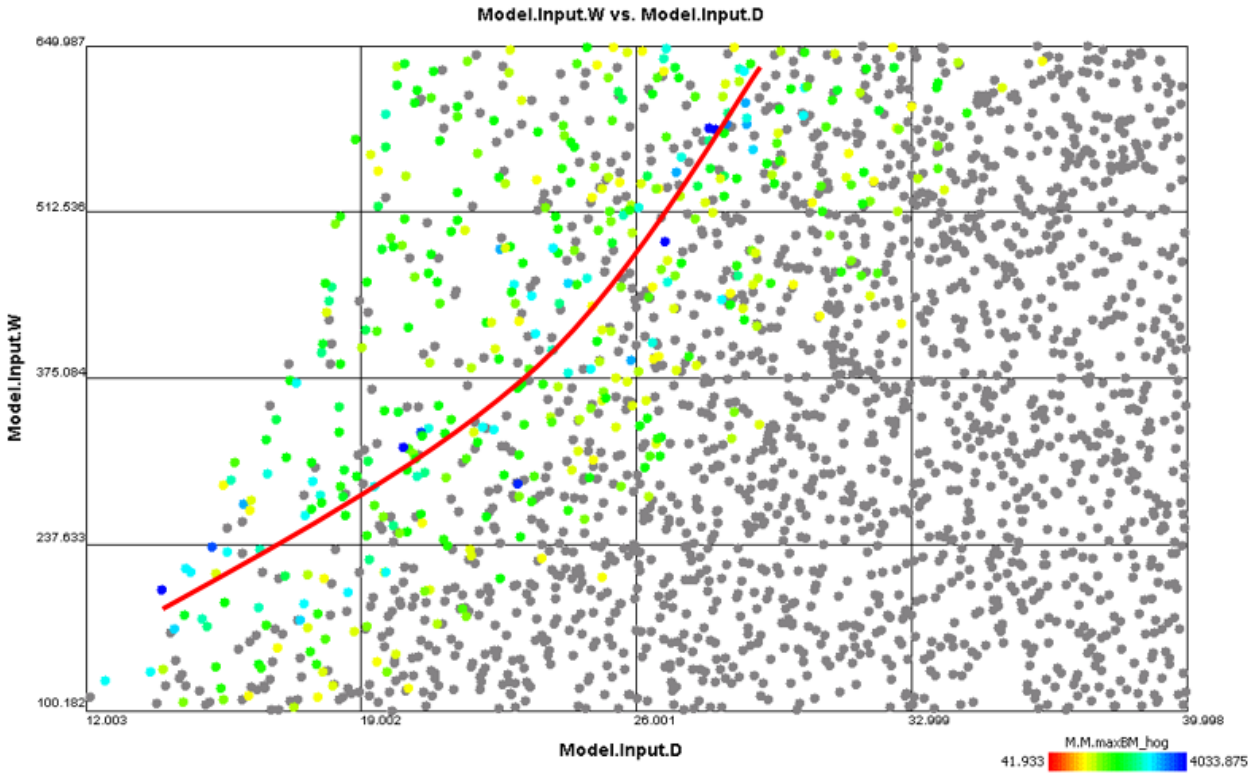

Figure 87 – Charge Depth vs. Charge Weight vs. Maximum Hogging Bending Moment

The shape of the approximate trend line in Figure 87 is very similar to the shape of the curve of the similitude equation for bubble period when the period is held constant, equation (2). This equation is plotted for a bubble period of 0.687 seconds, which is the natural vibration period of the ship's third mode shape, for the first (green) and second (red) bubble pulses in Figure 88. The blue circles on the plot show the charges for the runs that resulted in the 25 largest hogging bending moments from Figure 87. All runs are in the area between the two similitude curves, meaning that the bubbles from these charges had a bubble period similar to the natural vibration period of the ship's third mode shape.

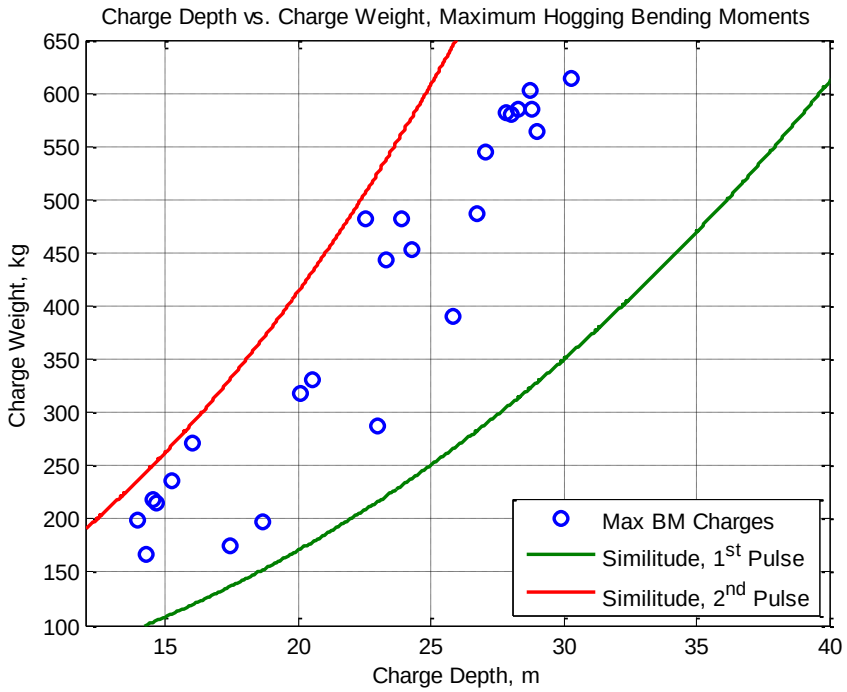

Figure 88 – Charge Depth vs. Charge Weight, Maximum Hogging Bending Moments and Similitude

Figure 89, Figure 90, and Figure 91 show scatter plots of bubble oscillation periods versus maximum hogging bending moments for the first, second, and third bubble oscillation, respectively. The color scale shows the variation of the maximum fluid acceleration for the plotted bubble oscillation. The red points on the vertical axis on Figure 90 and Figure 91 represent simulations that did not include a second or third pulse, respectively. In Figure 89, the maximum bending moments occur when the bubble period is between approximately 0.73 and 0.83 seconds, which correspond to oscillation frequencies between 1.21 and 1.37 Hertz. In Figure 90 and Figure 91, the maximum bending moments occur when the bubble period is between approximately 0.64 and 0.75 seconds, which corresponds to oscillation frequencies between 1.33 and 1.56 Hertz. These frequencies are very similar to the natural vibration frequency of the third vibration mode of the ship, 1.455 Hz. The plots also show that a larger fluid acceleration does not necessarily result in a more significant whipping loading. A bubble which emits pulses of an intermediate magnitude at a frequency similar to the natural vibration frequency of the ship are likely to produce more significant bending moments than a bubble which emits pulses of large magnitude at a dissimilar frequency.

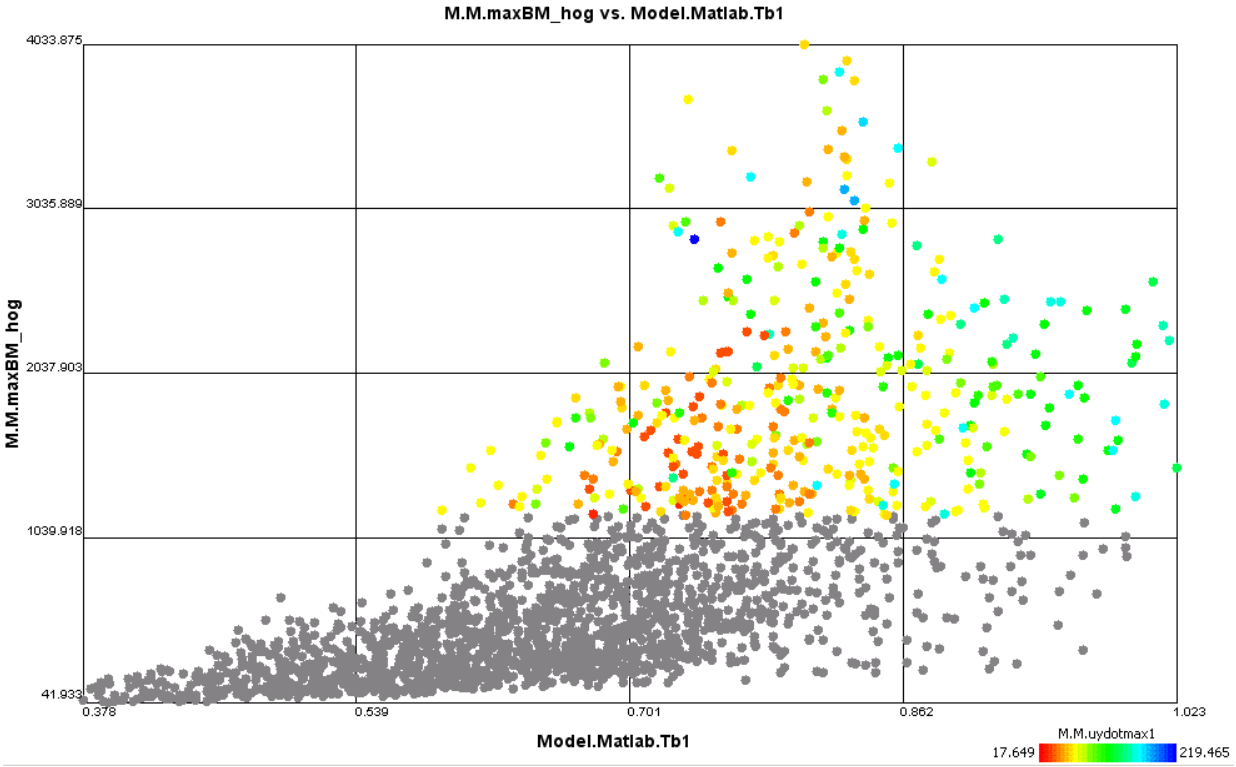

Figure 89 – First Bubble Oscillation Period vs. Maximum Hogging Bending Moment vs. Maximum Fluid Acceleration from the First Bubble Pulse

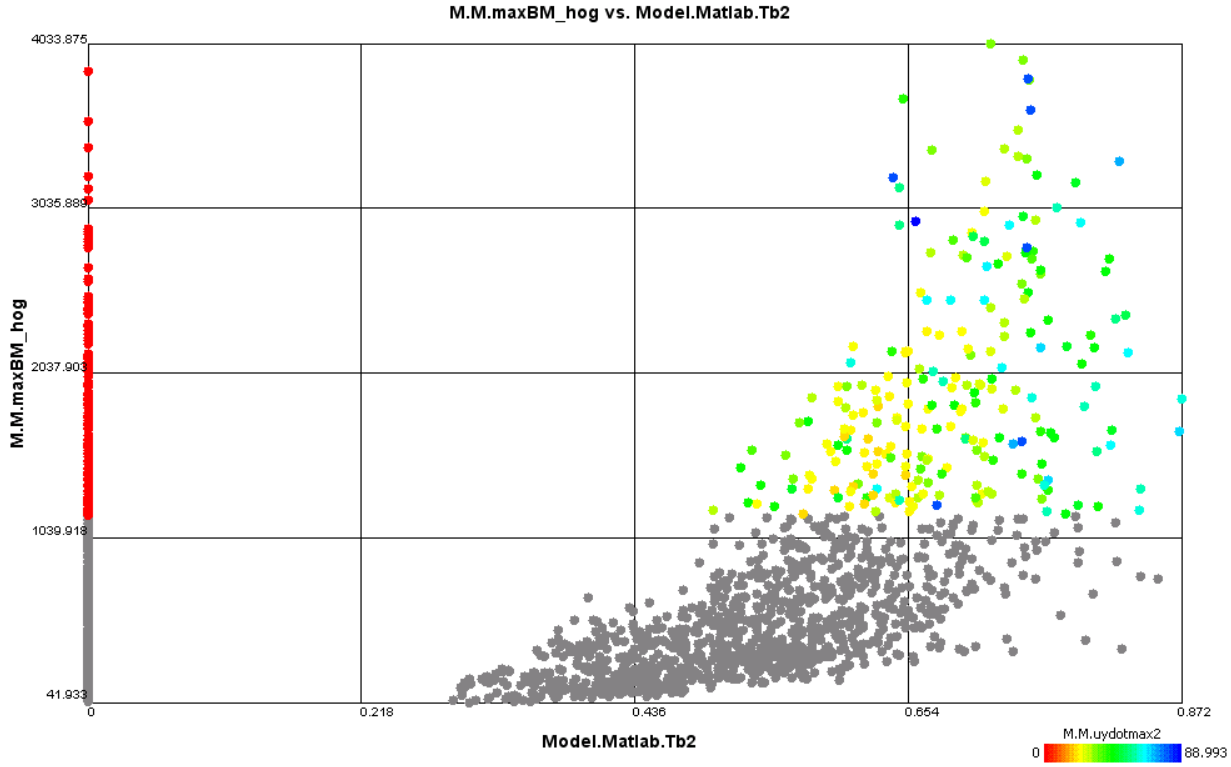

Figure 90 – Second Bubble Oscillation Period vs. Maximum Hogging Bending Moment vs. Maximum Fluid Acceleration from the Second Bubble Pulse

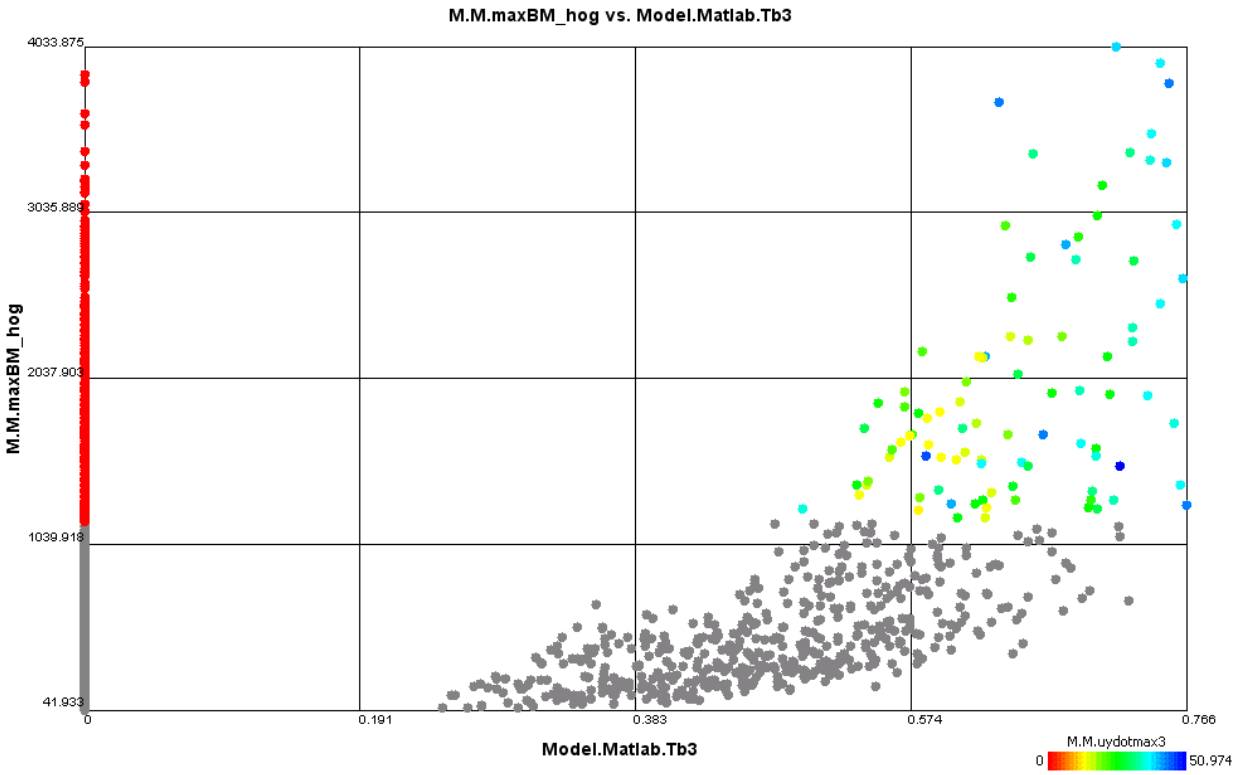

Figure 91 – Third Bubble Oscillation Period vs. Maximum Hogging Bending Moment vs. Maximum Fluid Acceleration from the Third Bubble Pulse

Chapter 5 Conclusions and Future Work

5.1 Conclusions

In this thesis, a fast and simple UNDEX-induced whipping model was developed for use as a design tool during early-stage ship design. The model consists of an UNDEX bubble model capable of accurately predicting bubble behavior for up to three pulses and a ship structural vibration model which calculates the deflection of the ship in response to the pressure pulses produced by the UNDEX bubble. The bubble model includes the effects of bubble migration and the presence of a free surface. It was tuned to match the behavior of secondary oscillations as predicted by the similitude equations by applying an empirical energy dissipation at the bubble minimums. The shape and magnitude of the bubble fluid acceleration pulses calculated by the bubble model were found to be similar to experimental results and those predicted by other bubble models.

The ship structural vibration model was developed using beam theory and represents the ship as a free-free beam with varying cross-sectional properties along its length. This model was found to be capable of accurately calculating the mode shapes and natural vibration frequencies for multiple ships. Strip theory and the distant flow approximation were utilized to apply the fluid motion to the structure. The ship vibration EOM was decomposed into its normal mode shapes and all but the third through sixth modes were ignored during the analysis.

The VT whipping model was found to give the most consistent results within the extremes of other available methods. However, more detailed and accurate data is needed to validate and verify the whipping responses predicted by the VT model.

A method for conducting a detailed structural analysis of a given MAESTRO finite element ship model for the whipping design load cases was also presented. This analysis helps to identify areas of the ship that are likely to fail under a whipping load condition. It was found that local and global damage to the ship is likely to occur as the result of the ship experiencing significant whipping loading. An analysis of the ultimate bending strength of the hull was also conducted, which revealed that hull rupture may occur due to severe whipping loads.

The presented UNDEX-induced whipping analysis approach is a useful method for determining preliminary design load cases for early-stage ship design. The process of developing an approximate ship model for input into the VT model does not require excessive modeling time

or the use of complex structural equations. The method quickly analyzes the ability of a ship to withstand UNDEX-induced whipping loading on both the global and local levels. Multiple load cases can be developed and investigated with minimal time investment to ensure that many possible threats are considered during the design process.

A parametric study was conducted using the VT whipping model. Many substantial conclusions and observations regarding the most significant factors necessary to create a devastating UNDEX-induced whipping scenario can be made from a review of the parametric study data. Charge size, charge depth, and longitudinal charge position are found to have a significant impact on the whipping loading imposed on the ship. In general, larger charges detonated close to the ship result in greater whipping loading on the ship due to the large fluid accelerations these combinations produce. However, the most severe loads resulted from charges that produced bubbles with oscillation frequencies similar to the natural vibration frequency of the ship's third mode. This is due to the pulses causing resonant vibration of the ship. Charges positioned slightly aft of midship resulted in the most significant whipping load scenarios. This position corresponds to the location of the maximum relative deflection of the ship's third vibration mode shape. The most severe UNDEX-induced whipping hogging bending moment calculated, 4,034 MN-m, is more than triple the predicted ultimate bending strength of the hull by ALPS/HULL, 1,172 MN-m. Therefore, it is safe to assume that the hull girder will have collapsed under this loading and no detailed analysis of this case is required.

Smaller ships with natural vibration frequencies similar to the oscillation frequencies of UNDEX bubbles will always be vulnerable to UNDEX-induced whipping attacks. Attempting to design a ship to survive the most extreme potential UNDEX-induced whipping loads is not feasible, as the scantlings required to withstand the loads will severely reduce the ability of the ship to perform its mission. The best way to limit the potential for structural damage due to whipping is to strengthen the local and global structure of the ship, which will increase the robustness of the local panels and the ultimate strength of the hull girder. The stiffened hull girder is more capable of surviving the original UNDEX-induced whipping event, in part because it has different natural vibration frequencies. However, the ship is now just as vulnerable to an UNDEX event that produces a bubble with an oscillation frequency similar to its new natural frequency. This event may be capable of causing a load equal in magnitude to the original loading, but the

increased ultimate strength of the hull girder improves the probability that the ship will survive the event.

5.2 Important Issues Not Addressed In This Study

There are several important aspects of the UNDEX-induced whipping problem that were not included in the model developed in this thesis. Two such issues are bubble-ship interaction and bubble jetting. A bubble contacting the hull is a likely result of a near-hull UNDEX event. The bubble-ship interaction greatly influences the motions of both the ship and bubble. In this event, the bubble is also capable of causing significant local and global damage to the ship structure and hull girder. The complex physics of this problem require the use of a CFD bubble model coupled to a dynamic FEA method to perform the analysis.

Bubble jetting occurs when the water column under the bubble caused by the vertical migration of the bubble pushes upward through the bubble with significant speed. The high speed water column loads the hull with pressures capable of puncturing the hull, as described in section 1.2.2. If the water column is large enough, the hull may be sliced into two pieces. Bubble jetting will only occur under specific conditions relating to the distance the bubble will migrate and the distance of the bubble from the ship. These types of bubble scenarios can be modelled and simulated using CFD software coupled to structural FEA programs or hydrocodes. Though outside the scope of this thesis, these phenomena are significant UNDEX threats for ships of all sizes.

5.3 Recommendations and Future Work

To improve the accuracy and increase the applicability of the model without greatly increasing its complexity and the computer resources necessary to run the model, the following future work is recommended.

1. Add damping to the ship vibration EOM. Including this will more accurately reflect the physics of the problem and will limit the severity of the predicted whipping motions.
2. Add equations for horizontal fluid accelerations and expand the structural model to account for vibration in the horizontal plane. Including these adjustments will improve the accuracy of the model for explosions positioned off of the ship's centerline. It also presents the opportunity to develop structural and vibration equations for applicability to multi-hulled vessels, such as catamarans and trimarans.

3. Incorporate the effects of plastic hull deformation into the structural and vibration models. Including plastic deformation effects will improve the overall accuracy of the model when predicting bending moments and deflections for scenarios that result in whipping loads that exceed the elastic limit. A more accurate bending moment calculation will lead to more accurate predictions of hull rupture.

References

1. Baron, M.L. and Daddazio, R. “Underwater Explosions,” in *Shock and Vibration Computer Programs*, 1995.
2. OPNAV Instruction 9070.1, “Shock Hardening of Surface Ships,” 12 January 1987.
3. Brown, A.J. (2014), “AOE 4264 Principles of Naval Engineering – Survivability Introduction I,” Virginia Tech Department of Aerospace and Ocean Engineering, 2014.
4. Brown, A.J. (2014), “AOE 4264 Principles of Naval Engineering – Survivability Introduction II,” Virginia Tech Department of Aerospace and Ocean Engineering, 2014.
5. Naval Technology, “The World’s Deadliest Torpedoes,” 9 June 2014, http://www.naval-technology.com/features/featurethe-worlds-deadliest-torpedoes-4286162/
6. DiGiulian, T., NavWeaps Website, http://www.navweaps.com/
7. Hartshorn, D.S., “Naval Mines,” http://www.hartshorn.us/Navy/navy-mines.htm
8. “SSK Collins Class (Type 471) Submarine, Australia,” Naval Technology, http://www.naval-technology.com/projects/collins/
9. Truver, S.C. "Taking Mines Seriously: Mine Warfare in China's Near Seas." *Naval War College Review* Vol 65(2), 2012.
10. Erickson, A.S., Goldstein, L.J., and Murray, W.S. “Chinese Mine Warfare: A PLA Navy ‘Assassin’s Mace’ Capability.” U.S. Naval War College, Newport, RI, 2009.
11. Webster, K.G., “Investigation of Close Proximity Underwater Explosion Effects on a Ship-Like Structure Using the Multi-Material Arbitrary Lagrangian Eulerian Finite Element Method,” Master’s Thesis, Virginia Tech, Blacksburg, VA, 2007.
12. Reid, W.D., *The Response of Surface Ships to Underwater Explosions*. Department of Defense, 1994.
13. Misovec, A.P., *Explosion Phenomena,* David W. Taylor Naval Ship Research and Development Center, 1976.
14. Cole, R.H., *Underwater Explosions*, Princeton University Press, 1948.
15. Klenow, B., “Assessment of LS-DYNA and Underwater Shock Analysis (USA) Tools for Modeling Far-Field Underwater Explosion Effects on Ships,” Master’s Thesis, Virginia Tech, Blacksburg, VA, 2006.

16. Park, J., “A Coupled Runge Kutta Discontinuous Galerkin-Direct Ghost Fluid (RKDG-DGF) Method to Near-field Early-time Underwater Explosion (UNDEX) Simulations,” Ph.D. Dissertation, Virginia Tech, Blacksburg, VA, 2008.
17. Mair, H.U., et al., Lagrangian Hydrocode Modeling of Underwater Explosive/Target Interaction. 61st Shock and Vibration Symposium, 1990. 5: p. 79-89.
18. Keil, A.H., *The Response of Ships to Underwater Explosions*. The Society of Naval Architects and Marine Engineers, 1961.
19. Wood, S.L., *Cavitation Effects on a Ship-Like Box Structure Subjected to an Underwater Explosion*, in *Mechanical Engineering*. 1998, Naval Postgraduate School: Monterey, CA.
20. Hicks, A.N., “The Theory of Explosion-Induced Ship Whipping Motions,” Naval Construction Research Establishment, NCRE Report R579, 1972.
21. Vernon, T.A., “Whipping Response of Ship Hulls from Underwater Explosion Bubble Loading,” Technical Memorandum 86/225, Defence Research Establishment Atlantic, 1986.
22. Snay, H.G., “Underwater Explosion Phenomena: The Parameters of Migrating Bubbles,” U.S. Naval Ordinance Laboratory, NAVORD Report 4185, 1962.
23. Hicks, A.N., "Explosion Induced Hull Whipping,” *Advances in Marine Structures*, Admiralty Research Establishment, Dunfermline, Scotland, UK, 1986.
24. Swisdak, M., “Explosion Effects and Properties: Part II – Explosion Effects in Water”. NSWC/WOR TR 76-116, 1978.
25. Arons, A.B., “Secondary Pressure Pulses Due to Gas Globe Oscillation in Underwater Explosions. II. Selection of Adiabatic Parameters in the Theory of Oscillation”. *J. Acoust. Soc. Am.* 20, 277, 1948.
26. Swift, E., Jr., and Decius, J.C., “Measurements of Bubble Pulse Phenomena, III. Radius and Period Studies,” *Underwater Explosion Research II*, Office of Naval Research, Washington, D.C., Vol. 2, pp. 553-599, 1947.
27. Riley, M., “Analytical Solutions for Predicting Underwater Explosion Gas Bubble Behavior,” Defence R&D Canada – Atlantic, Technical Memorandum 2010-237, 2010.
28. Brennen, C.E., *Cavitation and Bubble Dynamics*, Oxford University Press, 1995.
29. Van Lear, B.T., “Underwater Explosions with Fluid-Structural Interactions,” Dissertation, University of Minnesota, Minneapolis, MN, 2008.

30. Leighton, T.G., "Derivation of the Rayleigh-Plesset Equation in Terms of Volume," University of Southampton, Institute of Sound and Vibration Research, ISVR Technical Report No. 308, 2007.
31. Geers, T.L. and Hunter K.S., "An Integrated Wave-Effects Model for an Underwater Explosion Bubble," *J. Acoust. Soc. Am.* 111, pp. 1584-1601, 2002.
32. Chertock, G., "The Flexural Response of a Submerged Solid to a Pulsating Gas Bubble," *Journal of Applied Physics*, Vol. 24, No. 2, 1953.
33. Zong, Z., "A Hydroplastic Analysis of a Free-Free Beam Floating on Water Subjected to an Underwater Bubble," *Journal of Fluids and Structures* 20, pp. 359-372, 2005.
34. Miller ST et al. A pressure-based, compressible, two-phase flow finite volume method for underwater explosions. ComputFluids (2013), http://dx.doi.org/10.1016/j.compfluid.2013.04.002
35. Mair, H.U., Benchmarks for Submerged Structure Response to Underwater Explosions, Shock and Vibration 6 (1999), pp. 169-181.
36. Mair, H.U., Review: Hydrocodes for the Structural Response to Underwater Explosions, Shock and Vibration 6/2 (1999), pp. 81-96.
37. McGoldrick, R.T., "Ship Vibration," David Taylor Model Basin, Report 1451, 1960.
38. "Guideline for Evaluation of Finite Elements and Results," Ship Structures Committee, SSC-387, 1996.
39. Hughes, O.F. and Paik, J.K. *Ship Structural Analysis and Design*, Society of Naval Architects and Marine Engineers, New Jersey, 2010.
40. Bathe, K., *Finite Element Procedures in Engineering Analysis*, Prentice-Hall, New Jersey, 1981.
41. MAESTRO Structural Design Software Help Manual, DRS Advanced Marine Technology Center, 2015.
42. "MSC Nastran Product Brochure," MSC Software, 2013.
43. "MSC Nastran 2012 Dynamic Analysis User's Guide," MSC Software, 2011.
44. Hicks, A.N., "The Elastic Theory of Explosion Induced Whipping Computer Program Specification," Naval Construction Research Establishment, NCRE Report R550, 1968.

45. Stettler, J.W., “Damping Mechanisms and Their Effects on the Whipping Response of a Submerged Submarine Subjected to an Underwater Explosion,” Master’s Thesis, Massachusetts Institute of Technology, Cambridge, MA, 1995.
46. Matlab Documentation, MathWorks, 2015.
47. Molland, A.F., *The Maritime Engineering Reference Book: A Guide to Ship Design, Construction, and Operation*, Butterworth-Heinemann, Oxford, UK, 2008.
48. Logan, D.L., *A First Course in the Finite Element Method*, 4th ed., Nelson, Toronto, Ontario, Canada, 2007.
49. Barltrop, N.D. and Adams, A.J., *Dynamics of Fixed Marine Structures*, 3rd ed., Butterworth-Heinemann, Oxford, UK, 1991.
50. Lewis, F., “The Inertia of the Water Surrounding a Vibrating Ship,” Trans. SNAME, Vol. 37, 1929.
51. Zhang, N. and Zong, Z. “Hydro-Elastic-Plastic Dynamic Response of a Ship Hull Girder Subjected to an Underwater Bubble,” *Marine Structures,* Vol. 29, Issue 1, pp. 177-197, 2012.
52. Arons, A.B. “Measurement of Bubble Pulse Phenomena IV: Pressure-Time Measurements in Free Water,” U.S. Naval Ordinance Laboratory, NAVORD Report 408, 1947.
53. Paik, J.K. et al, “Benchmark Study on the use of ALPS/ULSAP Method to Determine Plate and Stiffened Panel Ultimate Strength,” MARSTRUCT 2011 Conference, Hamburg, Germany, 2011.
54. Paik, J.K. et al, “Methods for Ultimate Limit State Assessment of Ships and Ship-Shaped Offshore Structures: Part I – Unstiffened Plates,” *Ocean Engineering,* Vol. 35, Issue 2, pp. 261-270, 2008.
55. Paik, J.K. et al, “Methods for Ultimate Limit State Assessment of Ships and Ship-Shaped Offshore Structures: Part II – Stiffened Panels,” *Ocean Engineering*, Vol. 35, Issue 2, pp. 271-280, 2008.
56. Paik, J.K. et al, “Benchmark Studies: Ultimate Strength of Plates and Stiffened Panels,” Pusan National University Research Institute of Ship and Offshore Structural Design Innovation, 2011.
57. Paik, J.K. et al, “Benchmark Studies: Ultimate Strength of Ship Hulls,” Pusan National University Research Institute of Ship and Offshore Structural Design Innovation, 2011.

58. Paik, J.K. et al, “Modified Paik-Mansour Formula for Ultimate Strength Calculations of Ship Hulls,” MARSTRUCT 2011 Conference, Hamburg, Germany, 2011.
59. Ma, M., Personal Communication, 2015.
60. MAESTRO Structural Design Software, 2015, DRS Advanced Marine Technology Center, Maryland (www.maestromarine.com).
61. ModelCenter 10.0 Help Manual, Phoenix Integration, Inc., 2011.

Appendix A Hicks Sample Destroyer Lumped Mass and Beam Data

Mass Number	Distance from bow feet	Ship Mass tons	Added mass tons	Buoyancy tons	Immersion force tons/foot	Rotary inertia tons/ft	Section area in	Shear area in	Section inertia ft.in	Distance NA to keel feet
1	8.8	34	3	14	2.50	3050	333	111	37200	17.7
2	26.4	41	18	42	5.71	2120	422	109	44000	16.5
3	44.0	62	47	68	8.97	2900	510	107	52400	15.7
4	61.6	64	77	94	11.29	3660	603	106	61500	15.1
5	79.2	120	113	117	13.50	4410	693	108	71300	15.0
6	96.8	225	149	138	15.25	4700	818	122	86000	15.2
7	114.4	241	184	156	16.78	4750	1077	162	110100	14.2
8	132.0	103	218	172	18.04	7990	845	136	69200	10.2
9	149.6	155	239	184	18.65	5050	860	136	71600	10.3
10	167.2	136	248	193	18.83	6060	875	137	73200	10.5
11	184.8	158	254	185	18.92	3300	875	138	72800	10.6
12	202.4	191	252	185	18.90	4710	863	138	71600	10.7
13	220.0	127	237	181	18.69	3920	841	136	68400	10.7
14	237.6	137	221	173	18.38	2980	783	129	62000	11.1
15	255.2	139	203	162	18.00	2300	727	120	52800	11.6
16	272.8	238	176	145	17.25	4550	654	108	42600	12.3
17	290.4	177	151	120	16.71	3650	544	98	28800	12.0
18	308.0	60	137	92	15.40	1330	478	82	19900	10.0
19	325.6	56	86	63	12.00	2920	420	67	12000	6.2
20	343.2	54	60	35	9.90	1240				
	Total	2518	3073	2519						

Appendix B DDG Lumped Mass Representation Properties

Station Number	Distance from Bow (m)	Ship Mass (kg)	Buoyancy (kg)	Added Mass (kg)	Section Inertia (m^4)	Shear Area (m^2)	Neutral Axis Height (m)
0	0	7.679E+03	0	0	1.04E-08	5.66E-03	13.213
1	6.9	3.935E+04	5.084E+03	5.769E+03	1.19	0.155	10.813
2	13.8	6.926E+04	6.272E+04	5.148E+04	9.74	0.303	7.665
3	20.7	1.152E+05	1.375E+05	1.744E+05	12.81	0.305	7.409
4	27.6	2.442E+05	2.197E+05	2.430E+05	18.19	0.331	7.210
5	34.5	3.163E+05	2.993E+05	3.580E+05	103.73	0.581	12.344
6	41.4	3.646E+05	3.730E+05	6.632E+05	114.93	0.581	11.976
7	48.3	4.047E+05	4.332E+05	6.152E+05	133.92	0.637	11.943
8	55.2	4.227E+05	4.643E+05	9.376E+05	139.41	0.645	11.767
9	62.1	5.303E+05	5.038E+05	7.674E+05	47.52	0.491	8.194
10	69	4.968E+05	4.863E+05	1.054E+06	47.29	0.488	8.207
11	75.9	5.352E+05	4.998E+05	8.009E+05	46.92	0.481	8.234
12	82.8	3.908E+05	4.852E+05	1.066E+06	46.24	0.425	8.257
13	89.7	5.223E+05	4.913E+05	7.917E+05	43.52	0.505	8.282
14	96.6	5.104E+05	4.717E+05	1.034E+06	42.77	0.499	8.348
15	103.5	4.431E+05	4.444E+05	7.507E+05	17.56	0.399	6.071
16	110.4	1.844E+05	3.600E+05	7.376E+05	13.58	0.267	5.801
17	117.3	2.018E+05	2.402E+05	9.614E+05	9.31	0.169	6.267
18	124.2	1.935E+05	1.302E+05	8.906E+05	5.50	0.142	7.132
19	131.1	1.284E+05	5.310E+04	6.577E+05	4.28	0.142	7.523
20	138	4.822E+04	8.191E+03	4.368E+04	1.07E-05	6.68E-03	5.034
Total		6.169E+06	6.169E+06	1.260E+07			